ALMA MATER STUDIORUM
UNIVERSITÀ DEGLI STUDI DI BOLOGNA

Dottorato di Ricerca in Fisica
XXIII Ciclo - FIS/04

LUMINOSITY MEASUREMENTS WITH THE LUCID DETECTOR IN THE ATLAS EXPERIMENT

Relatore:
Chiar.mo Prof.
Mauro Villa

Correlatori:
Chiar.mo Prof.
Antonio Zoccoli

Dott.
Carla Sbarra

Coordinatore
Dottorato:
Fabio Ortolani

Candidata:
Sara Valentinetti

Anno Accademico 2010-2011

Contents

List of Figures

List of Tables

Introduction

The Standard Model is currently the most reliable description of the fundamental components of nature. A crucial element of the model is still missing: the Higgs boson, responsible for the spontaneous symmetry breaking of the electroweak interaction and the generation of the masses of all particles.

The main goals of the Large Hadron Collider (LHC) are the discovery of the Higgs boson, the precise measurement of Standard Model parameters and the detection of signatures of new physics. One of the four experiments installed at LHC is ATLAS. The description of LHC, together with the records reached during the 2010 data taking and some details about the ATLAS experiment, are presented in chapter 1.

Besides the center-of-mass energy, another feature of a collider is fundamental to accomplish any physics program: the luminosity, which correlates the event rate of any process to its cross section. LHC design luminosity is $L = 10^{34} cm^{-2} s^{-1}$. A good knowledge of luminosity is mandatory to calculate the cross section of any process by measuring its event rate, moreover, online luminosity monitoring is important to optimize the performance of both the collider and the experiments. A full description of the methods used to measure the luminosity at hadron colliders is provided in chapter 2.

At ATLAS the instantaneous luminosity is provided by a dedicated luminosity monitor: the LUCID detector. A full description of its functioning is presented in chapter 3. Quality checks on the performance of LUCID during the LHC running in 2010 as well as a comparison between real data and Monte Carlo predictions are presented in chapter 4. A description of the methods implemented in LUCID to measure the luminosity is reported in chapter 5. As a luminosity monitor, LUCID can not calculate directly the absolute luminosity. However, if a calibration is provided, the absolute luminosity evaluation is also possible. Depending to the different periods of data taking, different methods of calibration with different precisions will be used: Monte Carlo predictions with a precision of 20% (chapter 5), Van der Meer scan method with a precision at 3.4% level (chapter 6) and well know physics processes with a precision of 5% (chapter 7). During the 2011 shutdown, the installation of the ALFA detector was completed. ALFA is expected to provide

a luminosity calibration with precision of 2-3%.
My Ph.D work concerned many aspects:

- the study of the performances of LUCID with real data and the implementation in the ATLAS data acquisition system of some tools for the on line quality check of the detector;
- the tuning of the LUCID Monte Carlo predictions on the basis of the data acquired during 2010 LHC running;
- the development and implementation of the software driving the electronic board dedicated to the measurement of luminosity with LUCID;
- the collaboration in the analysis of Van der Meer scan results as well as Z production data in order to provide a calibration to the LUCID detector.

The work described in this thesis has been performed within the Bologna group of the ATLAS collaboration. Most of the research activities were developed at the CERN laboratories near Geneva.

Chapter 1

The ATLAS Experiment at the Large Hadron Collider

1.1 LHC: the Large Hadron Collider

1.1.1 Introduction

LHC (*Large Hadron Collider*) is the largest particle accelerator in the world. It is located beneath the border of France and Switzerland, in the underground tunnel which used to host the former *Large Electron-Positron (LEP)* Collider. The tunnel has a circumference of 27 km [1] and lies at a depth between 50 and 175 m below the surface. The LHC has two different modes of operation. One is as proton-proton collider with a design center-of-mass energy of 14 TeV. The other is as a lead ion collider, accelerating fully ionized lead atoms. For lead ions, the beams have a design energy of 2.76 TeV/nucleon, yielding a center-of-mass energy of 1150 TeV. The number of interactions that can occur in each beam crossing is proportional to the machine luminosity L (see chapter 2) according to $R = \sigma \cdot L$ where R is the number of events per second and σ is the total event cross section. LHC is designed to reach a luminosity of $L = 2 \cdot 10^{33} cm^{-2} s^{-1}$ during the first years of working. The high luminosity of $L = 2 \cdot 10^{34} cm^{-2} s^{-1}$ will be reached after 2/3 years, in proton beam operation. The design luminosity for lead ion beams is $10^{27} cm^{-2} s^{-1}$, because of the large number of particles produced when complex nuclei collide and because the inelastic cross section drastically increases with $\sigma_{inel} \propto A^{2/3}$ (where A is the atomic number).[1]

In 2009 LHC runned at a center-of-mass energy of 900 GeV and 2.36 TeV while the record center-of-mass energy of 7 TeV was reached in 2010. During the technical stop of 2013, LHC will be upgraded to reach the design energy of 14 TeV.

Four main experiments are now instrumented at LHC: two of them (ATLAS and CMS) are general purpose experiments, they aim at improving the precision on

Standard Model measurements as well as searching for new physics; LHCb is dedicated to b-quark physics, and finally ALICE is dedicated to heavy-ion physics.

1.1.2 LHC Physics Goals

The high energy and luminosity of LHC offer a large range of physics opportunities, from the precise measurement of the properties of known objects to the exploration of the high energy frontiers.
The Standard Model (SM) is currently the best description of the fundamental structure of matter: it is a phenomenological model which describes the behaviour of all known elementary particles and predicts the existence of a real particle, the Higgs Boson, which governs the mechanism of generation of all masses. The SM includes the Higgs mass as a free parameter that, once known, can be used to predict all the Higgs production and decay properties. Two limits are given for the Higgs boson mass m_H: direct searches at the e^+e^- collider LEP have led to the lower bound of 114.4 GeV [2], while an upper limit of 1 TeV can be inferred from unitary arguments [3]. Recent results at the Tevatron collider excludes the energy range at about 160 GeV. Assuming the overall validity of the Standard Model, a global fit to all the electroweak data leads to the 95% C.L. $m_H < 144$ GeV. Including the 95% C.L. lower limit obtained from LEP, the upper limit is increased to 182 GeV [4]. On the basis of the present theoretical knowledge, the Higgs sector of the Standard Model remains largely unconstrained. Further constraints can be derived under the assumption that the Standard Model is valid only up to a cutoff energy scale, beyond which new physics becomes relevant. The expected cross-section for the Higgs boson production in pp interactions must be compared with the cross-section of all concurrent processes (background). The cross-sections for the main processes are reported in figure 1.1. Any experiment searching for the Higgs boson must rely on colliders which allow the investigation of physics at the TeV energy scale and provide high rate, even for the rarest events. This requirement for high rate implies the need of high luminosity for LHC.

Despite its enormous success in describing almost all known experimental data available today, the SM is widely believed to be an effective theory valid only at the present accessible energies. Indeed, it does not include the fourth fundamental force, the gravitational force, and it does not explain the pattern of fermion masses. In its simplest version it does even not incorporate neutrino masses. Moreover there are at least three problems that are unsolved by the SM and that call for new physics:

- Given the high precision measurements at LEP and the particle content of the SM, it is demonstated that the coupling constants fail to converge at high

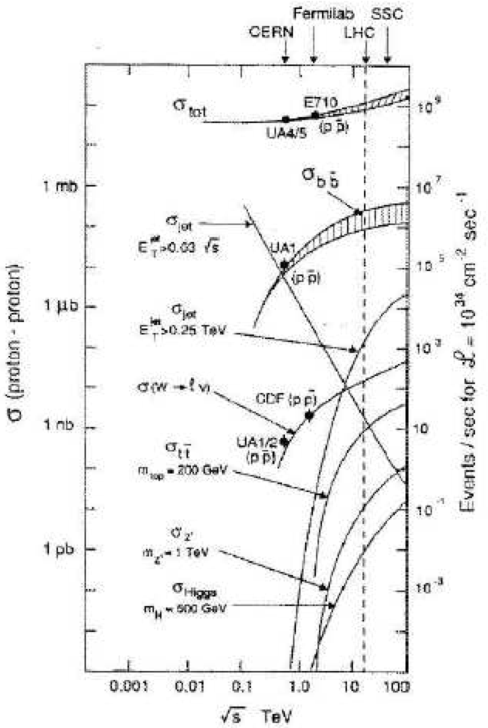

Figure 1.1: Cross section for various processes. The scale on the left represents the cross section measurements. The cross section is provided as a function of the center-of-mass energy. The dashed vertical line corresponds to the center-of-mass energy of 14 TeV. The scale on the right represents the number of events produced for a luminosity of $L = 10^{34} cm^{-2} s^{-1}$.

energy, while unification theories would prefer that the coupling constants meet at a common point, the GUT scale [5].

- There is a large contribution of non-baryonic, non-luminous component in the matter that is needed in the explanation of galaxy dynamics and in the Universe evolution from Big Bang up to now. Several arguments point toward the hypothesis that this matter should be non-relativistic. A particle that is stable, fairly massive, electrically neutral and has only weak interactions is thus required. The SM does not include any candidate particle to account for such Dark Matter component.

- In the SM, when calculating the radiative corrections to the Higgs boson mass, quadratic divergences in the cutoff scale appear.

Up to now the most qualified theory to solve the afore mentioned problems is the so-called Supersymmetry (SUSY) [6]. It is an extension of SM in which each particle has a supersymmetric partner which follows the opposite statistic: each boson has a supersymmetric fermion partner and each fermion has a supersymmetric boson partner. Supersymmetry is considered as the most attractive extension of the SM because it can even incorporate gravity. However, the most compelling arguments for Supersymmetry are phenomenological ones. When they are realized at low energies [4], SUSY theories can simultaneously solve all the problems mentioned above:

- The new SUSY particle spectrum contributes to the renormalization group evolution of the three coupling constants altering their slopes as a function of energy so that they meet at an energy scale slightly above 10^{16} GeV [4]. The value of M_{GUT} is large enough to prevent a too fast decay of the proton, as is generally the case with the particle content of the SM when only the unification of the two electroweak couplings is required [7].

- In minimal supersymmetric extensions, a discrete symmetry, called R-parity, is introduced to enforce in a simple way lepton and baryon number conservation [8]. A major consequence of this symmetry is that the lightest supersymmetric particle is stable. In most cases, this particle happens to be the lightest of the four neutralinos, which is massive, electrically neutral and weakly interacting. In large areas of the SUSY parameter space, the lightest neutralino can have the right cosmological relic density that could explain the cold Dark Matter in the Universe [9].

- Supersymmetry prevents the Higgs boson mass from acquiring very large radiative corrections: the quadratic divergent loop contributions of the SM particles to the Higgs mass are exactly cancelled by the corresponding loop contributions of their supersymmetric partners.

Despite the large number of supersymmetric particles foreseen in the theory, not a single one has been undoubtedly identified up to now. Therefore current best estimates of supersymmetric particle masses lie in the range explored by LHC. If they exist, they must be discovery by LHC experiments.

In addition to the wide panorama of SUSY theories, LHC will also provide important and precise measurements in several filed of SM, W/Z bosons, heavy flavours (including top quark properties and CP violation in B decay) and quark gluon plasma.

1.1.3 LHC Physics Requirements

Many of the new physics phenomena mentioned in the previous section have cross sections of 1 pb or less. Although the LHC design luminosity has purposely been chosen to cope with these small cross sections, interesting physics processes must still compete with the immense background coming from the inelastic *pp* cross section of about 80 mb. At design luminosity interesting *pp* collisions will be overlapped with about 23 inelastic interactions per bunch crossing which will significantly increase the difficulties of a clean identification of new physics processes.[10] The nature of proton-proton collisions imposes another experimental difficulty: the large number of particles expected to be produced are often grouped into sprays of particles called *jets*. Since jets often have a large boost, particles in a jet are usually nearly collinear. A detector with fine granularity is therefore needed to distinguish particles within a jet. Because the cross section for jet production is dominant over the rare processes mentioned in the previous section, it is important to identify experimental signatures of the rarest physics processes. These final state signatures, such as missing transverse energy or secondary vertices, impose further demands on the capability of particle-identification of the detectors [10]. The benchmark physics goals listed before have been converted into a set of general requirements for the LHC detectors [10]:

- fast, radiation hard electronics and sensor elements;
- high detector granularity, needed to handle the particle fluxes and to reduce the influence of overlapping events;
- electromagnetic calorimetry with good resolution for electron and photon identification and full-coverage hadronic calorimetry for accurate jet and missing energy (E_T^{miss}) measurements;
- good charge-particle momentum resolution and reconstruction efficiency in the inner tracker;
- efficient tracking for high p_T lepton momentum measurements, electron and photon identification, τ lepton and heavy flavour identification and full event reconstruction capability;
- good muon identification and momentum resolution over a wide range of momenta and the ability to determine unambiguously the charge of high p_T muons;
- large acceptance in pseudorapidity (η) with almost full azimuthal angle (ϕ) coverage. The azimuthal angle is measured around the beam axis whereas pseudorapidity is related to the polar angle θ measured from the beam direction (see figure 1.4 for ATLAS coordinate scheme):
  $\eta = -ln(tan\frac{\theta}{2})$;

- (highly) efficient triggering on low transverse-momentum objects with sufficient background rejection, to achieve an acceptable trigger rate for most processes of interest.

At LHC the general purpose experiments ATLAS and CMS have been designed to fulfill all these requirements and are therefore the best candidates to search for new physics processes.

1.1.4 LHC Design

LHC has been designed to shed light on an energy region almost unexplored yet. Most of the design parameters are therefore close to the technical limits.
In the LHC tunnel two proton beams circulate in opposite directions and collide every 25 ns. Each beam will be accelerated up to an energy of 7 TeV in order to obtain total center-of-mass energy of 14 TeV. In 2010 the energy was somewhat lower, 7 TeV. The same will be reached in 2011. A luminosity of $L = 2{\cdot}10^{33} cm^{-2}s^{-1}$ will be reached within the first years of working while the higher luminosity $L = 2 \cdot 10^{34} cm^{-2}s^{-1}$ will be reached after 2/3 years. The two beams circulate into two separate ultrahigh vacuum chambers at a pressure of 10^{-10} Torr. The beams are labelled 1 and 2, where the former circulates clockwise and the latter in the opposite direction. In order to keep the beams into circular trajectories, 1232 superconducting dipole magnets generate a magnetic field of 8.4 T at a current of 11.85 kA and a temperature of 1.9 K. Other 392 superconducting quadrupole magnets produce a field of 6.8 T necessary to focalize the beams.
The most important parameters of LHC are reported in table 1.1.

Beam Structure

The beams are not continuous: each can have at maximun 2808 filled bunches which are distributed into 3564 evenly spaced bunch slots, separated in time by 25 ns. Every slot, which can be filled or empty, is assigned its own ID number. When two bunch slots with the same ID are filled in the two different beams, they can be made to collide at special interaction points along the LHC tunnel. This is referred to as a bunch crossing (BC) and every event can be associated with a BCID for timing purposes.
Depending on the operational status of LHC, different filling schemes are foreseen. At the design luminosity each beam will contain 2808 filled bunches. The bunches will be gathered in trains of 80, out of which 72 filled and 8 empty, separated by 30 empty bunches. The minimum separation between the bunches (25 ns) is due to the requirement that there should be no additional interactions on each side of

Number of experiments	Two at high luminosity
Maximum collision energy	7 TeV
Number of particles per bunch	$1.67 \cdot 10^{11}$
Number of fill bunches	2808
Bunch separation	24.95 ns, 7.5 m
Bunch length	7.7 cm
Bunch width (Atlas)	16.7 μ m
Total number of particles	$4.7 \cdot 10^{14}$
Mean current	0.584 A
Luminosity	$2.3 \cdot 10^{34} cm^{-2} s^{-1}$
Inelastic pp cross section (7 TeV)	80 mb
Number of collision per bunch	25

Table 1.1: LHC parameters.

the interaction region, and by the time resolution of the experiments. Each bunch will contain 10^{11} protons and will be 7.55 cm long with a transverse length of few mm except in the interaction point where this length is reduced to 16 μm.
Assuming a total cross section of $10^{-25} cm^{-2}$ [10], there will be 10^9 events per second (or about 25 per filled BC). Elastic and inelastic collisions prevent the involved protons from continuing to circulate in the beam pipe in phase with the original bunches. A side effect of these collisions is that the beam luminosity degrades over time. The decay is exponential with an expected time constant τ = 14.9 h, taking all loss mechanisms into account. The beam can circulate for hours without requiring a refill. Measuring the luminosity is the task of various luminosity monitor detectors as LUCID (see chapter 3 and 5).

The Injection Chain

To reach the design center-of-mass energy of 14 TeV, protons will be accelerated through a chain of accelerators as presented in figure 1.2.

- **Linac2**: It is a linear accelerator for protons and ions. It injects beams of 50 MeV in the following accelerator with a rate of 1 Hz. The duration of each pulse ranges from 20 μs to 150 μs depending on the number of required protons.

- **Proton Synchrotron Booster (PSB)**: It speeds up the beams coming from Linac2 to an energy of 1.4 GeV. The accelerator is composed of 4 superimposed rings. Five bunches circulate in each ring that are then focused

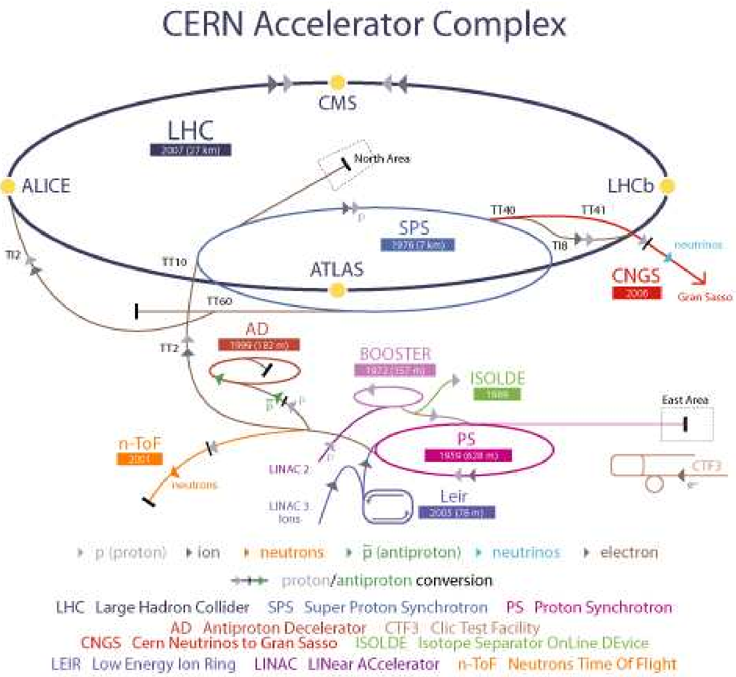

Figure 1.2: Scheme of injection chain at LHC.

and sent through a magnet deflector into a single line for injection into the next accelerating element.

- **Proton Sinctrotron (PS)**: It accelerates protons up to an energy of 28 GeV. It has been set to separate the bunches by 25 ns.
- **Super Proton Synchrotron (SPS)**: It is used as final injector for protons and heavy ions bringing the energy from 28 GeV to 450 GeV.

After injection in the LHC ring at 450 GeV, protons are accelerated up to the energy of 7 TeV (for each circulating beam).

1.1.5 LHC Experiments

Four experiments are installed along the LHC tunnel (see figure 1.3):

- **A Toroidal LHC ApparatuS (ATLAS)**: it is a multi-purpose experiment which works at high luminosity ($L = 10^{34} cm^{-2} s^{-1}$). It would be able to discover the Higgs boson as well as signatures of new physics.
- **Compact Muon Solenoid (CMS)**: it is a multi-purpose experiment designed to work up to high luminosity with the same intents of ATLAS, but implemented with different technologies.

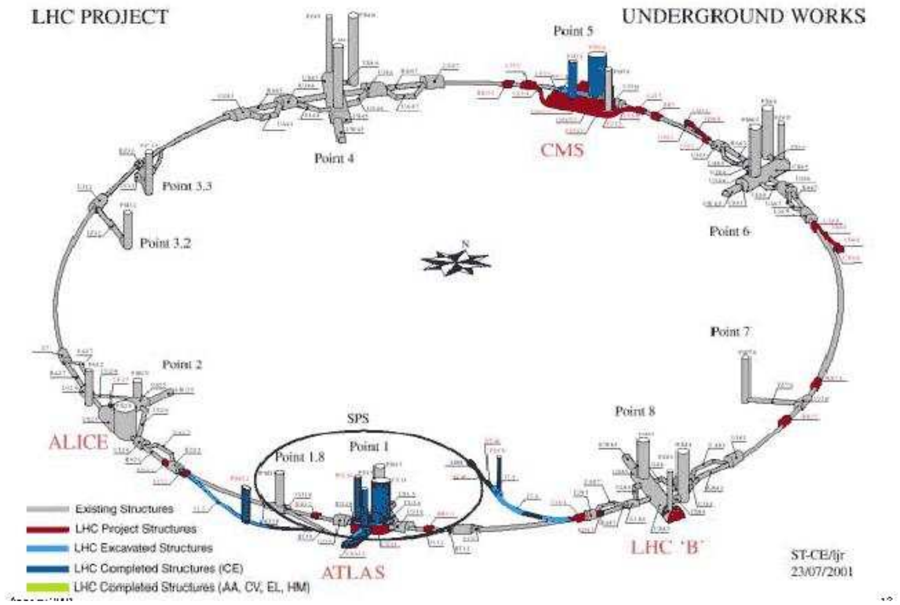

Figure 1.3: Position of the experiments along LHC ring.

- **LHCb**: it performs accurate measurements in the flavour physics of the B mesons, for example CP violation. Since the production and the decay vertices of B-mesons are difficult to reconstruct when there is more than one interaction per bunch crossing, LHCb works at a luminosity lower than the one designed for ATLAS and CMS (about $L = 10^{32} cm^{-2} s^{-1}$), using proton beams less focused near the interaction point.

- **A Large Ion Collider Experiment (ALICE)**: it is dedicated to the study of a condensed status of the matter, called *quark-gluon plasma*, by detecting particles that are produced in heavy ions collisions. Due to the high nucleus-nucleus cross section, the higher track density per collision and the technologies implemented by the detector, ALICE can work up to luminosities of $L = 10^{27} cm^{-2} s^{-1}$.

Other two experiments are installed along the tunnel:

- **LHCf**: it measures γ and π^0 spectra in the very forward region at luminosity of $L = 10^{29} cm^{-2} s^{-1}$. The aim is the calibration of Monte Carlo generators in cosmic rays studies. This detector was installed in 2009 and worked during the data taking at 900 GeV. It will be reinstalled once the design center-of-mass energy will be reached. At present, in place of LHCf, the EM module of the Zero Degree Calorimeters (ZDC) is installed (see section 1.2.2).

- **Total Cross Section, Elastic Scattering and Diffraction Dissociation at the LHC (TOTEM)**: it is designed to measure the total *pp* cross section at a luminosity of $L = 10^{29} cm^{-2} s^{-1}$. It is installed along the beam pipe near CMS.

1.2 ATLAS Experiment

The ATLAS experiment is a multi-purpose particle detector installed 100 m underground in the interaction Point 1 along the LHC tunnel (see figure 1.3 for the relative positions of the experiment). The detector has cylindrical symmetry, with a total length of 42 m and a diameter of 22 m [11]. The detector is organized in a central barrel and two end-caps that close either ends. In the barrel, the active detector elements form cylindrical layers around the beam pipe while in the end-caps they are organized in wheel layers.

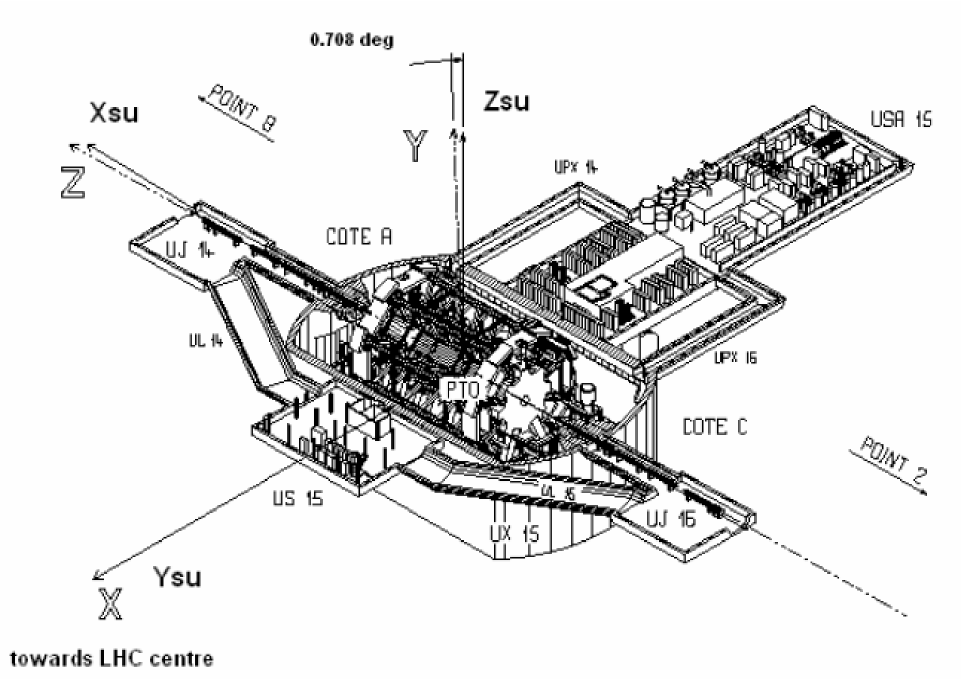

Figure 1.4: Overview of the underground facility at Point 1 where ATLAS is installed. The ATLAS coordinates are shown.

The origin of the ATLAS coordinate system is defined as the nominal interaction point. The beam direction defines the z-axis and the x-y plane, transverse to the beam direction. The positive x-axis is defined as pointing from the interaction point to the center of the LHC ring. The positive y-axis is defined as pointing upwards. The A-side (C-side) of the detector is defined as the side with positive (negative) z. ATLAS is nominally forward-backward symmetric with respect to the interaction point [11].

1.2.1 The Main Detectors

An overview of the ATLAS detector is shown in figure 1.5.

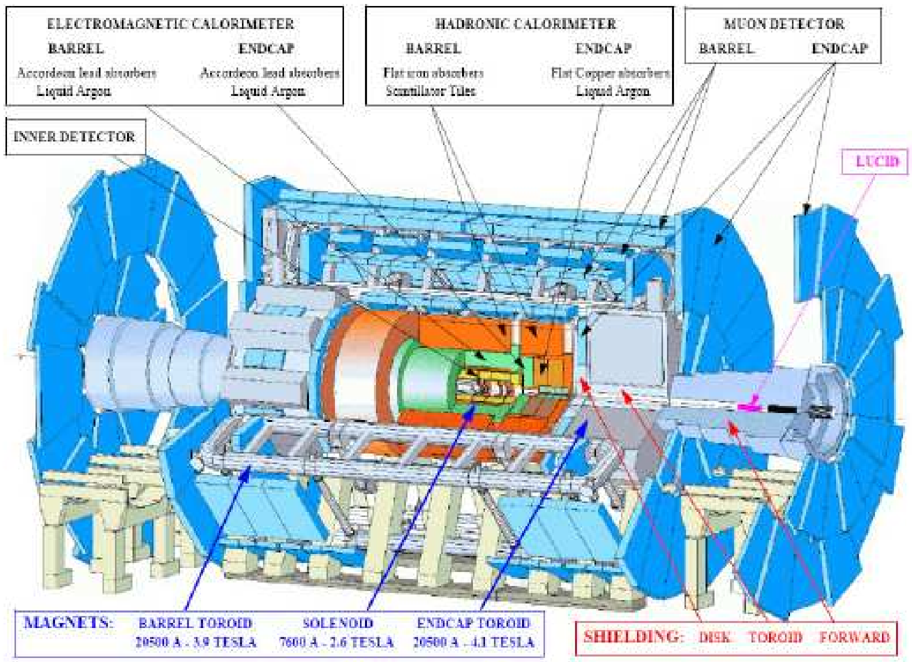

Figure 1.5: 3D view of ATLAS detector.

ATLAS is composed by many subsystems, each of which designed for specific purposes. These subsystems are: the Inner Detector (ID), the electromagnetic and hadronic calorimeters, the muon spectrometer and the forward detectors. Moreover, ATLAS is equipped with a magnetic system designed to bend the trajectory of high-energy charged particles. The magnetic field is necessary in order to measure the particle momentum.

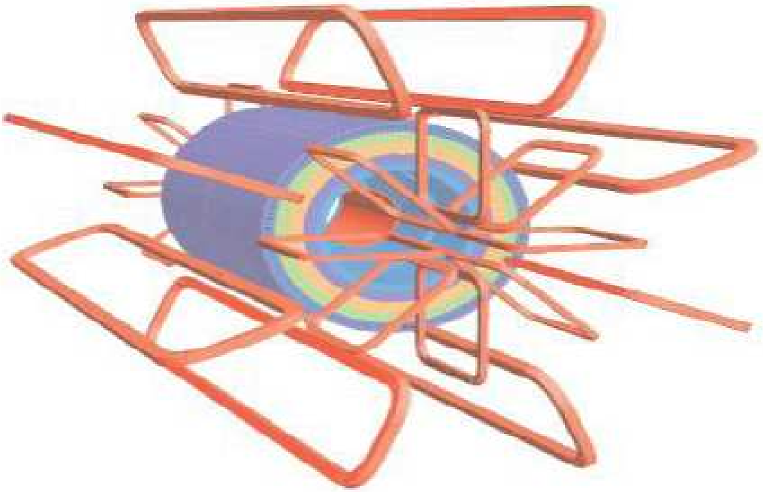

Figure 1.6: Scheme of the Barrel Toroids and End-Cap Toroid magnets (red) in ATLAS. The blue cylinder is the calorimeter.

The Magnetic System

In order to measure the momentum p of a particle of charge q it is necessary to measure the radius of curvature ρ of the trajectory when the particle crosses a region with a magnetic field B:

$$p\left[\frac{GeV}{c}\right] = 0.3 \cdot \rho[m] \cdot q \cdot B[Tesla] \tag{1.1}$$

ATLAS is characterized by 3 different magnetic field systems, each of which is composed by superconductive magnets kept at a temperature of 4.8 K:

- **Central Solenoid (CS)**: it is a superconducting solenoid installed around the Inner Detector cavity and providing a field of 2 T. It has a radius of 1.2 m, a length of 5.3 m and is parallel to the beam axis.

- **Barrel Toroid (BT)**: it is composed by 8 rectangular coils arranged in cylindrical configuration. The total length is 25 m, the outer diameter is 20.1 m and inner diameter is 9.4 m (see figure 1.6). It is installed just outside the calorimeters. It provides a magnetic field of 1.5 T.

- **End-Cap Toroid (ECT)**: it is composed by 8 rectangular coils arranged in a single cylindrical vessel. The outer diameter is 10.7 m while the inner diameter is 1.65 m. The total lenght is 5 m. The vessel is mounted at the ends of ATLAS in order to close the magnetic field lines produced by the

Barrel Toroid. With this configuration the magnetic field is orthogonal to the beam axis and has a value of 2 T.

Inner Detector (ID)

The Inner Detector (ID) is the inner part of ATLAS, near the beam pipe and closest to the interaction point. It is responsible for reconstructing the charged particle tracks and the primary and decay vertices. Approximately 1000 particles are expected to be produced every 25 ns for a luminosity of about $L = 10^{34} cm^{-2} s^{-1}$ within the ID volume [10], creating a very large track density in the detector.
The charge and direction of each track is measured, as well as the impact parameter, defined as the distance of closest approach to the beamline. The ID is also responsible for reconstructing both primary and secondary vertices, which are needed to identify B-mesons and converted photons. The ID is immersed in a 2T magnetic field. By measuring the curvature of the tracks, the momentum of the particles can be determined. The resolution of the track parameters can be parametrised as [11]:

$$\begin{aligned}
\sigma(d_0) &= 11 \oplus \frac{73}{p_T\sqrt{sen\theta}} && (\mu m) \\
\sigma(\Phi_0) &= 0.075 \oplus \frac{1.8}{p_T\sqrt{sen\theta}} && (mrad) \\
\sigma(z_0) &= 87 \oplus \frac{115}{p_T\sqrt{sen^3\theta}} && (\mu m) \\
\sigma(cot\theta) &= 0.7 \times 10^{-3} \oplus \frac{2.0 \times 10^{-3}}{p_T\sqrt{sen^3\theta}} && \\
\sigma\left(\frac{1}{p_T}\right) &= 0.36 \oplus \frac{13}{p_T\sqrt{sen\theta}} && (TeV^{-1})
\end{aligned} \tag{1.2}$$

where d_0, Φ_0, z_0, θ are respectively the distance of closest approach to the beam axis and the parameters that define the track direction in the transverse and longitudinal planes at the point of closest approach.
The layout of the ID is presented in figure 1.7. It consists of 3 parts: a barrel section of ±80 cm extending along the beam axis and 2 identical end-caps. In the barrel region high precision detector layers are arranged on concentrical cylinders around the beam axis while the end-cap detectors are mounted on disks perpendicular to the z-axis.
The high momentum and vertex resolution required by the physics to be studied by ATLAS call for high precision measurements. This goal is achieved by a high granularity in the ID through different technologies.
In the inner part the ID is composed by *Pixel Detectors* designed to measure the

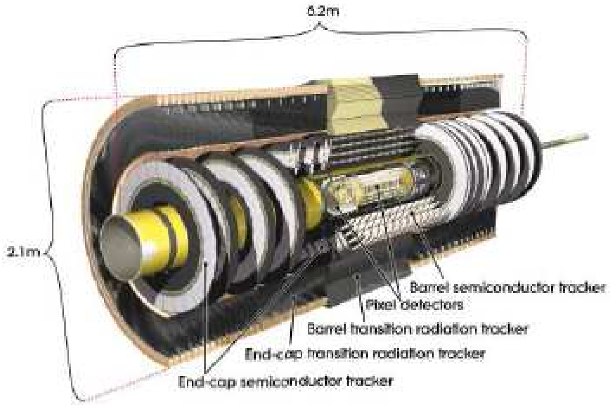

Figure 1.7: The layout of the Inner Detector.

particle impact parameters and the decay of short lived particles as B hadrons and τ leptons. A pixel sensor is composed by a 16.4 x 60.8 mm^2 silicon wafer with 46080 semi-conductor pixels, 50 x 300 μm^2 each. The system is composed by a total of 140 million of detector elements arranged in three barrels at average radii of 4, 10 and 13 cm and five end-cap disks on each side between radii of 11 and 20 cm, which complete the angular coverage.
In the intermediate radial range a *SemiConductor Tracker (SCT)* provides precise reconstruction of tracks as well as measurements of momentum, impact parameter and vertex positions. The barrel SCT uses eight layers of silicon microstrips detectors. Each silicon detector is 6.36 $\times$ 6.40 cm^2 with 768 readout strips of 80 μm pitch. Each module consists of four single-sided p-on-n silicon detectors. On each side of the module, two detectors are wire-bounded together to form 12.8 cm long strips. The end-cap modules are very similar and consist of strips of either 12 cm lenght at outer radii or 6-7 cm lenght at the innermost radii. Its high granularity is important for the pattern recognition.
The outer part of the ID is equipped with continuous tracking elements, the *Transition Radiation Tubes (TRT)*, based on the use of straw detectors. Each straw is 4 mm in diameter for a maximum straw lenght of 144 cm in the barrel. The tubes are arranged in 36 layers. The tubes are filled with a gas mixture that ionizes when a particle traverses it. A gold-plated tungsten wire in the middle of each tube collects the signal. Each layer is interspersed with a radiator to stimulate transition radiation from ultrarelativistic particles. The spatial resolution is about 200 μm.[11]

The Calorimetric System

Calorimeters in ATLAS absorb and measure the energy of charged and neutral particles, as well as jets. They also detect missing transverse energy by summing up all the measured energy deposits. Missing energy can be a sign of interesting new physics, such as the production of new weakly interacting neutral particles as neutralinos.
The ATLAS calorimetric system is composed by different calorimeters which cover different ranges of pseudo-rapidity. A pictorial view of the whole system is shown in figure 1.8.

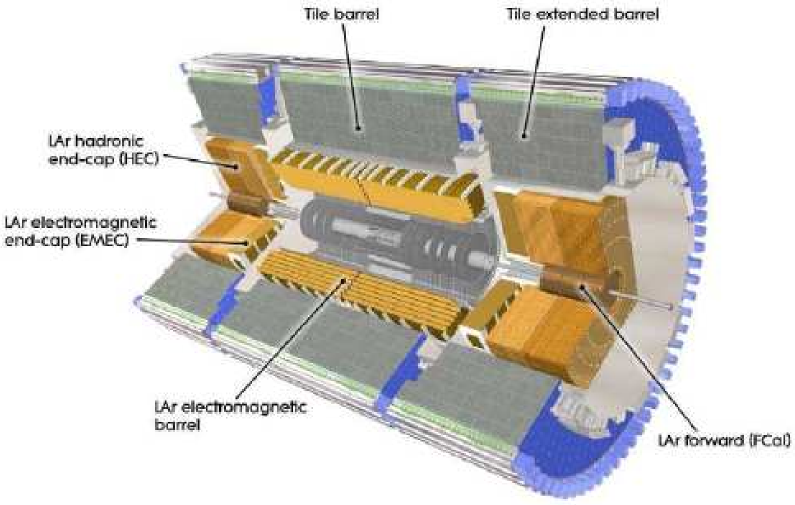

Figure 1.8: The ATLAS calorimetry system.

The **electromagnetic calorimeter** (EM Cal) is divided into a barrel part and two end-cap components. It is specifically designed to absorb and measure the energy of photons and electrons. The EM calorimeter is composed by liquid argon as active material, with accordion-shaped kapton electrodes, and lead absorber plates as passive medium. When a particle traverses the liquid argon gap, it creates charge by ionization. The signal is then collected on readout electrodes. The EM calorimeter is preceded by a presampler detector to correct for electron energy losses in the material upstream the EM calorimeter. The barrel component covers the pseudo-rapidity range of $|\eta| < 1.475$ while the two end-cap elements cover the range $1.375 < |\eta| < 3.2$. The total thickness of the EM calorimeter is > 24 radiation lengths (X_0) in the barrel and > 26 X_0 in the end caps. The EM calorimeter must be able to identify electrons and photons with energy between 5 GeV and 5 TeV. The energy measurements do not have to deviate from linearity more than 0.5%

to provide good resolution [11]. The energy resolution as measured in beam tests is:

$$\frac{\sigma_E}{E} = \frac{(9.23 \pm 0.09)\%}{\sqrt{E(GeV)}} \oplus (0.21 \pm 0.02)\% \tag{1.3}$$

The **hadronic calorimeters** are designed to absorb and measure particles that interact via the strong nuclear force. They consist of a *Hadronic Tile Calorimeter (HTC)* made of iron and plastic scintillator in the barrel region ($|\eta| < 1.7$), a liquid argon sampling calorimeter in the end-caps (*Hadronic End-Caps Calorimeter, HEC*) for $1.5 < |\eta| < 3.2$ coverage, and a *Forward Calorimeter (FCAL)*, very close to the beam pipe, made of liquid argon, iron and tungsten, that covers the region of $|\eta| < 5$. The thicknesses of the calorimeters have to be tuned in order to contain all the hadronic shower, to minimize the punch-through into the muon system and to provide a good resolution for high energy jets. The total thickness is 11 interaction lengths. The energy resolutions as measured in beam tests are:

- for the Tile Calorimeter (HTC)

$$\frac{\sigma_E}{E} = \frac{50\%}{\sqrt{E(GeV)}} \oplus 3\% \tag{1.4}$$

- for the HEC

$$\frac{\sigma_E}{E} = \frac{50\%}{\sqrt{E(GeV)}} \oplus 10\% \tag{1.5}$$

- for the forward calorimeter (FCAL)

$$\frac{\sigma_E}{E} = \frac{100\%}{\sqrt{E(GeV)}} \oplus 3\% \tag{1.6}$$

Muon Chambers

Only in a small fraction of pp collisions, high p_T events can be found for standard model processes, and an even smaller fraction of events is expected to correspond to new physics. Muons at high p_T or isolated ones are more common in interesting events than in background and thus provide an important signature used by the trigger system.

The muon spectrometer in ATLAS has been designed to be efficient in the muon detection and, in principle, should be able to measure the momentum without the help of the Inner Detector.

The muon chamber system, with its outer diameter of 22 m, represents the extreme outer layer of the ATLAS detector (see figure 1.9). The muon system is instrumented with separate trigger and high-precision tracking chambers for excellent

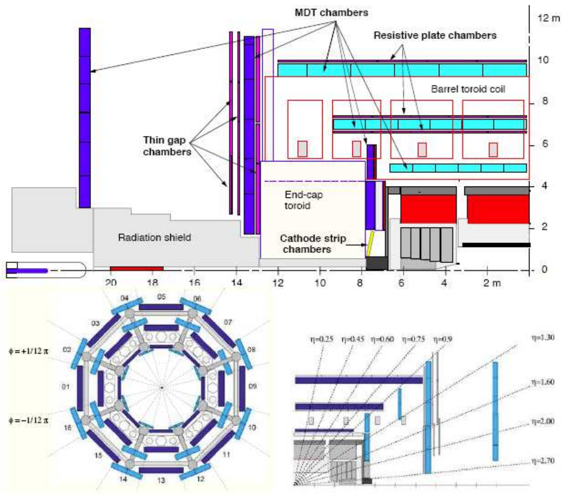

(a) ϕ-binning (b) η-binning

Figure 1.9: ATLAS muon spectrometer layout.

momentum resolution.
The tracking chambers are *Monitor Drift Tube (MDTs)* chambers and *Chatode Strip chambers (CSCs)*. The MDT chambers provide precise muon tracking over most of the pseudo-rapidity range. The tubes are made of aluminum and have a diameter of 30 mm. The resolution on the drift distance is about 80 μm [12].
The CSCs cover the pseudo-rapidity range of $1 < |\eta| < 2.7$. They are multi-wire proportional chambers with cathodes segmented into strips. The spatial resolution on the precision coordinate is about 60 μm [12].
The trigger system covers the range $|\eta| < 2.4$. *Resistive Plate Chambers (RPCs)* are used in the barrel and *Thin Gap Chambers (TGCs)* in the end-caps. The trigger chambers (RPC and TGC) have a 3-fold purpose:

- bunch-crossing identification, with a time resolution better than the LHC bunch separation of 25 ns;
- trigger with well defined p_T threshold requiring a granularity of the order of 1 cm;
- measurement of the second coordinate orthogonal to the one measured by precision chambers with a typical resolution of 5-10 mm.

1.2.2 The Forward Detectors

In an advanced state of commissioning of ATLAS, an efficient and reliable luminosity measurement became an important issue for the search of new physics.

Different types of forward detectors have been designed and developed in ATLAS to accomplish this task according to the space left by the other subdetectors.

Luminosity measurements Using Cherenkov Integrating Detector (LUCID)

LUCID is a Cherenkov detector consisting of 2 symmetric modules installed at 17 m from the interaction point. Each arm is equipped with 20 projective aluminum tubes filled with C_4F_{10}. It covers a pseudo-rapidity range of $\eta = [5.6; 5.9]$. Full details of the LUCID detector are reported in chapter 3.
LUCID is dedicated to monitoring LHC luminosity, as fully described in chapter 5, and is designed to have a time resolution suitable to identify each bunch crossing.

Zero Degree Calorimeters (ZDC)

The ZDC was proposed as a tool for heavy ion collisions. It is able to count and measure the energy of the neutral particles at zero degrees with respect to the beam line that are not swapt away by the magnetic field in the beam pipe. Via the multiplicity of spectator neutrons, the collision impact parameter can be measured. The centrality of the collisions, in fact, is strongly correlated to the very forward (spectator) neutrons. In *pp* collisions ZDC serves as an additional minimum bias trigger.
ZDC runs as a subsystem of ATLAS and thus it allows to correlate its measurements with those observed in the main ATLAS subdetectors.

Figure 1.10: Left: Scheme of ZDC detectors. Each detector is located 140 m downstream on either side of IP1. The front modules are instrumented with coordinate readout system. Right: Position of one ZDC module in the tunnel.

ZDC layout and the position of one module in the tunnel are presented in figure 1.10. The ZDC detector is located at approximately zero degrees to the incident beams on either side of the interaction point of ATLAS, 140 m downstream in a slot inside the neutral beam absorber (Target Absorber Neutral, TAN), at the point where the beam pipe branches off into two pipes. The pseudo-rapidity range covered by ZDC is $|\eta| > 8.3$. ZDC is a sampling compact calorimeter composed of tungsten alloy as absorber material and quartz fibers, which generate and transmit the Cherenkov light produced by showers of secondaries to the readout system. Two types of quartz fibers are used: vertical quartz strips for energy measurements and horizontal quartz rods to provide position information. The quartz fibers guarantee low signal losses during the transmission of the signal itself. In addition they are radiation hard. MC simulations have demonstrated, in fact, that ZDC can stand radiation doses up to 5 Grad. At a luminosity of about $10^{33} cm^{-2} s^{-1}$ ZDC can survive without damages for few years, while at a luminosity of $10^{34} cm^{-2} s^{-1}$ for few months.

Beam Conditions Monitor (BCM)

Losses from the circulating beams, occurring far from the ATLAS region, will most likely be detected by machine protection devices. However, magnet failures occurring close to ATLAS are also possible. The primary goal of the BCM system is to detect the early signs of beam instabilities, and to protect the experiment by initiating a beam abort, if necessary. Moreover, BCM provides real-time monitoring of particle rate close to the interaction point and is able to distinguish between collisions and background events. The separation between signal and background is based on the timing of BCM signals.

BCM consists of two stations (forward and backward) of detectors each equipped with four modules. The sensors are required to tolerate doses up to 500 kGy or 10^{15} charged particles per cm^2 over the lifetime of the experiment. Each module includes four diamond sensors, which are readout in parallel. The stations are placed symmetrically around the interaction point, at $|z| = 1.84$ m and $r = 55$ mm. The pseudo-rapidity coverage is $3.9 < |\eta| < 4.1$. Equipped with fast electronics (2 ns rise time), the stations measure the arrival time, with respect to the LHC clock, of particles and their pulse height. This permits to distinguish events resulting from beam losses from those normally occurring in pp interactions. BCM also provides measurement of bunch-by-bunch luminosities in ATLAS by counting the number of collisions.

Absolute Luminosity For ATLAS (ALFA)

ALFA is a system of ultra-small-angle detectors, proposed to measure elastically scattered protons in the Coulomb-Nuclear Interference region. This measurement is needed for the determination of LHC absolute luminosity with an

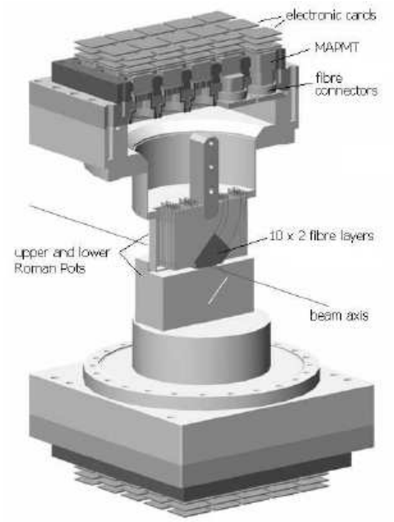

Figure 1.11: 3D view of an upper and lower detector and of the Roman Pots.

accuracy of 2-3%. This goal can be achieved by using special optics configuration: LHC running at high β^*, low luminosity and parallel-to-point focusing, to focus all the particles scattered at the same angle in the same position y at the detector position.

To measure the particles scattered at very small angles (about 3 μrad [13]), the detector must approach the beam to about 1.5 mm. The technology used to achieve this goal is the so-called *Roman Pot*, a system integrated with the beam pipe and able to move the detector close to the beam.

ALFA is made of two arms situated at 240 m from the interaction point at either sides of ATLAS. Each module is composed by 2 groups of scintillating plastic fibers of square cross-section (0.5x0.5 mm^2), at 90 degrees with respect to each other. The layout of the detector and of the Roman Pots is presented in figure 1.11. A tipical spatial resolution obtained with this configuration is about 30 μm. The pseudo-rapidity coverage range is $10.6 < |\eta| < 13.5$.

Radiation doses are not an issue for ALFA, due to the low luminosity running conditions.

Minimub Bias Trigger Scintillators (MBTS)

At the beginning of LHC data-taking, at the initial low luminosity of about $10^{27} cm^{-2} s^{-1}$, most of the bunch crossing did not produce any pp interaction. ATLAS has a dedicated experimental setup to trigger on minimum bias events, called *Minimum Bias Trigger Scintillators (MBTS)*, to reject empty events efficiently. MBTS helped commissioning other subdetectors by triggering on minimum bias

collisions.
The MBTS counters consist of a plane with 2x8 scintillator segments on each side of the interaction point at $|z| = 356$ cm, mounted in front of the LAr end-cap. The position corresponds to a pseudo-rapidity range of $1.9 < |\eta| < 3.8$.
MBTS survived the radiation damage of the first few months of data taking and contributed to the luminosity monitoring till luminosities up to about $10^{27} cm^{-2} s^{-1}$. At higher luminosity, with the use of bunch trains, separated in time by less than 75 ns, MBTS was not be usefull anymore: the leghts of its signals were, in fact, too long to separate collisions occurring in two different BCID.

1.2.3 ATLAS Trigger and Data Acquisition System

At design luminosity, ATLAS would produce about 1 Petabyte/second of raw data if all the *pp* collisions were recorded. However, most of the data comes from common, well-known processes that are of little interest to the experiment. The purpose of a trigger system is to select only the rare, interesting events while rejecting everything else.

The Trigger System

The Trigger System [14] selects bunch crossings containing interesting interactions. At the design luminosity there are about 25 interactions per bunch crossing leading to an interaction rate of about 10^9 Hz. The online triggering system must be able to select interesting physics signatures reducing the acquisition rate to approximately 100 Hz, the upper limit for the data storage. This goal is achieved with different trigger levels which successively refine the selection process: LVL1, LVL2 and LVL3 also called Event Filter (see figure 1.12).

- **Level 1 Trigger** All the subdetectors in ATLAS work at the full LHC bunch -crossing rate. Also the trigger electronics has to provide a decision on the data temporarily buffered in pipe line at the rate of 40 MHz. The LVL1 trigger uses reduced granularity data from only a subset of detectors, muon chambers and calorimeters, plus prescaled contributions from LUCID and MBTS. Then the LVL1 decides if one event can be stored or it has to be rejected. The time to form and to distribute the trigger decision, called latency, is 2 μs and the maximun rate is limited to 100 kHz by the capabilities of the LVL2 trigger input band width. During the LVL1 processing, the data from all subdetectors are held in pipeline memories in the front-end electronics. The LVL1 trigger must identify unambiguously the bunch crossing containing the interaction of interest introducing negligible dead-time.

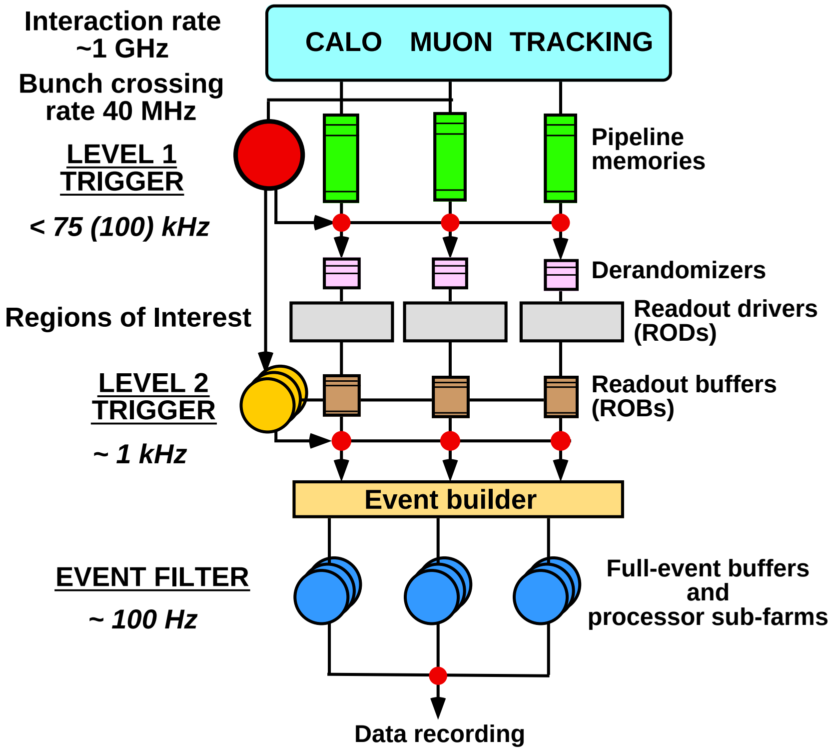

Figure 1.12: The ATLAS trigger and data acquisition systems.

- **Level 2 Trigger** The LVL2 trigger reduces the accepted rate from 100 kHz to 1 kHz, with a latency ranging from 1 ms to 10 ms depending on the event. Events passing the LVL1 trigger are held in so-called *Read Out Buffers (ROB)* until the LVL2 trigger takes the decision to either discard the event or accept it. After an event is accepted, the full data are sent to the Event Filter processor via the Event Builder. In order to reduce the data transfer bandwidth from the ROBs to the LVL2 trigger processors, the LVL2 algorithms work on subsets of the detector data called *Region of Interest (RoI)* and defined in the LVL1.

- **Event Filter** The Event Filter trigger uses the full event data together with the latest available calibration and alignment constants to make the final selection of events for permanent storage. At LVL3 a complete event reconstruction is possible, and the total latency is about 1 s. The Event Filter must achieve a data storage of 10-100 MB/s by reducing both the event rate and the event size.

LV2 trigger and Event Filter are called together *High Level Trigger (HLT)*.

Data Acquisition System

The Data Acquisition System (DAQ) is the framework in which the Trigger System operates. It receives and buffers the data from the detector-specific read out, called *Read Out Drivers (ROD)*, at the Level 1 trigger rate, and trasmits the data to the Level 2 trigger if requested. If an event fulfills the Level 2 selection criteria, the DAQ is responsible for building the event and moving it to the Event Filter. Finally, the DAQ forwards the final selected events to mass storage.

In addition to moving data down to the trigger selection chain, the DAQ provides an interface for configuration, control and monitoring of the ATLAS detector during data taking. Supervision of the detector hardware, such as gas system and power supply voltages, is handled by a separate framework called the *Detector Control System (DCS)*. Moreover, the DCS is responsible for alert and handling archiving.

1.2.4 Syncronization of Signals

The syncronization of the LHC experiments to the collisions is necessary to guarantee the quality of recorded data. LHC provides beam related timing signals to the experiments via optical fibers that are several kilometers long. The phase of the clock signals can drift, e.g due to temperature fluctuation, causing front-end electronics to sample at non optimal working points. The syncronization at ATLAS is provided by the *Beam Precision Monitor for Timing Purposes (BPTX)* system [15]. The BPTX stations are comprised of electrostatic button pick-up detectors, located at 175 m from the IP along the beam pipe on both side of ATLAS. BPTX are used to monitor the phase between collisions and clock with high accuracy in order to guarantee a stable phase relationship for optimal signal sampling in the subdetectors front-end electronics. In principle, the bunch structure of the beams as well as the number of protons in each bunch are measured by the BPTX system. In practice, BPTX can not measure $N_{1,2}$ with the precision required by luminosity measurements.

1.2.5 Measurements of Bunch Currents

Two complementary systems are used in ATLAS to evaluate the bunch currents with the precision required by luminosity measurements: the Fast Bunch-Current Transformers (FBCT) and the Direct-Current Current Transformers (DCCT) [16]. The *Fast Bunch-Current Transformers (FBCT)* are AC-coupled, high-bandwidth devices which use gated electronics to perform continuous measurements of individual bunch charges for each beam. The *Direct-Current Current Transformers (DCCT)* measure the total circulating intensity in each of the two beams irrespective of their underlying time structure. The DCCT have intrinsically better accuracy, but require averaging over tens of seconds to achieve the needed precision. The relative bunch-to-bunch currents are based on the FBCT measurements. The absolute scale of the bunch intensities is determined by rescaling the total circulating charge measured by the FBCT to more accurate DCCT measurements.

Chapter 2

Luminosity Measurements at Hadron Colliders

2.1 Introduction

The rate of physics processes produced at colliders is a function of both their cross section and the luminosity of the collider. The instantaneous luminosity, providing the event rate for unit cross section, depends on the number of particles circulating into the beams as well as the overlap integral of the beams. For two perfectly head-on beams, the higher the number of particles and the smaller the beam size, the higher the number of collisions. In order to discover rare processes high luminosity or, equivalently, high event-rate is a must.
The definitions of luminosity and its importance will be presented in section 2.2. The different methods used at LHC to measure the luminosity will be presented in section 2.3, with particular attention to ATLAS strategy.

2.2 Luminosity Overview

2.2.1 Instantaneous and Integrated Luminosities

The *instantaneous* luminosity $\mathscr{L}$ is defined as the ratio between the interaction rate R of any process and its cross section σ. It is expressed in units of $cm^{-2}s^{-1}$ and it is independent of the process itself.

$$\mathscr{L} = \frac{R}{\sigma} \tag{2.1}$$

The instantaneous luminosity can be inferred from the machine parameters: if the two beams are made of identical bunches, these are Gaussian in shape and perfectly overlapping without crossing angle, the luminosity is given by:

$$\mathscr{L} = f_r n_b \frac{N_1 N_2}{4\pi\sigma_x\sigma_y} \tag{2.2}$$

where $\sigma_{x,y}$ are the gaussian transverse profiles of the beams, e.g. the standard deviations of the bidimentional gaussians, N_1 and N_2 are the number of protons in the bunches of beam 1 ans 2, n_b is the number of bunches and f_r is the beam-revolution frequency.
The *integrated* luminosity L is obtained by integrating the instantaneous luminosity over a certain time interval t and is expressed in units of cm^{-2}:

$$L = \int_0^t \mathscr{L}(t')dt' \tag{2.3}$$

At LHC, the instantaneous luminosity is expected to decrease by 1% every 10 minutes according to the power law:

$$\mathscr{L} = \mathscr{L}_0 e^{-\frac{t}{\tau}} \tag{2.4}$$

where $\tau \simeq 14$ h.

2.2.2 Delivered and Recorded Luminosities

Luminosity estimates can be influenced by the live-time (or dead-time) of the detectors as well as of the data acquisition system.
The *delivered luminosity* is defined as the luminosity made available by the accelerator at a certain interaction point. The *recorded luminosity* is defined with respect to a trigger chain T and refers to the fraction of time when the trigger chain T was active. This excludes for example bunch-crossing that occurs during dead-time.
The delivered luminosity is evaluated before any trigger decision and therefore does not experience the dead-time of the data acquisition system. Since all data-sets used for analysis are exposed to dead-time, the final goal is to find the recorded luminosity corresponding to the data-set in question: the delivered luminosity needs to be transformed into recorded luminosity by correcting for dead-time.

2.2.3 Luminosity for Physics Analysis

For many measurements of cross sections and branching ratios at the LHC, the uncertainty on the integrated luminosity dominates the final accuracy. One prominent example is the measurement of the $H \rightarrow ZZ^*$ decay. The expected precision on the measurements of the Higgs production times the branching ratio to ZZ^* is about 12% if one assumes the luminosity is known at 10% level; this level improves to 6% when the luminosity is known up to 5%. As shown if figure 2.1, dropping the uncertainty in the luminosity by one half, in the mass region where the Higgs is expected, gives a drop by one half in the uncertainty on the cross section.

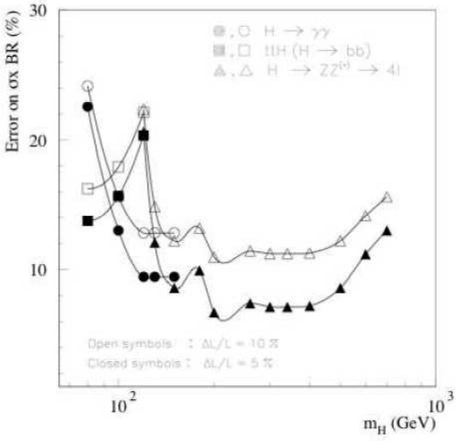

Figure 2.1: Expected systematic uncertainty on the measurement of the Higgs boson production cross section times branching ratio as a function of the Higgs mass, assuming an integrated luminosity of $300 fb^{-1}$. Results are shown for various decay channels and two values of the systematic uncertanity on the luminosity (10% and 5%)

2.2.4 Luminosity Monitor for Beam Tuning

Measuring the instantaneous luminosity is important to monitor the beam conditions and to use it efficiently. At LHC so called *mini lumi-scans* are used to center the beams on each other in the transverse plane at the beginning of each fill. Mini lumi-scans consist in activating closed-orbit bumps around the IP, which vary the position of both beams by $\pm 1\sigma$ in opposite directions, either horizontally or vertically. A closed orbit bump is a local distortion of the beam orbit that is implemented using pairs of steering dipoles located on either side of the affected region. In this particular case, these bumps are tuned to translate either beam parallel to itself at the IP, in either the horizontal or the vertical direction. The relative positions of the two beams are then adjusted, in each plane, to achieve the optimum transverse overlap, as inferred from the measurement of the interaction rate.

2.3 Luminosity Measurements at LHC

All the experimental techniques implemented at LHC to measure both the integrated and the instantaneous luminosity are presented in the following sections. These techniques can be divided in *direct* and *indirect* ones. In *direct* measurements, such as the so-called *Van der Meer scan* method or the *beam gas interaction* method, the absolute luminosity is inferred from bunch properties. In *indirect* measurements, information on physics processes, like their measured rates and cross sections, are used. The measured rate, for example, is only proportional to the absolute luminosity and it is referred to as *relative* luminosity.

2.3.1 Absolute Luminosity Measurements

Luminosity from LHC Parameters

The absolute luminosity can be obtained from the machine parameters, such as geometrical and kinematic characteristics of the beams, under specific beam conditions [17]. The method relies on measuring the individual beam shapes and determining the overlap integral which enters into formula 2.5. With this method the absolute luminosity can be estimated individually for each colliding bunch pair. The luminosity for two counter-rotating bunches (labelled 1 and 2) with time- and position-dependent density function $\rho_1(\vec{x},t)$ and $\rho_2(\vec{x},t)$ is given by:

$$L = f_r N_1 N_2 \sqrt{(\vec{v_1}-\vec{v_2})^2 - \frac{(\vec{v_1}\times\vec{v_2})^2}{c^2}} \times \int \rho_1(\vec{x},t)\rho_2(\vec{x},t) d^3x dt \tag{2.5}$$

for the case where the particles in each bunch are all moving with the same velocity $\vec{v_1}$ and $\vec{v_2}$ in the laboratory reference frame. In the formula f_r is the bunch revolution frequency and N_1 and N_2 are the number of particles in the corresponding bunches. The particle density functions $\rho_1(\vec{x},t)$ and $\rho_2(\vec{x},t)$ are normalized such that they have a unitary integral over the full space. Assuming that the two bunches are identical in the transverse profile, that their charge distribution on the plane perpendicular to the direction of motion is gaussian, that the profiles of the bunches are indipendent of the position along the bunch, and that the particle distributions are not altered during collisions, the previous equation can be written as [18]:

$$L = f_r \frac{N_1 N_2 n_b \gamma}{4\pi\epsilon_n \beta^*} F \tag{2.6}$$

where n_b is the number of bunches per beam, γ is the relativistic factor, ϵ_n is the normalized transverse emittance, β^* is the *beta function* of Coutant-Snyder [19] at the collision point and F is a reduction factor due to the crossing angle at the IP.

F is defined by [18]:

$$F = \frac{1}{\sqrt{1+\left(\frac{\theta_c \sigma_z}{2\sigma^*}\right)^2}} \tag{2.7}$$

where θ_c is the crossing angle between the two beams at the IP, σ_z is the mean square length of the bunches along the z axis and σ^* is the transverse dimension of the bunches.
The beam emittance is defined as:

$$\epsilon = \frac{6\pi\left(w^2 - D\left(\frac{dp}{p}\right)^2\right)}{\beta^*} \tag{2.8}$$

where w is the width of particle beams, dp/p is the momentum spread of the particle in the beams, D is the value of the dispersion function and β^* is the beta function. Both D and β^* must be evaluated at the measurement point in the particle accelerator. The β^* value is defined as the distance from the IP where the beam size is double with respect to the one at the IP. The lower β^*, the smaller the transverse size of the beam. If the two bunches are Gaussian and perfectly overlapping without crossing angle, the luminosity reduces to formula 2.2.
The bunch number and orbit frequency are well known.

Van der Meer Scan Method

An attractive method to measure the absolute luminosity without any a priori knowledge of any cross section or assumption on the beam shape is the so-called *Van der Meer scan* method [20]. The final formula obtained from this method is quite general and only depends on the assumption that there is no correlation between particle density distributions in x and in y. This method was invented in 1968 by S.Van der Meer [21] who found that it was possible to measure the effective height of the colliding ISR beams by observing the counting rate in a suitable detector while scanning one of the two beams in the vertical plane with respect to the other one. The measurement of the counting rate versus the displacement would yield a bell-shaped curve with its maximum at zero displacement. The value of the effective beam width in the vertical plane is, irrespective of the beam shape, equal to the area under the curve, divided by the ordinate at zero displacement.
At LHC the method consists in moving the beams transversely with respect to each other while recording the counting rate of at least one luminosity monitor. Separation scans are performed in both the vertical and horizontal directions. The position of maximum rate is thus found and the absolute luminosity is inferred from the measured beam overlap which is related to the area under the curve, as shown in figure 2.2.

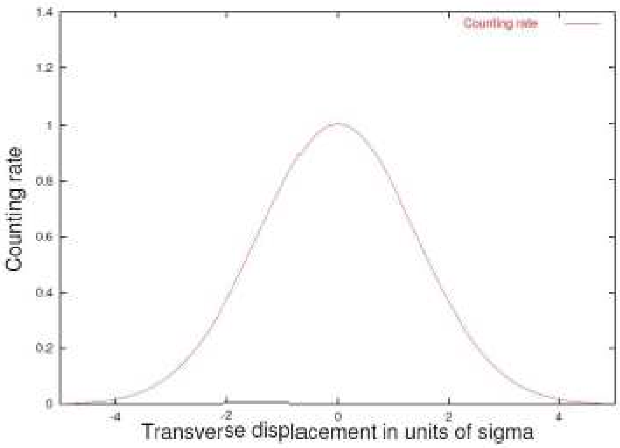

Figure 2.2: Example of the dependency of the counting rate on the beam displacement during a Van der Meer scan.

In terms of colliding beam parameters, the luminosity is defined as:

$$L = n_b f_r N_1 N_2 \int \rho_1(x,y)\rho_2(x,y)dxdy \tag{2.9}$$

where n_b is the number of colliding bunches, f_r is the machine revolution frequency (11245.5 Hz for LHC), $N_{1(2)}$ is the number of particles per bunch in beam 1(2) and $\rho_{1(2)}(x,y)$ is the particle density in the transverse plane (x-y) of beam 1(2) at the IP. Under the general assumption that there is no correlation between x and y, the luminosity can be written as:

$$L = n_b f_r N_1 N_2 \Omega_x(\rho_1(x)\rho_2(x))\Omega_y(\rho_1(y)\rho_2(y)) \tag{2.10}$$

where:

$$\Omega_x(\rho_1,\rho_2) = \int \rho_1(x)\rho_2(x)dx \qquad \rho_1(x) = \int \rho_1(x,y)dy \tag{2.11}$$

Ω_x is the beam overlap integral in the x direction, with an analogous definition for the overlap integral in the y direction. With the Van der Meer method the overlap integral can be calculated as:

$$\Omega_x(\rho_1,\rho_2) = \frac{R_x(0)}{\int R_x(x)dx} \tag{2.12}$$

where $R_x(x)$ is the rate at displacement x. We define Σ_x by the equation:

$$\Sigma_x = \frac{1}{\sqrt{2\pi}}\frac{\int R_x(x)dx}{R_x(0)} \tag{2.13}$$

When $R_x(x)$ is Gaussian, Σ_x coincides with the standard deviation of the rate distribution. By using equations 2.12 and 2.13, the luminosity can be rewritten as:

$$L = \frac{n_b f_r N_1 N_2}{2\pi \Sigma_x \Sigma_y} \tag{2.14}$$

which is the general formula to extract luminosity from machine parameters by performing a beam separation scan.

Physics Channels

It is possible to measure the absolute luminosity by counting the occurrencies of very well understood physics processes, with sufficient cross section and very clear experimental signature. The main idea is to measure the rate of these well-known channels taking care for background subtraction and then evaluate the luminosity by using equation 2.1.
Candle channels are Z/W production and decay into leptons, and lepton pair production via double-γ exchange.

- **Z/W decaying into lepton pairs**
  LHC can be considered as a Z/W factory: plenty of Z/W electroweak bosons will be produced, with expected rate of about 20 Hz for Z and 200 Hz for W at $L = 10^{34} cm^{-2} s^{-1}$ [20]. In addition, their signature is very clear once leptonic decays are considered. For $Z \rightarrow l^+l^-$, two leptons with high transverse momentum and invariant mass close to the nominal value of Z mass are produced. For $W \rightarrow l\nu$ a lepton with high transverse momentum is produced, together with a neutrino resulting into missing transverse energy.
  At the beginning of LHC running, at low luminosity, the electroweak channels are used as cross checks for the measurements of the integrated luminosity, as presented in chapter 7. At high luminosity, when all systematics and theoretical uncertainties will be calibrated and well understood, the measured rate of Z/W production can be used as a luminosity monitor.

- **Two-photon production of lepton pairs**
  The process $pp \rightarrow ppl^+l^-$, whose Feynmann diagram is shown in figure 2.3 and where two muons (electrons) are produced, can provide a method to determine the integrated luminosity. Due to the high design luminosity of LHC, a lot of two-photon events are produced both at central and forward rapidities. These events can be easily identified inside the data streams thanks to their clear signature. The process is very well understood: the cross section

at 14 TeV and within the detector acceptance is $\sigma = 1.33 \pm 0.01$ pb for ATLAS and CMS and $\sigma = 0.88 \pm 0.01$ pb for LHCb [20]. All the three experiments are expected to measure the integrated luminosity from these electromagnetic channels with a statistical precision of few percent. These events can be used also as a luminosity monitor, but only after some fb^{-1} of data will be collected, due to the not very high cross section.

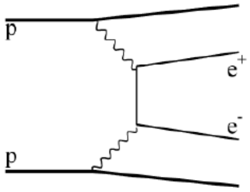

Figure 2.3: Feynmann diagram for the two-photon $pp \rightarrow ppll$ process.

Proton-proton Elastic Scattering

The absolute luminosity can also be determined by measuring the pp elastic scattering amplitude. The total (elastic and inelastic) counting rate is related to the luminosity and the total cross section by the expression:

$$\sigma_{tot} \cdot L = N_{inel} + N_{el} \tag{2.15}$$

where N_{inel} is the counting rate of inelastic events and N_{el} is the counting rate of elastic events. According with the optical theorem, the total cross section is directly proportional to the imaginary part of the forward elastic scattering amplitude extrapolated to zero momentum transfer $(-t)$ squared:

$$\sigma_{tot} = 4\pi Im[f_{el}(0)] \tag{2.16}$$

If the total rate R_{tot} of pp interactions as well as the rate of forward elastic scattering $dR_{el}/dt(t = 0)$ are measured, then the luminosity is derived from the relation:

$$L \frac{dR_{el}}{dt}\bigg|_{t=0} = R_{tot}^2 \frac{(1 + \rho^2)}{16\pi} \tag{2.17}$$

where ρ is the ratio of the real to imaginary part of the elastic forward amplitude. Both the total counting rate and the elastic scattering rate must be measurend with high precision. In order to measure $dR_{el}/dt(t = 0)$ a dedicated detector is required to tag proton scattering at very small squared-momentum-transfers, t; high and well known efficiency for detecting inelastic pp interactions is needed. The detector dedicated to the measurements of both R_{tot} and $dR_{el}/dt(t = 0)$ at LHC is *TOTal cross section, Elastic scattering and diffraction dissociation Measurements at LHC (TOTEM)* [22]. TOTEM is composed by two tracking telescopes installed on each side in the pseudorapidity region $3.1 \leq \eta \leq 6.5$ in Roman Pot stations at 140 m and 220 m from the IP of CMS. TOTEM is able to measure the total number of collisions as well as the number of forward elastic scattered events, through which the luminosity is evaluated using Eq. 2.17. TOTEM works at special running consditions of high $\beta^* = 1540$ m and thus low luminosity $L \sim 10^{28} cm^{-2}s^{-1}$. ATLAS does not have enought coverage in η to measure R_{tot} with sufficient precision. The approach is thus using the measurements of the elastic scattering provided by the ALFA detector. The total rate of scattering events is approximated by the relation:

$$\frac{dN}{dt} = L\pi(f_C + f_N)^2 \approx L\pi \left| -\frac{2\alpha_{EM}}{|t|} + \frac{\sigma_{tot}}{4\pi}(i+\rho)e^{-b|t|/2} \right|^2 \tag{2.18}$$

where the first term corresponds to the Coulomb and the second term to the strong interaction amplitude. α_{EM} is the electromagnetic fine-structure constant and b is the nuclear slope for pp scattering. The trend of the general dependency of scattering rate on the momentum transfer is shown in figure 2.4.

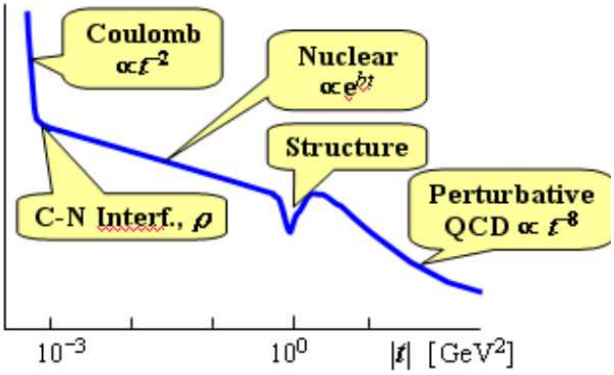

Figure 2.4: Dependency of pp scattering rate on the t-value.

If ALFA will be able to measure the elastic scattering down to such small t-values that the cross section becomes sensitive to the electromagnetic amplitude via the Coulomb Interference term, the luminosity, total cross section, b and ρ are extracted simultaneously from the fit of the event rate in the Coulomb-Nuclear Interference (CNI) region.

If the CNI region will not be reached, an alternative solution will be to combine the measurement of the elastic scattering provided by ALFA with the value of $\sigma_{tot} = L \cdot R_{tot}$ obtained by TOTEM. An accuracy of few percent on the luminosity evaluation is expected. The measurement of the elastic scattering at very small angle (about 3μrad) requires special optics conditions (high $\beta^* > 1000$) which imply low luminosity. As a consequence, the luminosity measurement obtained with ALFA is not directly available for standard physics runs. However, it will provide a calibration for all the luminosity monitors running at the same time as ALFA [13].

2.4 Luminosity Measurements in ATLAS

Luminosity measurements in ATLAS are designed to reach three goals.

- Providing final absolute integrated luminosity values for offline analyses, for the full data sample as well as for selected periods. In addition, measurements of the average luminosity over small time intervals, called *Luminosity Block (LB)*, and for individual bunch crossings are required. The LB is defined as a time interval in which the luminosity can be considered constant. As a consequence, the LB must be smaller than the decay time of the beam. The luminosity must be provided for each LB. In physics analyses, in fact, data are used only if some quality criteria, provided LB by LB, are satisfied. To avoid discarting too many data, short LB are needed. Typical values of LB lenght are thus of the order of 1-2 minutes, to balance all the aspects mentioned before. Each LB is identify by a number which uniquely tags it within a run.

- Providing fast online luminosity monitoring, as required for efficient beam steering: machine optimization, as for example beam centering through mini-scans, as well as efficient use of the trigger. The fraction of recorded data, called *prescale*, in fact, can be changed according to the beam degradation in order to optimize at each time the data acquisition band width. A statistical precision of about 5% per few seconds and systematic uncertainties below 20% are desirable for the online luminosity.

- Fast checking of running conditions such as monitoring the structure of the beam and beam-related backgrounds.

Since there is no single experimental technique which can fullfill all the above requirements, a number of complementary measurements and detectors have to be considered: parallel measurements of absolute and relative luminosity are mandatory.

2.4.1 ATLAS Running Conditions in 2010

All the data analysed in the next chapters have been collected in 2010 *pp* runs. The first data in early 2010 have been taken at a center-of-mass energy of 900 GeV, while from March 2010 to November 2010 all the data have been recorded at the energy of 3.5 TeV per beam. The instantaneous luminosity has increased from $9.36 \cdot 10^{26} cm^{-2}s^{-1}$ at the end of March 2010, to $2.7 \cdot 10^{32} cm^{-2}s^{-1}$ at the beginning of October 2010. The growth of the peak luminosity during this period is reported in figure 2.5. The number of colliding bunches in Point 1 has increased from 1 in the very first runs, to 348 in the last runs and the average number of events per bunch crossing has grown from 0.00632 to 3.78. The growth of the instantanueous luminosity was due to the increase of the number of filled bunches, as well as the increase of the bunch currents and the emittance.

From November to December 2010, LHC has been running with heavy-ion with center-of-mass energy of 2.76 TeV for nucleon pair. The maximum number of filled bunches was 129. The growth of the peak luminosity during heavy-ion running is reported in figure 2.6: the instantaneous luminosity has increased from $3.695 \cdot 10^{23} cm^{-2}s^{-1}$ to $3.04 \cdot 10^{25} cm^{-2}s^{-1}$.

The total integrated luminosity both for *pp* running and for lead-ion running are visible in figures 2.7 and 2.8. The ratio of the recorded to delivered luminosity gives the ATLAS data taking efficiency of 93.6% for *pp* running and 94.6% for heavy-ion running. The inefficiency accounts for the turn-on of the high voltage of the Pixel, SCT and some of the muons detectors (about 2%) and any other inefficiencies due to the deadtime or to individual problems of a subdetector (4.4%).

All LHC records achieved during 2010 *pp* data taking at 3.5 GeV per beam are reported in table 2.1, while all the records reached during data taking with heavy-ion are reported in table 2.2.

Collision energy per beam	3.5 TeV
Peak Stable Luminosity Delivered	$2.07 \cdot 10^{32}$
Maximum Luminosity Delivered in one fill	6304.61 nb^{-1}
Maximun Luminosity Delivered in one day	5983.78 nb^{-1}
Maximum Colliding Bunches	348
Maximum Average Events per Bunch Crossing	3.78
Longest Time in Stable Beams for one fill	30.3 hours
Longest Time in Stable Beams for one day	22.8 hours
Longest Time in Stable Beams for 7 days	69.9 hours

Table 2.1: LHC records reached during 2010 *pp* data taking.

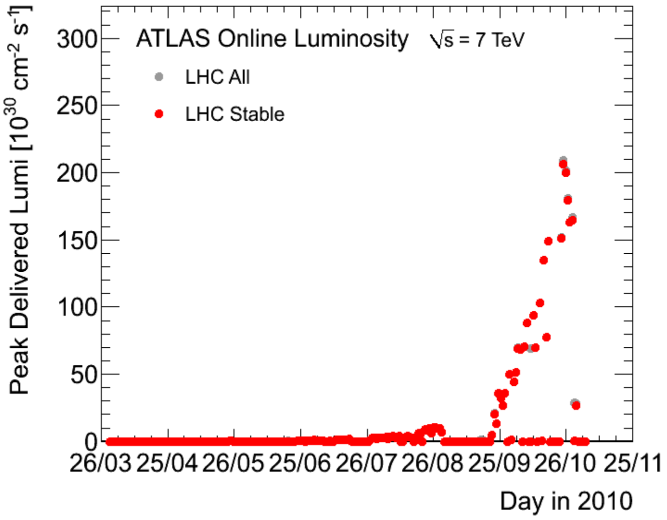

Figure 2.5: Peak of delivered luminosity as a function of time during 2010 pp running.

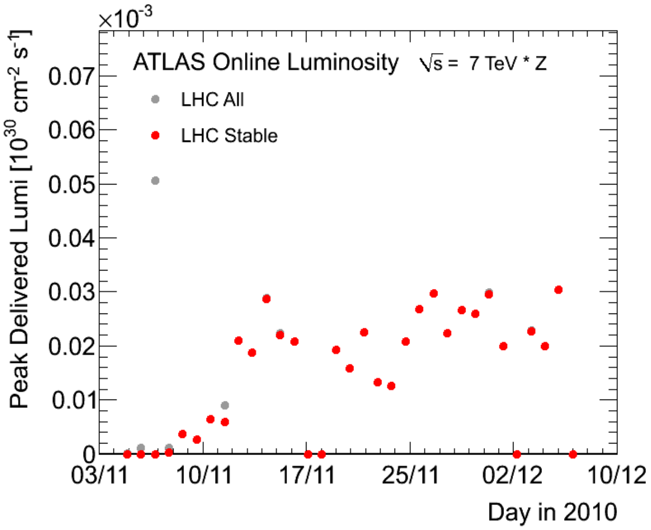

Figure 2.6: Peak of delivered luminosity as a function of time during 2010 heavy-ion running.

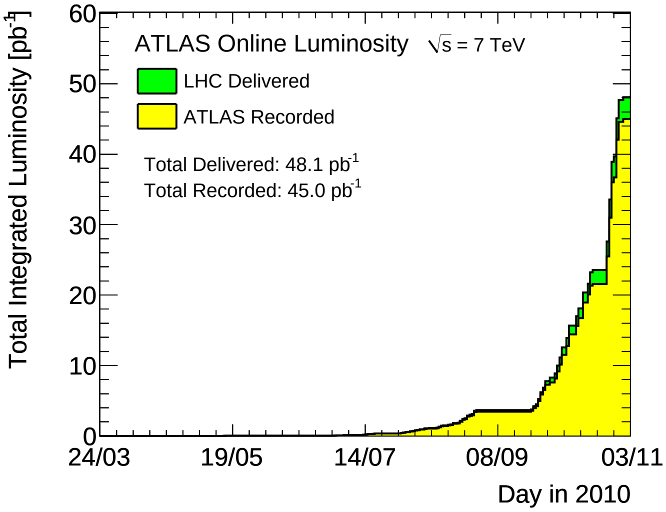

Figure 2.7: The integrated luminosity reported by day for pp running in the period April-October 2010. The total delivered in green and recorded in yellow luminosities are reported. The integrated luminosity delivered by LHC has increased from 0.008 nb^{-1} in April 2010 to about 50 pb^{-1} at the end of pp data taking.

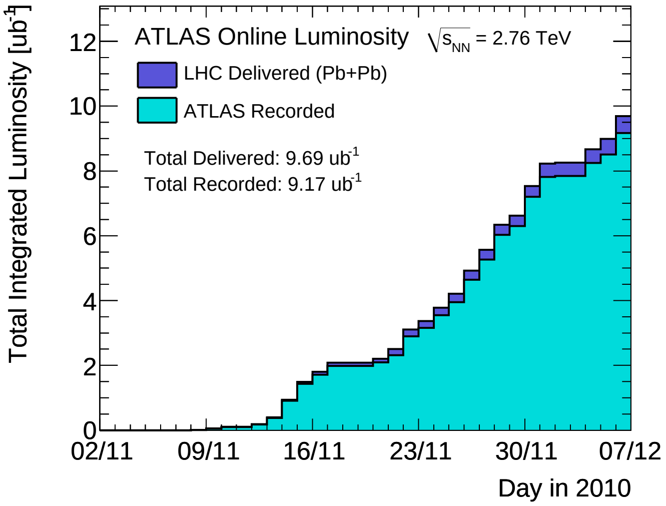

Figure 2.8: The total integrated luminosity reported by day for HI data taking in the period November-December 2010. The total delivered in blue and recorded in light blue luminosities are reported. The total integrated luminosity delivered by LHC from November to December 2010 is about 10 μb^{-1}.

Collision energy per nucleon	2.76 TeV
Peak Stable Luminosity Delivered	$3.04 \cdot 10^{25}$
Maximum Colliding Bunches	129
Longest Time in Stable Beams for one fill	13.9 hours
Longest Time in Stable Beams for one day	15.6 hours
Longest Time in Stable Beams for 7 days	79.0 hours

Table 2.2: LHC records reached during 2010 lead ion data taking.

2.4.2 Relative Luminosity Measurements

From the very beginning of running in 2010, ATLAS has been able to provide delivered relative luminosity thanks to the different monitors it is equipped with. The luminosity monitors provide the measurements of the instantaneous luminosity at two different frequencies. First, the luminosity monitors evaluate the instantaneous luminosity at the frequency of about 1-2 Hz. These fast measurements are typically BCID blind. At least one of these measurements is communicated to the LHC for machine operations. Second, the instantaneous luminosity is provided LB per LB on bunch-by-bunch basis. These measurements are used for physics analysis. In summary, the luminosity is provided both integrated over all the bunch crossing and on bunch-by-bunch basis.

The response of a luminosity monitor ought to be linear over a large dynamic range, fast, stable in time and stable under different beam conditions. The main goal of these luminosity monitor detectors is to reach a stability better than 2%.

A list of the ATLAS monitors for the delivered luminosity with their main features is reported in table 2.3.

Detector	*Pseudo-rapidity range*	*Luminosity range* ($cm^{-2}s^{-1}$)	*Resolution*
LUCID	[5.6;5.9]	$10^{27} \div 10^{34}$	BX
MBTS	[1.9;3.8]	$10^{27} \div 10^{33}$	
BCM	[3.9;4.1]	$10^{27} \div 10^{34}$	BX
ZDC	>8.3	$10^{27} \div 10^{34}$	

Table 2.3: ATLAS monitors for the delivered luminosity with their main characteristics.

Among all the luminosity monitors, only LUCID has been operational during the

whole running period in 2010. MBTS has been able to provide measurements of the delivered luminosity only during the very first months, during which the luminosity remained below $10^{27} cm^{-2} s^{-1}$ and the filled bunches were separated in time by more than 75 ns. At higher luminosity with the use of bunch trains, separated in time by less than 75 ns, MBTS was not be usefull anymore: the leghts of its signals were too long to separate collisions occurring in two different BCID. ZDC has been in phase of commissioning till the beginning of the heavy-ion running. Due to hardware problems, BCM was operational from the middle of the 2010 running.
A measurement of the recorded luminosity was provided also by both the Tile and the Liquid Argon calorimeters, which use quantities derived from the analysis of the ATLAS data stream. The measurements of the recorded luminosity have been used mainly to control the algorithms used by the monitors of table 2.3 to evaluate the delivered luminosity. The main characteristics of the detectors for the recorded luminosity measurements are listed in table 2.4.

Detector	*Pseudo-rapidity range*	*Luminosity range* $(cm^{-2}s^{-1})$
Tile Calorimeter	[-1.7;1.7]	$10^{27} \div 10^{34}$
Liquid Argon	[-5.0;5.0]	$10^{27} \div 10^{34}$

Table 2.4: ATLAS monitors for the recorded luminosity with their main characteristics.

Due to the features of the LUCID detector, it has been considered the *preferred* luminosity monitor during all the *pp* running in 2010. More details about LUCID strategy to measure the luminosity are reported in chapter 5.

Absolute Luminosity Measurements

All the results obtained from the luminosity monitors have to be calibrated using at least one measurement of the absolute luminosity.
A very preliminar calibration of relative luminosity was based on Monte Carlo predictions for the inelastic *pp* cross section, since no *pp* data at 7 TeV were available yet. The precision obtained with this calibration was about 20%. More details on the Monte Carlo based calibration are reported in chapter 5.
During 2010 data taking, four Van der Meer scans were performed. From the analysis on the first three scan data, the calibration constants for all the luminosity monitors were evaluated and the absolute luminosity was provided with an accuracy of about 11%, dominated by the uncertainty on the bunch currents provided directly by LHC. Analysis on the fourth scan is still ongoing, but, from a first

estimation, including these data set, the accuracy of 3.4% is reached. Full description of the first three Van der Meer scan data analyses for the LUCID detector is reported in chapter 6.

During the winter shutdown in 2011, the installation of the ALFA detector was completed. ALFA will use the measurement of the elastic cross section at very small angles to provide an absolute luminosity measurement. With ALFA, calibrating relative luminosity with an accuracy of about 2-3% will be possible.

Finally, accurate measurements of absolute luminosity should be obtained measuring the number of produced Z and W. A preliminary analysis of the Z production is reported in chapter 7.

Chapter 3

The LUCID Detector

3.1 Introduction

The main luminosity monitor in ATLAS is a dedicated detector called LUCID (*Luminosity measurements Using Cherenkov Integrating Detector*). The intrinsically fast response of the detector and its readout electronics make it ideal to measure the number of interactions at each bunch crossing. A dedicated electronic board performs the on-the-fly evaluation of the LHC luminosity with different algorithms. More details on the algorithms are presented in chapter 5. In this chapter the LUCID design, as well as its read-out electronics, will be presented.

3.2 Design

The main intent of LUCID is to monitor the inelastic collision rate with sufficient efficiency and low sensitivity to the background. The idea is to count the mean number of inelestic *pp* collisions through the number of charged particles that are produced in each collision within the LUCID acceptance.
The LUCID apparatus is composed by two symmetric arms installed around the beam pipe at about 17 m from the interaction point, as shown in figures 3.1 and 3.2. Each arm is composed by a conical aluminum vessel housing 20 mechanically polished aluminum tubes pointing to the interaction point. The tubes are arranged in two rings at 9.6 cm and 11.5 cm from the beam line. Each tube has a diameter of 15 mm and is 1500 mm long. A schematic view of the pointing geometry of LUCID is presented in figure 3.3.

The internal walls of the tubes have a reflecting index from 0.92 to 0.98 [23] in the wavelength range from 400 to 600 nm, region in which the PMTs are mostly

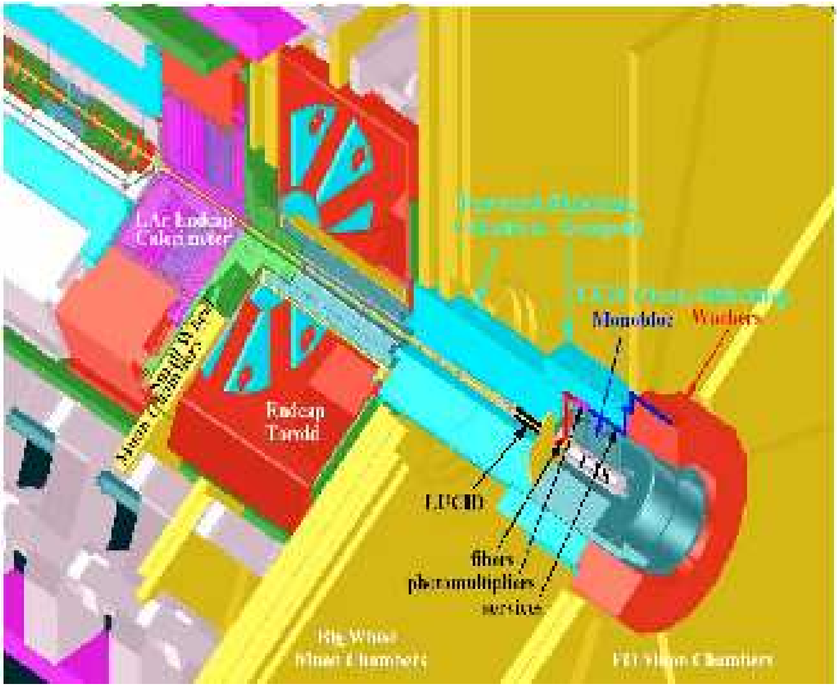

Figure 3.1: LUCID position scheme inside ATLAS.

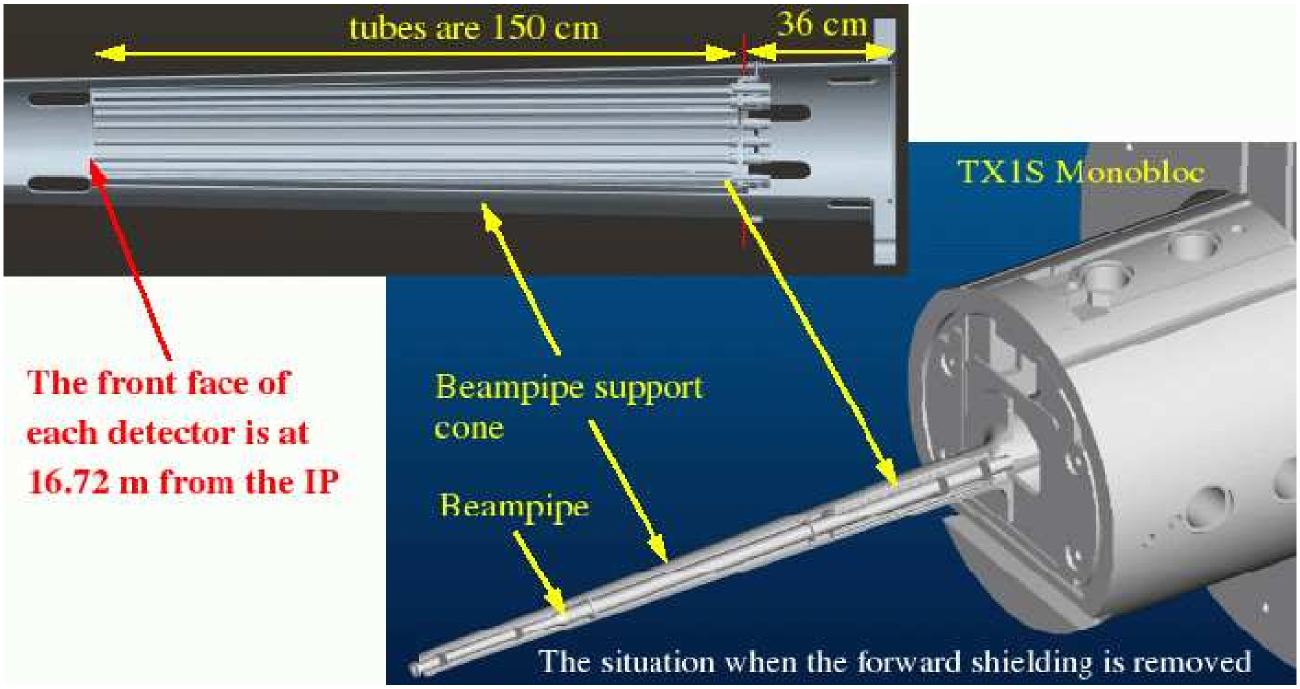

Figure 3.2: Details of LUCID position near the beam pipe.

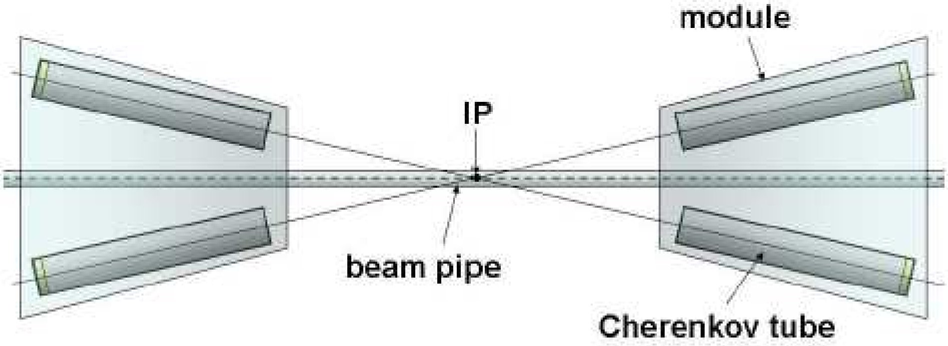

Figure 3.3: Schematic view of the pointing geometry of four LUCID tubes (not in scale).

sensitive. The tubes are filled with C_4F_{10}, a high refractive index (n = 1.00137, at standard temperature and pression) Cherenkov radiator gas kept at a pressure of about 1.1 bar.
When a charged particle enters a tube, Cherenkov light is emitted at an average angle of 3° with respect to the particle trajectory. The light undergoes multiple reflections on the aluminum walls till it reaches the tube end. In 16 out of the total 20 tubes, the light is collected by a photomultiplier directly coupled with the tube. The others 4 tubes end up in a small aluminum cone concentrating the light on a fiber bundle (5 m long) that in turn brings the light to a lower radiation area, where a multianode photomultiplier reads out the signals. Fibers readout is used only for study purposes, as a possible solution when LHC will be running at maximum luminosity.
All the principal characteristics of LUCID are reported in table 3.1.

η coverage	± [5.6;5.9]
N tubes.	20
Material	Mechanic. polished Al
Gas	C_4F_{10}
Pressure	1.1 bar
Cherenkov angle	3°
Signal duration	Few ns
Read-out	16 PMTs + 4 fibers
Expected dose	7 Mrad/y @ $10^{34} cm^{-2} s^{-1}$

Table 3.1: Main parameters per LUCID module.

The advantages of the LUCID design are that the detector is composed of light material, which is intrinsically radiation hard, and the detector response is fast, within few ns from the momentum a particle traverses the detector. The bandwidth of the electronics allow to keep the FWHM of the PMT signals at a level of 10 ns (fast baseline restoration). These characteristics ensure the capability to separate collisions coming from different bunch crossings (separated by 25 ns) and make LUCID suitable for online monitoring of the bunch structure.

3.3 Principle of Detection: Cherenkov Light Emission

Cherenkov light is emitted when a charged particle traverses a material with a velocity v larger than the speed of light in that medium (c/n):

$$v > \frac{c}{n} \rightarrow \beta = \frac{v}{c} > \frac{1}{n} \tag{3.1}$$

where n is the refractive index of the radiator. The minimal velocity at which the emission takes place (c/n) corresponds to a particle energy threshold E_{th}:

$$E_{th} = \gamma m_0 c^2 = \frac{m_0 c^2}{\sqrt{1-(\frac{v}{c})^2}} = \frac{m_0 c^2}{\sqrt{1-(\frac{1}{n})^2}} \tag{3.2}$$

where m_0 is the rest mass of the particle. In C_4F_{10} kept at 1.1 bar, $E_{th} = 2.7$ GeV for pions (π) and $E_{th} = 9.3$ MeV for electrons (e). In the quartz window of the PMTs, $E_{th} = 190$ MeV for π and $E_{th} = 0.7$ MeV for e.
The emission angle θ_c is a function of both the refractive index of the medium and the particle velocity:

$$cos\theta_c = \frac{1}{\beta n} \tag{3.3}$$

The number of photons emitted when a particle passes through the radiator medium is proportional to the length of the trajectory inside the medium (L) and depends on the Cherenkov angle (θ_c):

$$N_{pe} = N_0 \cdot L \cdot sin^2\theta_c \tag{3.4}$$

where N_0 is related to the efficiency of light collection (ϵ_{coll}) and to the quantum efficiency of the PMTs (ϵ_{PMT})

$$N_0 = 370cm^{-2}eV^{-1} \int \epsilon_{coll}(E)\epsilon_{PMT}(E)dE \tag{3.5}$$

The refractive index of a gas is a function of the photon energy (E), the pressure (P) and the temperature (T) of the gas [25]. In case of C_4F_{10}:

$$n = \sqrt{\frac{2x+1}{1-x}} \tag{3.6}$$

where

$$x = \frac{0.25938 \times P[bar]}{T[kelvin]} \cdot \frac{1}{1-\left(\frac{E[ev]}{17.0}\right)^2} \tag{3.7}$$

The value of the gas pressure was chosen to balance different effects. An increase of the pressure value results in an increase of the refractive index, as visible from Eq. 3.6. As a consequence the number of produced photoelectrons increases. However, with increasing refractive index, the Cherenkov angle decreases and the number of reflections of the photoelectron on the tube walls increases, resulting in a loss of the collected light. Moreover the pressure has to be kept at a value above the atmospheric one for mechanical problems of the support housing the PMTs in the vessel. To balance all the above mentioned effects the pressure value has been choosen of 1.1 atm.

The refractive index of C_4F_{10} and the aluminum tube reflectivity are also dependent on the wavelength of the incident light as shown in figure 3.4.

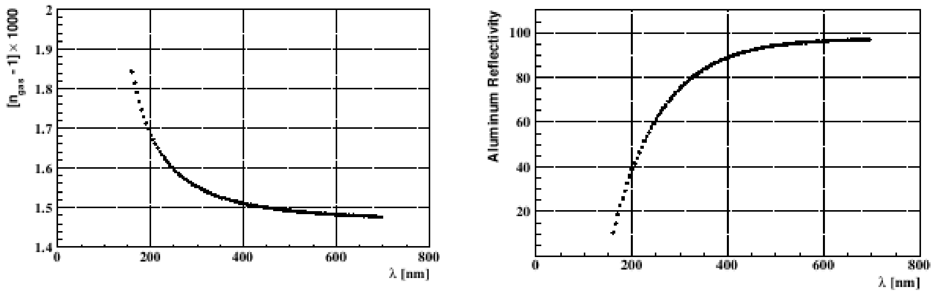

Figure 3.4: The dependency of the refractive index of C_4F_{10} (left) and of the aluminum tube reflectivity (right) on the wavelength.

Charged particles with $\beta \sim 1$ in C_4F_{10} generally emit Cherenkov light at an angle of 3°, resulting in 2.8 average number of reflections of the produced photons on the tube walls [26].

The signal from a *pp* collision is given by the contribution of two cathegories of particles: primary and secondary. Primary particles are produced at the interaction point directly in the *pp* collision or from a prompt decay of a primary particle. They travel along a straight trajectory until they reach the LUCID volume. Secondary particles are the product of primary particles interacting with any other material (beam pipe, detector, machine elements, etc...). They travel along scattered trajectories before reaching LUCID. Due to the pointing geometry of LUCID, primary particles typically enter a LUCID tube from the front and travel inside the tube along a path parallel to its axis. Secondary particles are likely to enter the tubes from the lateral walls and travel a shorter path inside the gas (see figure 3.5). Since light is emitted continuously over the tube lenght, a primary particle is expected to release a larger amount of Cherenkov light than a secondary particle. The pointing geometry of the tube configuration and proper threshold cuts on the PMT signals reduce the contributions of secondary particles.

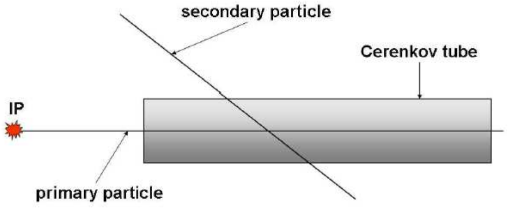

Figure 3.5: Scheme of a LUCID tube (not in scale). Comparison between the path travelled by a primary and a secondary particle.

3.3.1 Electronics

A partial schema of LUCID electronics is shown in figure 3.6.

The LUCID electronics consists of two logic sections: one section is dedicated to the luminosity measurements (CFD plus LUMAT card in figure 3.6) and is included in the ATLAS data stream called *global stream*; the other section is dedicated to the online monitor of the LUCID signals through a so-called *local stream* of data recorded asyncronously with respect to the ATLAS stream (CFD, QDC and FADC in figure 3.6).

The Local Stream

In order to monitor the luminosity with high stability, a deep understanding of the signal shape is mandatory. For this reason the LUCID electronics has been designed to allow a close control of the analog signals produced by the PMTs. Cherenkov photons hitting the PMTs are converted into a current. The analog signals from the PMTs are sent to amplifiers and differential line drivers placed close to the detector. The drivers send the data over 100 m of cable to the counting room. The signals are then received and zero pole compensated and forwarded to

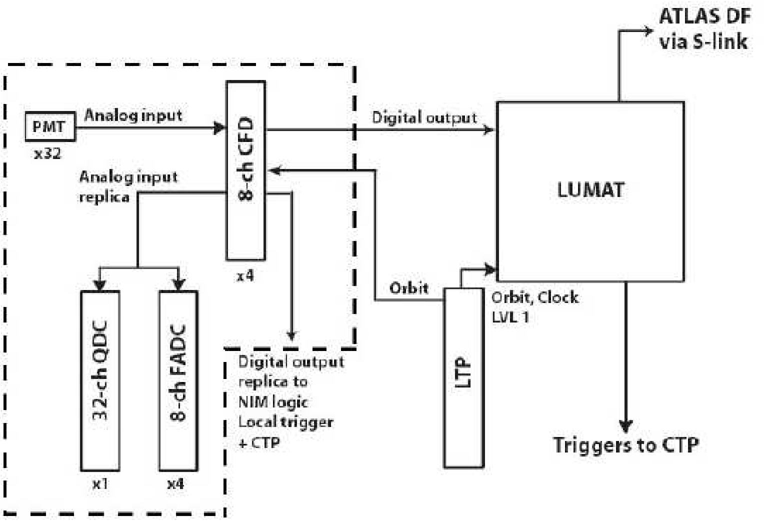

Figure 3.6: General schema of LUCID electronics.

four eight-channel discrimination units (CFD, Constant Fraction Discriminator). The CFDs provide two types of outputs: an amplified copy of the original input signals and a logical signal (TTL logic) of 10 ns of duration set to true when the input is above a programmable threshold. The CFD thresholds were initially set to 15 photoelectrons to keep the background at the level of 1 Hz, providing high efficiency to detect the first *splash* events. In September 2008 the LHC beam was injected with only one filled bunch and stopped by the collimator near ATLAS. The interaction of the protons with the dense material produced ”splashes” of secondary particles that travelled several hundred metres and passed through the detector. A majority of the subdetectors were operational so saw these splash events, as LUCID did.

The analog signals from the CFDs are sent to analog-to-digital converters (both QDC and 250 MHz flash ADC) for signal monitoring and calibration. The QDC is an integrating device which measures the total signal charge in unit of QDC counts over a window of time, called gate, of programmable duration. A typical charge distribution from a PMT is shown in figure 3.7.

The FADCs sample the signals every 4 ns for a programmable time window. For each tube the shape of the incoming signal is reconstructed, as shown in figure 3.8. The signal amplitude is given by the difference of two quantities: the baseline, at about 50 mV for all tubes, and the peak position. The position of the signal peak is evaluated by interpolating the three samples around the peak with a polinomial of second order. Integrating the signal produced by the FADC, the charge can be measured as well. The charge obtained with the FADC has been compared to the one obtained with the QDC. The two results are compatible between the errors on the measurements. It was decided to use only the QDC evaluation of the charge because the measurement is more precise. Once the time separation bewteen the bunches will be smaller than the QDC gate (80 ns), the charge will be evaluated only with the FADC.

Combining the information from QDC and FADC modules, the relation between the integrated charge and the amplitude of the signals is evaluated, as presented

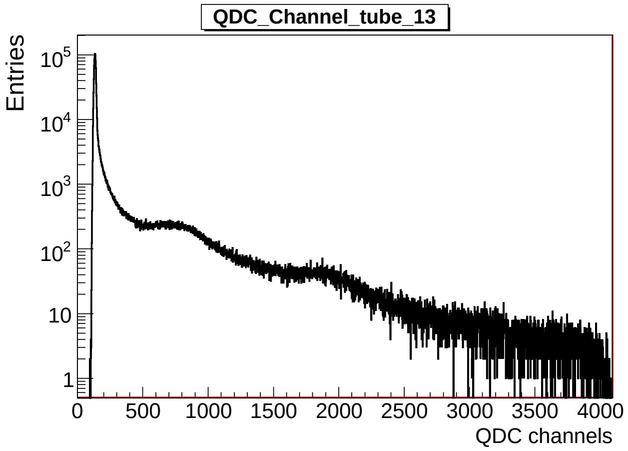

Figure 3.7: Example of the charge distribution collected by a PMT when a particle enters a tube as measured by the QDC module. The QDC integrates the charge from a PMT over a time window of 80 ns (gate).

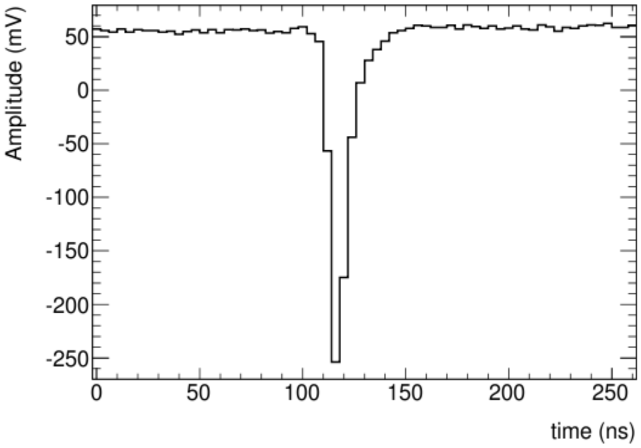

Figure 3.8: Example of the shape of the signal produced by a PMT when a particle enters a tube as sampled by the FADC module. The FADC samples the signal every 4 ns.

in figure 3.9. More details about this dependency will be provided in chapter 5.

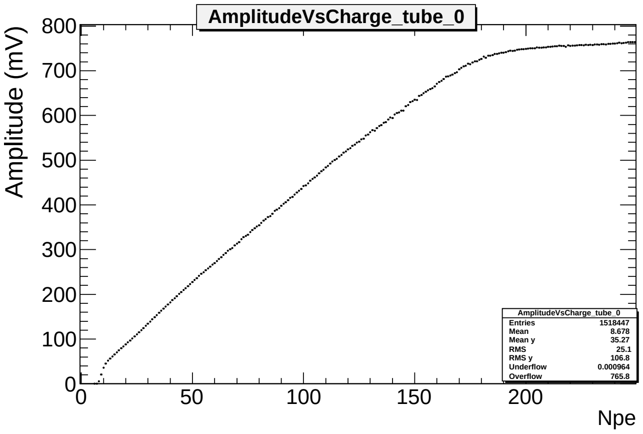

Figure 3.9: Example of the dependency of the amplitude measured by the FADC on the integrated charge provided by the QDC.

The charge distribution from the QDC needs to be calibrated to define the exact relation between QDC counts, an arbitray unit without physical meaning, and number of photoelectrons produced by the PMTs. The calibration is mandatory to compare the real data and the physics predictions, which are in number of photoelectrons. The process of calibration makes use of a system of 2 LEDs mounted on one end of a bundle of optical fibers that bring the light to the LUCID tubes. The LEDs have wavelengths of 340 and 395 nm. All the fibers are illuminated by whichever one of the LEDs is turned on. During the calibration the readout is triggered by a pulser syncronized with the LED blinking frequency. The intensity and the pulse duration of the LEDs signals can be adjusted so that one photoelectron is emitted from the photocathode of the PMT most of the time. The calibration makes uses of single photoelectron charge distributions. How the QDC bins are transformed in number of photoelectrons will be discuss in details in chapter 4. The QDC has a total range of 4096 channels, but the linearity is guarantee only to about 3500 channels. From Monte Carlo simulation, about 250 photoelectrons at maximum are expected from beam data. As a consequence the calibration constant has been fixed to 15 QDC bins to exploit all the dynamic range of the electronics during physics runs. During calibration runs, the signal output are much smaller than in physics runs, so that an additional amplification of a factor 2 is applied.

The 32 charges from PMTs as measured by the QDC and 32 vectors containing the sampling of the PMT signal obtained with the FADCs provide the event for the LUCID local data stream. The read-out trigger for the local stream is defined as the logic OR of the logic outputs of the four CFDs. It is implemented with standard NIM modules giving the gate to the QDC and the trigger to the FADC. The readout is handled in a slightly different way by the FADC and the QDC. In the case of the FADC, the signal shape data is kept in a buffer which is promptly read out upon request. The QDC, on the other hand, becomes active only when a readout request is received (the gate from the CFD trigger). When a trigger occurs, all the 32 channels are read out simultaneously. The local stream is read out indipendently from the rest of ATLAS. During global runs, when all ATLAS subdetectors are running together, the purpose of the local stream is to provide fast online feedback regarding the status of LUCID. A set of checks are performed using local data stream in order to assess the detector health and to determine whether or not the data recorded is meaningful. This process is called *data quality monitoring*. The readout time associated with the local stream is much longer than 25 ns (the time between the bunch crossings) with a maximum recording rate of about 350 Hz. As a consequence, the local stream represents an hardware sampling of the LUCID signals. The acquisition time of the local stream is limited by VME read-out speed. The local stream is finally used for the calibration processe and for setting detector parameters as described in details in chapter 4.

The Global Stream

The discriminated signals from the CFDs are sent to a custom electronic board called LUMAT, *LUMinosity And Trigger monitoring card*, that performs three main functions:

- it sends the LUCID event to ATLAS DAQ stream;
- it implements various hit and event counting algorithms;
- it provides a fast trigger.

The output of the LUMAT card provides the so-called *global stream data* generated upon request of the ATLAS LV1 trigger as described in chapter 1. The global stream, which contains the data sent to ATLAS events, is collected via a fast optical link. For every bunch crossing, at a rate of 40 MHz, a signal is sent to the *Central Trigger Processor (CTP)*, telling it whether or not LUCID registered a hit. The CTP sends back a trigger decision based on this information together with similar signals from other subdetectors. If the event is accepted, which happens at a rate of maximum 75 kHz, LUMAT sends the hit map to the main ATLAS data flow.

A picture of the LUMAT card with its main building blocks is visible in figure 3.10. It is a 9U VME board with five piggy back boards mounted on top of it and is equipped with four fast FPGAs. The card contains in total 4 internal sets of scalers

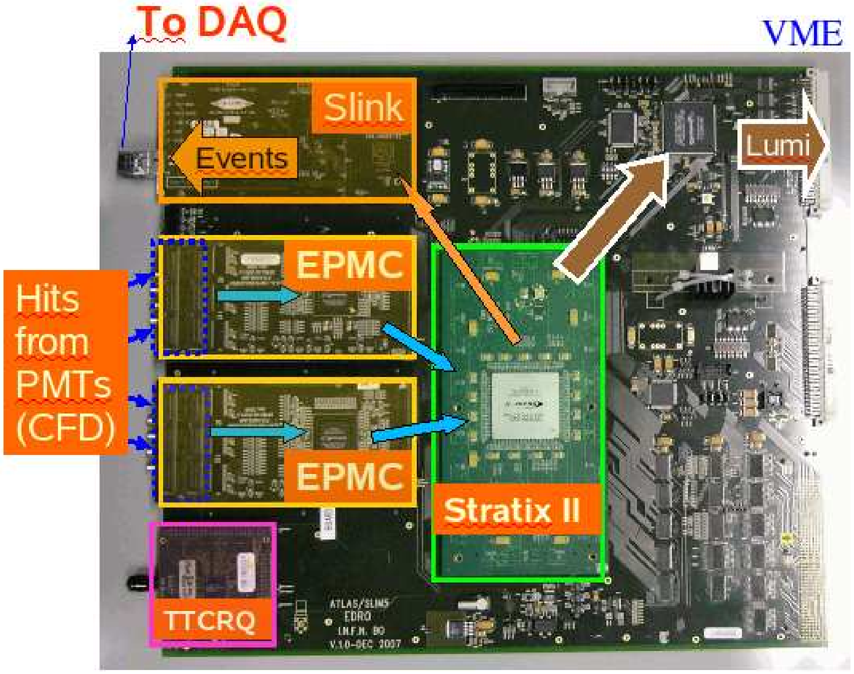

Figure 3.10: The LUMAT board with its main building block an data path.

that correspond to different ways of measuring the relative luminosity. Each set has 3564 scalers, one for each BCID. The LUMAT card samples the logical signals sent by the CFDs every 25 ns. Depending on the level of the input signals, the LUMAT card buids an hit map. The input signals must be aligned with the LHC clock so as to make each hit fall within a 25 ns time window or BCID. If a signal crosses two successive BCID windows, the LUMAT counts double and the luminosity is incorrectly evaluated. The actual readout of the scalers is not done until the end of one luminosity block. Hits are counted separately for the two LUCID modules and an information of how many hits have been observed in module A (N_A) and in module C (N_C) is available every 25 ns. A trigger information can be generated among the following logic combination: a) $N_A \geq N_{min}$, b) $N_C \geq N_{min}$, c) N_A OR $N_C \geq N_{min}$, d) $N_A \geq N_{min}$ AND $N_C \geq N_{min}$, where N_{min} is a programmable threshold value. The trigger information is generated in less than 100 ns for a total latency less than 400 ns. The counting methods based on the record of these information are described in chapter 5.

3.4 Radiation Hardness Tests on PMTs

The advantages of the direct coupling between the Cherenkov tube and the PMTs are that the light is readout directly where it is produced, without transmission steps that might introduces inefficiencies. Moreover, the quartz window of the PMTs constitutes an additional Cherenkov radiator that increases the overall signal. However, there are also drawbacks, for example active and metallic elements have to be placed in a high radiation environment. The radiation hardness of the PMTs was studied with fluxes of gamma and neutrons. Both lifetime and performance degradations were evaluated as a function of the absorbed dose.

3.4.1 Expected Dose

LUCID was proposed to the ATLAS community when ATLAS was in an advanced state of commissioning. LUCID was suggested as a possible solution to the problem of measuring the luminosity with a precision better than 5%. In designing LUCID, the available place around the ATLAS region and the corresponding quantity of radiation doses had to be taken into account. The only available space in the forward region, near the beam pipe and the interaction point where the acceptance for single interactions is maximized, was, in fact, a high radiation area. The expected radiation dose was thus evaluated and the electronics to be used were chosen accordingly.
During the first years of LHC the maximum luminosity will be $L = 10^{33} cm^{-2} s^{-1}$. The expected dose during this phase in the region of LUCID is 0.7 Mrad/y with a neutron flux of about $5 \cdot 10^{13} cm^{-2} yr^{-1}$ [24], as shown in figure 3.11. In the following years at higher luminosity the expected dose rises by a factor of 10.

3.4.2 Radiation Hardness Tests on PMTs

Taking into account the total expected radiation doses at the LUCID region, two PMTs were submitted to gamma and neutron irradiation. Both for gamma and for neutron irradiation, the total dose absorbed by the PMTs is several times larger than the one expected during the first years of LHC data taking. The PMTs were submitted to the fluxes of radiation once turned off.

For both tests, a significant increase of the dark current was measured. The increase of dark current is due to the decay of metallic materials in the PMT, such the aluminum, with a decay time of 12 min. No main effects were observed on gain, quantum efficiency as well as spectral response, within the sensibility of the measurement. The principal quantities studied for the radiation hardness tests be-

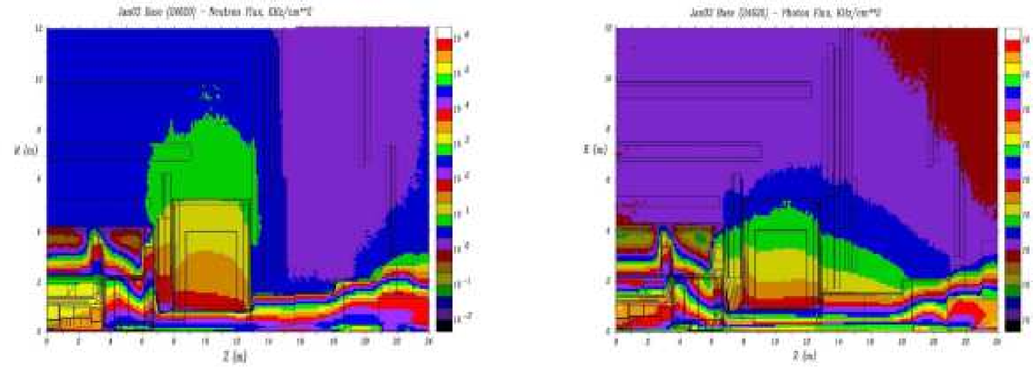

Figure 3.11: Total neutron (left) and photon (right) flux simulation in a full ATLAS quadrant at LHC design luminosity $L = 10^{33} cm^{-2} s^{-1}$. LUCID is placed at $17m < Z < 18.5m$, $|R| < 15cm$.

Figure 3.12: Two PMTs. The one in the upper part is a not-irradiated reference PMT. The one in the bottom part has been irradiated with gamma dose. The most striking change is the visible darkening of the glass part of the PMT. The quartz part kept its initial transparency.

fore and after the irradiation were listed in table 3.3.

Gamma irradiation	**20 MRad**	
	Before	*After 7 days*
Dark current at 1 kV	0.2 nA	130 nA
Gain exponent	7.12 ± 0.10	7.15 ± 0.10
Spectral response change	0% (ref)	± 2%

Table 3.2: Changes in the PMT parameters after irradiation with 20 MRad of gamma total dose. Within the sensitivity of the measurements, no changes have been observed on gain and spectral response, while an increase is the dark current is measured.

Neutron irradiation	**5 x 10 ^{1}4 n/cm^2**	
	Before	*After 2 days*
Dark current at 1 kV	0.1 nA	350 nA
Gain exponent	6.34 ± 0.29	6.64 ± 0.29
Spectral response change	0% (ref)	± 8%

Table 3.3: Changes in the PMT parameters after irradiation with neutron flux of $5 \times 10^{14} n/cm^2$. Within the sensitivity of the measurements, no changes have been observed on gain and spectral response, while an increase is the dark current is measured

According to these results and to the expected radiation doses during the first years of LHC running, the LUCID PMTs are expected to survive in such a high radiation environment without damages. On the other hand, the lifetime of the PMTs strongly depends on the gain and the total integrated charge they accumulate during their functionning. It is most plausible that the PMTs will undergo mechanical degradation, as the luminosity rise up, expecially due to the deterioration of the last dynode, which has to collect the majority of the charge.

3.5 LUCID Beam Tests

To characterize the response of LUCID, several beam tests have been done over years. The last one was done in July 2009 at the SPS-H6 beam line using pions of 120 GeV energy. During 15 days of data taking, a statistics of 80 Mevents was acquired with different tube gas-pressure configurations. The DAQ system, fully ATLAS compliant, ran at an average of 1.5 kEvents/s. The results of this beam test can be used to evaluate systematics due to variations in the gas pressure and to angular orientation of the incident particles with respect to the tube axis.

3.5.1 Experimental Setup

The setup consisted of a vessel containing seven tubes, a beam telescope and three scintillators for triggering purposes. The position of the different components is shown in figure 3.13 and 3.14. The former is a schematic representation of the setup, the latter is a photo for a more realistic view.

The beam telescope was composed of four tracking stations that had been used in the SLIM5 experiment [27], [28]. Each station was composed of a single silicon layer equipped on both side with 50 μm pitch microstrips, for x and y readout, and

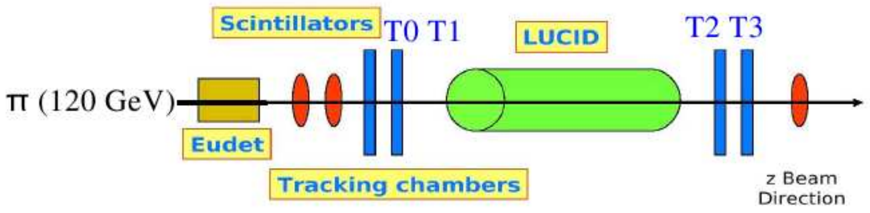

Figure 3.13: Pictorial view of the relative position of the LUCID vessel and of the trigger elements used for the beam test of July 2009.

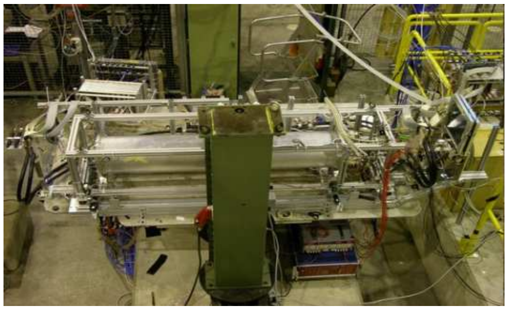

Figure 3.14: Photo of the relative position of the LUCID vessel and of the trigger elements used for the beam test of July 2009.

had a resolution on track impact point of 15 μm. The readout of the signals from the PMTs was the same as the one installed in ATLAS. The trigger was achieved requiring the coincidence of two scintillators.

3.5.2 Signal study

The mechanical instrumentation of the vassel permitted to center each tube one at a time along the beam axis. Thanks to the tracking stations, it was possible to center the beam in the quartz window of the PMT under study with a precision of 10 μm. This precise aligment of the whole system permits to evaluate separately the contribution from the quartz window and from gas avoiding the contamination of secondary particles.
Typical spectra of the charge distributions are presented in figure 3.15. The left plot shows the spectrum obtained when in the tube under study there was no gas: the peak at about 750 QDC counts is due to Cherenkov emission of pions in the quartz window. The right plot in figure 3.15 represents the charge distribution in case the tube was filled with C_4F_{10} at a pressure of 1 bar. In this case the peak moves to about 1050 QDC counts: the contribution of the Cherenkov emission from the quartz window sums up with the contribution from the gas.

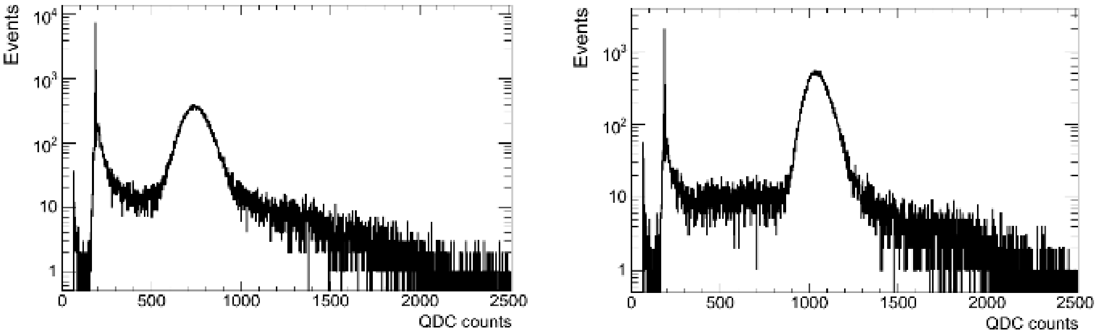

Figure 3.15: Left: charge distribution from QDC module in condition of no gas inside the tube under study. The peak at about 750 QDC counts is due to Cherenkov emission of pions in the PMT quartz window. Right: charge distribution from QDC module in case of tube filled with C_4F_{10} at 1 bar. The peak at about 1050 QDC counts is due to Cherenkov emission of pions in both the PMT quartz window and the gas. The two contributions sum up as expected.

3.5.3 Track Counting

A typical spectrum of charge distribution for one of the tubes is shown in the left plot of figure 3.16. The spectrum refers to a tube filled with C_4F_{10} gas at 1800 mbar. In the blue histogram, it is possible to see a pedestal around 190 QDC channels and a peak around 1150 QDC channel that corresponds to a track. Since the area of the scintillator is larger than the area of the PMTs, the pedestal in the charge distribution is due to particles that fire the scintillators in the outer parts of their area but do not struck the PMT surface. The red line represents the same distribution after a request on the tracking system of a clearly identified track entering into the tube: the request of a track strongly reduces the background.
The right plot of figure 3.16 refers to a different tube filled with C_4F_{10} kept at a pressure of 1100 mbar when the beam intensity was increased. In this case two peaks are visible, one at 460 QDC channels and another at 760 QDC channels. The first peak corresponds to a single track, the second to two tracks entering the tube. As can be seen by the distributions, the charge analysis can provide the number of particles hitting the detector.

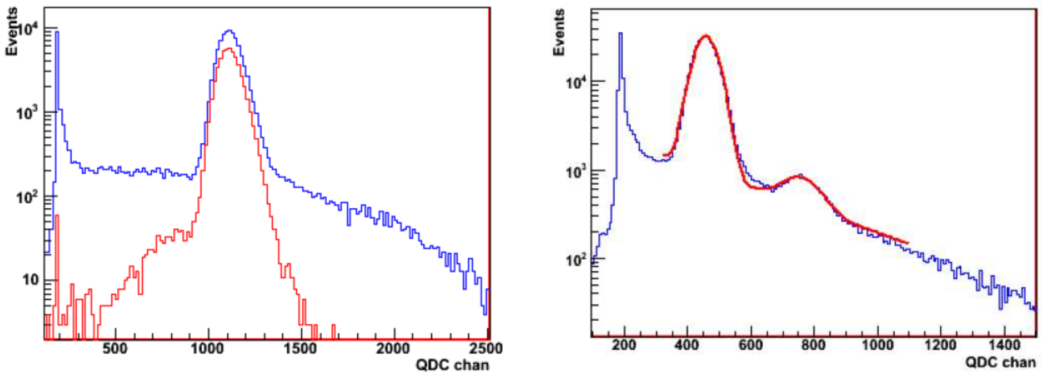

Figure 3.16: Left: charge distribution for typical LUCID tube filled with C_4F_{10} at 1800 mbar. Blue: without any request on tracks. Red: with request of one track in the triggering system. Right: charge distribution for typical LUCID tube filled with C_4F_{10} at 1100 mbar for beam of increased intensity. Two peaks are well visible, that correspond to one and two tracks entering into the LUCID tube. Red: fit on the two peaks.

3.5.4 Pressure Scan

As described in section 3.3, a change in the gas pressure results in a change of the refractive index of the gas itself and, as a consequence, a change of the Cherenkov angle and of the total number of produced Cherenkov photons. Changing the pressure of the C_4F_{10} from 180 to 1800 mbar, the average number of reflections on the tube walls passes from one to five. The average charge in a tube as a function of the gas pressure for three different gas is reported in figure 3.17: in

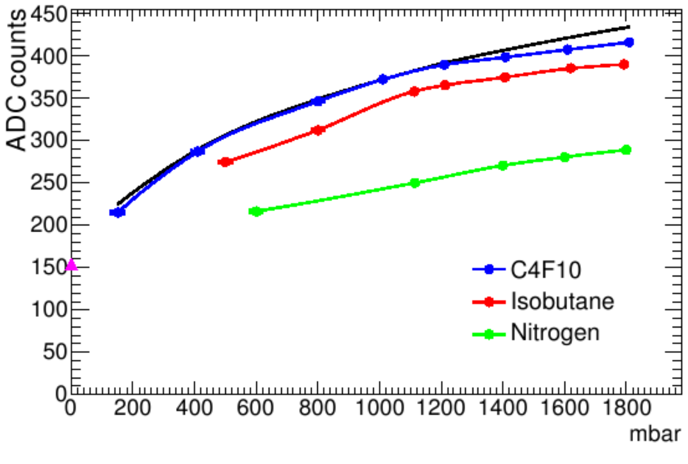

Figure 3.17: Average QDC charge for C_4F_{10} (blue), Isobutane (red) and Nitrogen (green) as a function of gas pressure. Black line represents the Monte Carlo simulation for C_4F_{10}.

blue for C_4F_{10}, in red for Isobutane and in green for Nitrogen. The purple point is an extrapolation of the case of tube without gas, which represents the contribution of quartz window only. The black line is the Monte Carlo simulation obtained for C_4F_{10}. The optical properties of the aluminum walls are enhanced by successive reflections, leading to a loss of proportionality between pressure and charge, visible from the trending of data in figure 3.17. For the same gas pressure, the C_4F_{10} is the most performant radiator gas.
The good agreement between the Monte Carlo predictions and the real data confirms that the physics that describes the LUCID functionning is well understood.

3.5.5 Angular Scan

To verify the validity of the pointing geometry of LUCID, angular scans have been performed during the beam test.
The collected charge when a charged particle enters one of the LUCID tube filled with C_4F_{10} at a pressure of 1800 mbar as a function of the angular shift between the particle trajectory and the tube axis is shown in figure 3.18. As visible from the plot, for shifts of few mrad, corresponding to a shift of the tube axis of about 20 mm, a drop in the charge of 10% arises. This behaviour guarantees the strong suppression of the background.

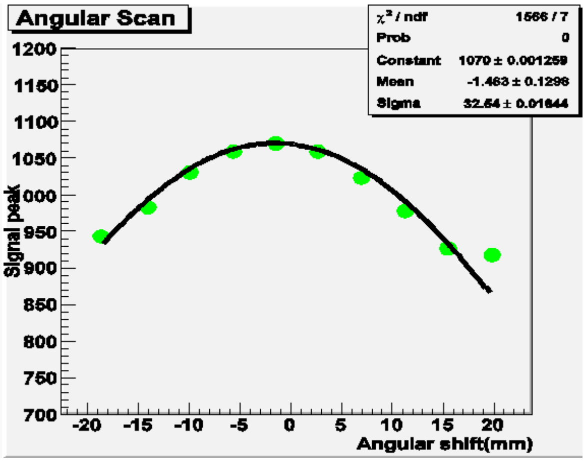

Figure 3.18: Average QDC charge for C_4F_{10} at a pressure of 1800 mbar for different angular shifts between the trajectory of an incoming particle and the LUCID tube axis.

3.6 Conclusions

The peculiar characteristics of the electronics, as for example the signal duration shorter than 25 ns, make LUCID ideal to measure the number of interactions per LHC bunch crossing, providing also an efficient trigger to the ATLAS experiment. A dedicated electronics board (LUMAT card) performs the on-the-fly evaluation of the instantaneous luminosity according to different algorithms (see chapter 5). If a calibration constant is provided, LUCID contributes also to the measurement of the absolute luminosity, with precision that depends on calibration method. On-beam tests confirmed the projective geometry of LUCID, that permits to reduce the background coming from beam-halo or beam-gas.

Chapter 4

Analysis of the LUCID Local Stream Data

4.1 Introduction

The local stream plays an important role in assessing the detector stability. Each event of the local stream is composed by the 32 charges measured by the QDC and 32 vectors containing the signals sampled by the FADC. Combining these data, a lot of cross checks can be made to determine whether or not the measurement of the luminosity is robust. Moreover, the local stream allows the determination of the optimal values of the parameters of the detector: determining the linearity range of the amplification chain, calibrating the PMTs, equalizing the photomultiplier gains as well as finding the optimal CFD thresholds and many other aspects. Finally, some performance checks on LUCID are possible, as described in next sections.

4.2 QDC Calibration for Single Photoelectron Spectra

The QDC needs to be calibrated to define the exact relation between QDC counts and number of photoelectrons. This procedure is necessary to compare the real data to the predictions of the physics of the Cherenkov process which is expressed in number of photoelectrons. A typical calibration spectrum obtained during a calibration run is shown in figure 4.1.

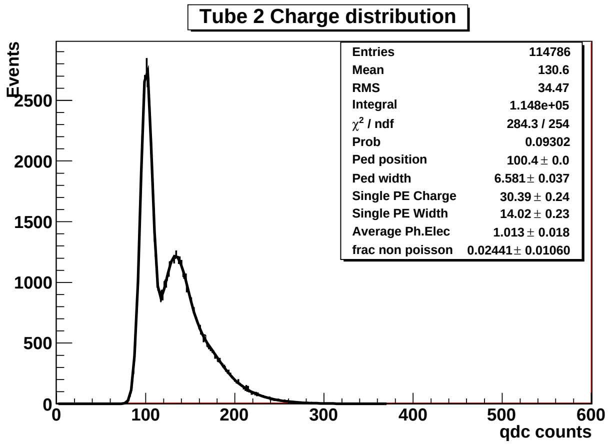

Figure 4.1: Typical calibration spectrum of single photoelectron emission from the PMT photocathode for a tube.

4.2.1 Fitting the Distribution

A first method to obtain the calibration constant consists in fitting the single photoelectron spectrum [29]. The spectrum of the charge from QDC integration shows the typical distribution of figure 4.2.b.

The first step in the calibration process is to find the pedestal (figure 4.2-a), which is the charge distribution obtained when no light is incident on PMT. The pedestal is due to the intrinsic noise of the electronics, mainly caused by the amplificator modules.

When the LEDs are turned on, the light incident on the PMT excites electrons from the photocathode via the photoelectron effect. The number of incident photons is a Poisson distributed variable and the excitation and collection of each photoelectron can be considered a binary process. The distribution of photoelectrons is thus given by:

$$P(n,\mu) = \frac{\mu^n \cdot e^{-\mu}}{n!} \tag{4.1}$$

where $P(n,\mu)$ is the probability that n photoelectrons will be collected given an expected mean number of collected photoelectrons μ. Each collected photoelectron will then be amplified by the PMT. The charge resulting from the amplification process follows a Gaussian ditribution. The total photomultiplier output charge is thus a convolution of each n-photoelectron Gaussian distribution weighted by its occurrence Poisson probability, yelding

$$P(x) = \sum_{n=0}^{+\infty} \frac{\mu^e \cdot e^{-\mu}}{n!} * Gaussian(x,n) \tag{4.2}$$

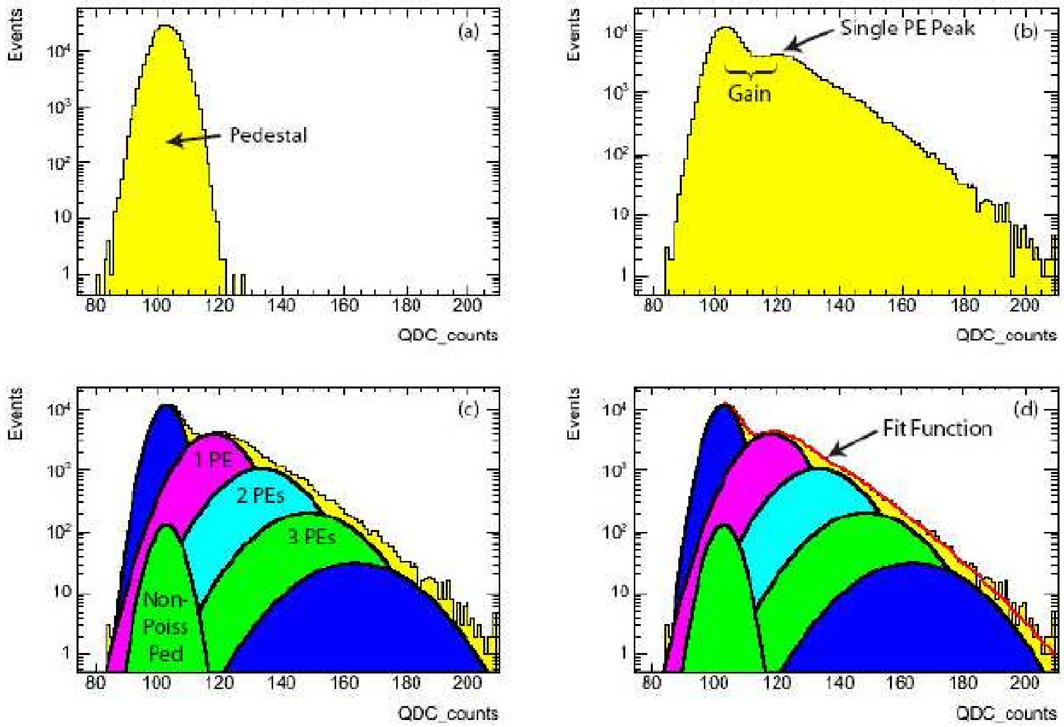

Figure 4.2: Charge distribution involved in detector calibration. The pedestal (a) is obtained in absence of light. When the mean number of photoelectron is close to unity, a single photoelectron spectrum (b) is obtanied. The sum of pedestal, single photoelectron events, double photoelectron events...(c) are combined into a fit function (d).

where $P(x)$ is the probability that the charge x is output by the PMT. If the LED intensity is turned to generate one photoelectron on average and the number of events is large, a single photoelectron spectrum (figure 4.2-b) is obtained. Figure 4.2-c shows more clearly that the total charge distribution is the sum of the contributions from single photoelectron events, double photoelectron events and so on. There is also a small contribution designated "Non-Poiss Ped", which corresponds to the pedestal events that could not be explained by Poisson statistics: the "Non-Poiss Ped" events correspond to inefficiencies of the method of detection. The conversion from QDC counts to charge is obtained by calculating the distance between the pedestal and the single photoelectron peak.

The accuracy of this calibrating algorithm is determined by how well the fit function follows the shape of the charge distribution. The method chosen to estimate the accuracy is the evaluation of the chi square parameter: the ratio between the chi square and the number of degrees of freedom must be near to one to have an accurate fit. If the gain is too low, so that the single photoelectron peak is not well resolved from the pedestal, the fitting algorithm tends to understimate the single photoelectron position. A minimum gain is thus required to separate the single photoelectron from the pedestal by at least three sigma of the pedestal. In this case, in fact, the calibration of the detector can be determined accurately.

4.2.2 Mean and RMS

Another method has been studied to calibrate the QDC signal which does not need any fit. This method is based on the principle of functioning of the electronics that characterizes a photomultiplier.
LUCID photomultipliers, model Hamamatsu R762, have ten dynodes each with a different resistance and different applied voltage as visible in figure 4.3.

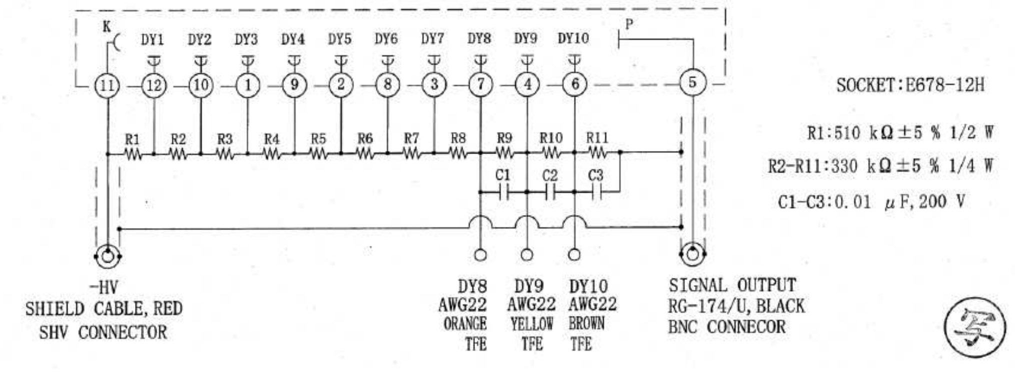

Figure 4.3: Voltage repartition for photomultiplier Hamamatsu R762 installed in LUCID.

Full details about the calculation of the calibration constant are described in Appendix C, only the relevant quantities are reported here.
The relation connecting the PMT gain to its applied voltage is:

$$G = K \cdot V^{\alpha} \tag{4.3}$$

where $\alpha = 7$ for R762 PMTs and K is a constant. We define γ as the ratio between the first and the second dynode gain. In general:

$$\gamma = \frac{k_1}{k_2} = \left(\frac{R_1}{R_2}\right)^{\alpha/no.dynodes} \tag{4.4}$$

where $R_{1(2)}$ are the resistence of the first and second dynode. For LUCID:

$$\gamma = \left(\frac{510}{330}\right)^{7/10} = 1.356 \tag{4.5}$$

The noise factor f is defined in Appendix C and can be written as:

$$f = \frac{1+\gamma(k_i - 1)}{\gamma(k_i - 1)} = 1.258 \pm 0.023 \tag{4.6}$$

The calibration constant becomes:

$$K_{cal} = \frac{1}{f} \cdot \frac{\sigma^2_{N_a}}{N_a} \tag{4.7}$$

where N_a is the amplitude of the PMT signal and σ_{N_a} is the width.
Let's see in practice how this method works. Once a calibration run is performed, the RMSs and the means of both the pedestal charge distribution and the single photoelectrum spectrum are recorded. The relation to be used to find the calibration constant becomes:

$$K_{cal} = \frac{1}{f} \cdot \frac{hRMS^2 - pRMS^2}{hMean - pMean} \tag{4.8}$$

where h stands for the single photoelectron spectrum and p for pedestal charge distribution.
The calibration constants obtained with this method have been compared with the ones obtained fitting the single photoelectron spectrum. The results for each tube for a typical calibration run are reported in table 4.1. In the last column the fractional difference between the two methods is reported. As visible from the table, the calibration constants obtained with this method differ from the ones obtained with the fit by about 1-5%. In the fit method the chi square parameter is an objective way to evaluate if the assumed shape is a good description of the spectrum. On the contrary, with the latter method, there is no objective control on the results and thus a small change in the histogram shape can change the results of the calibration. This is the reason why the fit method has been chosen as the preferred method, although the latter is much faster.

4.2.3 Photomultiplier Gain Equalization

The gain of each photomultiplier has been initially set in order to have a calibration constant of 15: 15 QDC counts correspond to a single photoelectron. This number has been chosen for two different reasons. First, as already mentioned, the peak position of the single photoelectron spectrum has to be separated from the pedestal peak by at least three sigma of the pedestal in order to guarantee a robust fit. Second, the value of the calibration constant has been set so as to exploit the whole dynamic range of the electronics, as discussed in chapter 3. During

Tube	**Calib fit**	**Calib signal**	**Diff** %
0	29.5096	28.3616	0.0389
2	30.1283	29.0567	0.0356
3	30.8113	30.5279	0.0092
4	29.5986	29.4398	0.0054
5	29.753	28.6444	0.0373
6	30.1764	28.6105	0.0519
7	29.5274	29.0421	0.0164
8	30.689	29.7914	0.0292
9	29.3896	29.5255	0.0046
10	29.7471	29.2117	0.0180
11	29.754	31.0844	0.0689
12	29.6611	29.4555	0.0069
13	29.5483	30.7522	0.0407
14	29.8143	29.7366	0.0026
15	29.5203	30.306	0.0266
20	30.3286	29.1789	0.0379
21	29.6377	30.4282	0.0267
22	29.7431	31.6236	0.0632
23	29.6076	31.5913	0.0670
24	29.5361	27.4018	0.0723
25	29.8371	32.0571	0.0744
26	30.0891	29.3174	0.0256
27	29.8023	28.4361	0.0458
28	30.5193	28.6602	0.0609
29	30.177	29.6863	0.0163
30	30.0054	29.1859	0.0273
31	30.0759	32.0471	0.0655
32	30.1865	28.6344	0.0514
33	29.9291	30.2425	0.0105
34	29.5942	28.6277	0.0327

Table 4.1: The values of the calibration constants obtained with the two different methods are reported for each tube. In the last column the percentage difference of the two results is listed. No results are reported for tube 1 and 35 because they correspond to broken PMTs.

calibration runs, in which the expected signals are much smaller than in physics runs, an additional amplification of factor 2 is applied on the incoming signals. The calibration constant becomes 30 as visible in the fit values of figure 4.1.

Since the PMTs are not identical, they require different values of the applied voltage to obtain the same gain. Let's remind that, in fact, the relation between the applied voltage and the gain of a PMT is $G = K \cdot V^{\alpha}$. The gain curve used to evaluated the needed voltage is obtained by measuring the gain at different voltages. The values of K and α are found by fitting the data points with an exponential. Once they are known, the appropriate voltage for any gain can be exctracted. The gain curve for tube 33 is presented in figure 4.4: in this case to have a calibration of 15 QDC counts in a physics run, an applied voltage of 928 V is required. Table 4.2 reports the final voltage obtained with the above mentioned procedure for each tube.

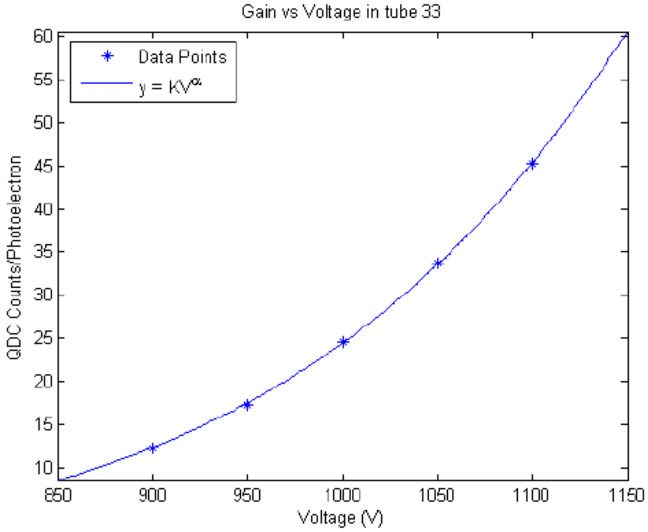

Figure 4.4: PMT gain as a function of voltage for tube 33.

Initially, a gain curve is used to find the optimal voltages to be applied to the PMTs. Once this procedure has been done and a first estimate of the value of the PMT voltages has been found, almost every day a calibration run is performed. According to the calibration results, a fine tuning of the PMT voltages is done to ensure that the calibration constant of each PMT is in the range of 30.0 ± 0.5, in a calibration run. PMT gain can, in fact, change with temperature or can undergo spontaneous drifts in time, so a day-by-day adjustment is mandatory for a precise equalization. Thanks to the characteristics of ATLAS Data Acquisition System, an automatic routine has been implemented in the DCS framework to tune the PMT voltages at each calibration run, if necessary.

Side A	
Tube	**Voltage (V)**
0	873
2	873
3	817
4	868
5	873
6	885
7	812
8	799
9	811
10	848
11	804
12	790
13	781
14	807
15	818

Side C	
Tube	**Voltage (V)**
20	878
21	852
22	897
23	868
24	870
25	863
26	905
27	872
28	819
29	857
30	860
31	799
32	885
33	924
34	889

Table 4.2: Voltages that best equalize the PMT gain at 15 QDC counts per photoelectron in a first approximation obtained from gain curves. No results are reported for tube 1 and 35 because they correspond to broken PMTs.

4.3 Comparison between Monte Carlo and Data

Monte Carlo simulations have been carried out in order to predict the response of the detector to inelastic *pp* interactions. All the data obtained by Monte Carlo expectations are expressed in number of photoelectrons, since Monte Carlo simulates the physics of the Cherenkov effect that produces photoelectrons as a final result. Monte Carlo data are compared with the charge distribution obtained from the QDC. The charge collected by the PMTs can be evaluated also from the signal sampling provided by the FADC. This has been done and the results have been compared to the ones obtained by the QDC. The agreement of the two measurements are good. The final decision has been to use only the charge from the QDC while the separation in time between two bunches is smaller than the QDC gate.

4.3.1 LUCID Simulation

The LUCID simulation is divided into three steps. The first step is the description of the geometry of the detector in a stand-alone GEANT4 simulation. The second step is the study of the detector response to particles of a given energy,

position and direction. Finally, inelastic *pp* collisions at the center-of-mass energy of 7 TeV are generated to simulate the production and decay of particles according to the current knowledge of cross sections and branching ratios.
In the first step of the simulation, the main detector elements (vessel, radiator gas, tubes, quartz window of PMTs) have been described in a stand-alone GEANT4 simulation (version 4.7.1p01) [30]. PMTs are simulated with a thin quartz disc matching the transverse dimensions of the tubes. The simulation of the PMT window is crucial since it acts as photon emitter, in addition to the gas radiator. The dynodes inside the PMT are not simulated. The photocathode is simulated by applying the PMT quantum efficiency factor provided by Hamamatsu [31] to the number of photons produced when a particle coming from a *pp* collision enters a LUCID tube. It must be noticed that all the tubes installed in LUCID were initially simulated with the same characteristics in terms of reflectivity and dimentions, even if this was not realistic. A fine tuning of the Monte Carlo prediction is necessary to take care of the instrinsic differences from tube to tube.
The parameters used to decribe the detector geometry are listed in table 4.3.

Distance from IP [mm]	16715.5
Vessel length [mm]	1532
Vessel inner radius [mm]	85
Vessel outer radius [mm]	125.5(min), 147(max)
Vessel inner thickness [mm]	2.5
Vessel outer thickness [mm]	3.0
Vessel bulkhead thickness [mm]	3.2
Radial distance Tube-Beam [mm]	93.6 (ring 1)
Radial distance Tube-Beam [mm]	114.7 (ring 2)
Tube thickness [mm]	1.0
Tube length [mm]	1495
Tube radius [mm]	7.0
Pmt quartz window thickness [mm]	1.2
Pmt quartz window radius [mm]	7.0
Gas pressure [bar]	1.1
Gas temperature [K]	293.15

Table 4.3: Parameters used for the geometrical desciption of LUCID.

The second step is the study of the detector response to particles of a given energy, position and direction. LUCID geometry is such that a particle originating from the IP, called primary particle, produces more light than a particle coming from any other direction, called secondary particle. The response of LUCID is simulated for particles originating from the IP and travelling either along the tube axis (on-axis) or along a random direction (off-axis). The detector response to primary particles is obtained by using 180 GeV charged pions travelling exactly along the tube axis. In this case, pions emit Cherenkov light in both the gas and the PMT quartz window. The average number of expected photoelectrons is 105 [26], out of which 75 come from gas and 30 come from the quartz window, as visible in figure 4.5.

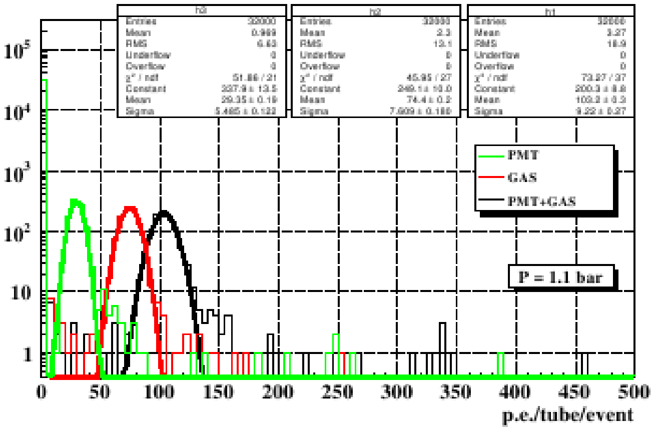

Figure 4.5: Average number of expected photoelectrons produced by Cherenkov effect when a charged pion travels along the tube axis, for a single tube, for a single *pp* interaction.

In a more realistic scenario, primary particles originated at the IP travel along directions different from the tube axis. However, since the diameter of the tube is small compared to the distance between LUCID and the IP, the angle between the trajectory of an off-axis primary particle and the tube can be considered negligible. When a primary particle crosses the detector tube walls or some other material in the ATLAS volume, secondary particles are produced by interactions with such material. Secondary particles may cross the Cherenkov radiators, both quartz window and gas, and release light which adds to the signal of primary particles. The trajectory of a secondary particle is typically at a non negligible angle with respect to the axis of the tube, thus the light emission is smaller than the one produced by a primary particle. Off-axis primary particles are simulated by shooting 180 GeV pions from the IP with a flat polar angle between 4 and 10 mrad and a flat azimutal angle between 0 and 2π. The results are presented in figure 4.6, where two quite different distributions are visible.

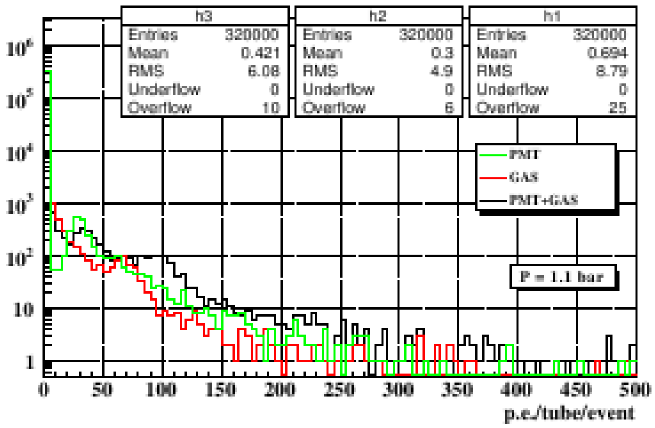

Figure 4.6: Average number of expected photoelectrons produced by Cherenkov effect, when a charged pion travels along a random trajectory inside the tube, for a single tube.

In case of off-axis particles, a continuous exponential background is created [26]. Two small peaks are visible in the same positions in which they appear in case of on-axis particles. Neutral particles do not emit Cherenkov photons when crossing the LUCID detector. However, neutral particles might affect the LUCID response by producing charged particles when interacting with the material around the LUCID volume. The spectrum of photoelectrons produced by 100 GeV photons has been studied: a peak at about 30 photolectrons is still visible, while the peak at 105 photoelectrons disappears due to the fact that secondary particles typically do not travel the full lenght of the tube. [26].

Finally, primary pp collisions at a the center-of-mass energy of 7 TeV are simulated according to the production cross sections and the decay branching ratios provided by PHOJET (version 1.12.1.35) [32]. Particles are generated by a GEANT3-GCALOR [33] simulation that describes all the ATLAS detector subsystems except LUCID, in order to describe the interaction of primary particles with the detector material up to the LUCID volume. The impact point, the arrival time and the energy of all the original primary particles and the secondary particles produced by interactions with ATLAS materials hitting the LUCID volume are seed for the track propagation inside the volume with the stand-alone GEANT4 [30] simulation of the first step. Background originated from beam halo and beam-gas interactions inside the beam pipe is not simulated.

The final expected distribution of the number of photoelectrons produced by a single pp collision for a single tube is shown in figure 4.7. The first peak at about 35 photoelectrons corresponds to particles that traverse the quatz window but only a small length inside the gas. The second peak at about 100 photoelectrons corresponds to particles that traverse both the quartz window and the tube for most of its length: the peak corresponds to the sum of photoelectrons produced in the quartz and in the gas.

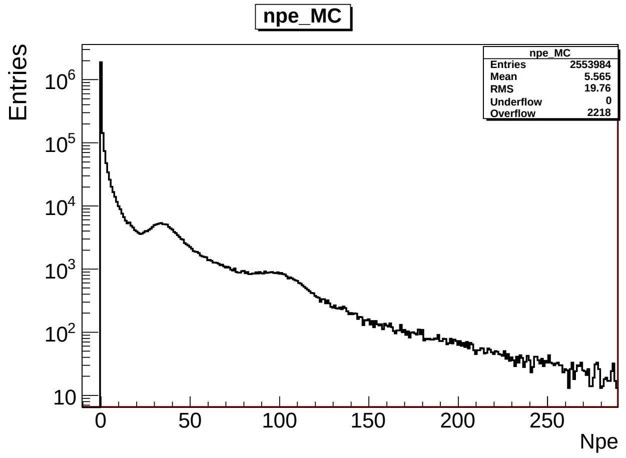

Figure 4.7: Distribution of the number of photolectrons expected from simulation of single *pp* collision for a single tube.

4.3.2 Peak Positions in Local Stream Data

It is mandatory to verify, at the very beginning of LHC data taking, if Monte Carlo predictions are in agreement with the real data: in first approximation, if the peaks expected from the simulation are present also in the data recorded by LUCID. Figure 4.8 shows the distribution of the number of photoelectrons per single *pp* event per tube predicted by Monte Carlo simulations, in dashed line, and the same distribution obtained with real data, in solid line, for tube 0.

The presence of three peaks is well visible in both plots. The peak at zero corresponds to events in which no particle traversed the tube under study. The presence of the peaks in both Monte Carlo and real data confirms that in first approximation the LUCID response has been well simulated. However, the peak positions are not the same in Monte Carlo and in real data. This aspect has been studied in details and the results are presented in section 4.3.4.
Tubes 21, 22, 23, 30, 31 and 33 in side C show no peaks at all, as visible for example in figure 4.9: there is no evidence for any peak. One of the reasons has been tracked as the presence of a residual and unexpected magnetic field.
Where possible, the peaks of the charge distribution obtained from real data have been fitted with Gaussians to model the peaks and an exponential to model the smooth part of the distribution. Mean position and RMS of the peaks are reported

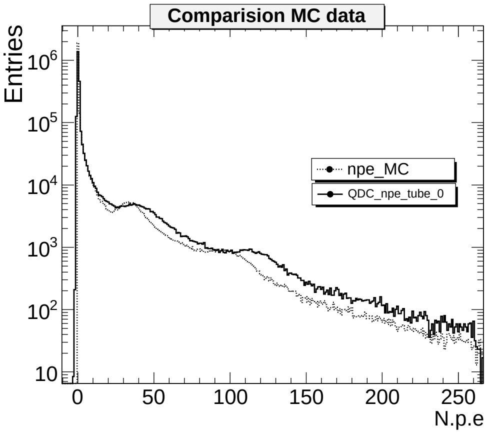

Figure 4.8: . The distribution of the number of photoelectrons per single *pp* event per tube predicted by Monte Carlo simulations, in dashed line, is compared with the same distribution obtained with real data for tube 0 in solid line. Two peaks are well visible in both distributions: the first corresponds to Cherenkov emission from a particle passing through the PMT quartz window, the second one corresponds to Cherenkov emission from a particle passing through both quartz window and gas. The two histograms are normalized to the number of entries.

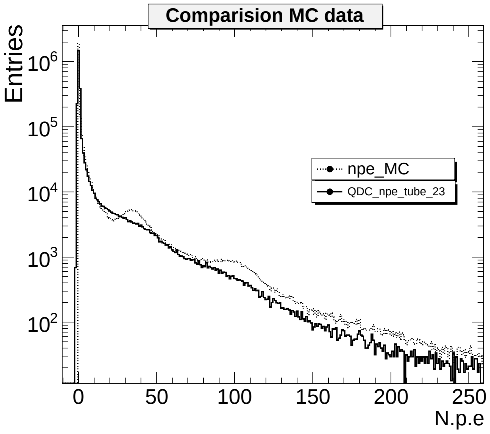

Figure 4.9: . The distribution of the number of photoelectrons per single *pp* event per tube predicted by Monte Carlo simulations, in dashed line, is compared with the same distribution obtained with real data for tube 23 of side C in solid line. The peaks in real data are not distinguishable from the smooth part of the distribution. The histograms are normalized to the number of entries.

in table 4.4 for each tube. The errors on the fitted values of positions and RMS of the peaks are about 1-3% for tubes in side A and 2-5% for tubes in side C. The widths of the peaks are in average larger for the tubes in side C than for tubes in side A due to the presence of a strongest residual magnetic field. Moreover, for tube 33 the second peak is too large to be fitted, while for tubes 23 and 30 only a rought estimation of the position of the first peak is possible.

4.3.3 Effects of Residual Magnetic Field

Evaluation of Residual Magnetic Field in the LUCID Region

Simulations [34] of the barrel and endcap toroid fields were done to estimate their magnitude in the region occupied by ATLAS. The solenoid field was expected to give no significant contributions at the distances in which the detectors are installed. Typical B-field values in the LUCID position would not be greater than 10 mG [35]. This is not enough to have any significant influence on the PMT behaviour. Actual data taken during the first phase of LUCID commissioning in 2009 indicated that this was not the case. The magnetic field around LUCID was measured with a hand probe when only the solenoid was turned on. The value of the magnetic field reaches up to 50-60 G in certain parts of the region in which LUCID is installed. The behaviour of the PMTs is known to be affected by the presence of B-field. In particular the PMTs installed in LUCID have a strong dependence on the spatial orientation of the PMT with respect to the magnetic field. In 2009 LHC was not operating yet, so only data from high intensity LED runs were available to be analyzed. It was found that the signals obained enlighting the PMTs with the LEDs were attenuated when the toroid and the solenoid were on. A decrease in the PMT gain was observed. The slope of the relation between the amplitude and the charge decreased as well.

Although the presence of the iron shield, a stray magnetic field is present in LUCID region. Two ways of evaluating the influence of residual magnetic field have been studied. The first is the effect of magnetic field on calibration data; the second is the effect on the position and on the width of the peaks obtained during physics runs.

It must be noticed that the effect of the stray magnetic field on PMT performances is not included in the Monte Carlo predictions, so fine tuning of the simulation is necessary to take into account this effect, as described in section 4.3.4.

Effect of Magnetic Field on PMT Calibration

The signal decrease due to the presence of the residual magnetic filed can be recovered by a slight adjustment of the applied voltage. To verify that the recovery is succesfull, two calibration runs, performed one in case of toroid magnetic

Tube	Mean 1st peak	RMS 1st peak	Mean 2nd peak	RMS 2nd peak
0	38.48	19.31	114.61	10.09
2	35.09	18.63	113.98	21.63
3	33.14	19.76	100.67	18.72
4	42.12	16.26	113.24	26.38
5	42.66	16.36	118.57	12.82
6	41.86	15.51	116.76	12.43
7	35.83	17.03	109.93	14.95
8	38.86	16.58	109.05	12.00
9	38.85	17.51	108.10	10.83
10	41.29	16.54	116.13	11.72
11	37.71	18.25	118.60	11.84
12	39.24	18.46	119.09	12.05
13	40.11	16.78	115.42	21.76
14	41.74	16.81	109.45	16.64
15	39.73	17.15	110.61	11.97
20	36.68	17.29	107.92	10.36
21	34.48	16.69	102.02	13.18
22	38.06	17.53	106.70	19.83
23	25.61	~20	93.85	31.04
24	40.03	16.12	118.31	20.80
25	30.95	21.78	95.10	26.79
26	30.76	20.83	93.11	20.98
27	36.87	17.79	114.37	27.04
28	39.28	17.21	117.86	20.76
29	38.90	17.13	112.21	10.15
30	31.27	~20	92.88	25.22
31	34.40	33.51	101.44	21.78
32	38.56	16.10	102.50	23.38
33	38.38	8.51	nan	nan
34	36.75	17.04	103.80	19.74

Table 4.4: Value of mean and RMS of first and second peaks from QDC distribution in number of photolectrons for all tubes. No results are reported for tube 1 and 35 because they correspond to broken PMTs.

field turned on and another with the toroid magnetic field turned off, have been compared to see the influence of the stray magnetic field on PMT performances. The fit to the single photoelectron spectrum provides the evaluation of some important parameters: the pedestal position and width, the charge and width of the single photoelectron distribution as well as the mean number of photoelectrons. The mean of the peak position gives the calibration constant that permits to pass from QDC counts to number of photoelectrons. With a wrong calibration constant the comparison between Monte Carlo and data would be incorrect. The mean number of photoelectrons is related to the efficiency of the LUCID detector: if this number decreases, the efficiency decreases. The width of the peak of single photoelectron is related to the resolution. The results of the fit for the two calibration runs are reported in figure 4.10 for tube 31, which, as described in section 4.3.2, has been demonstrated to be strongly affected by the magnetic field.

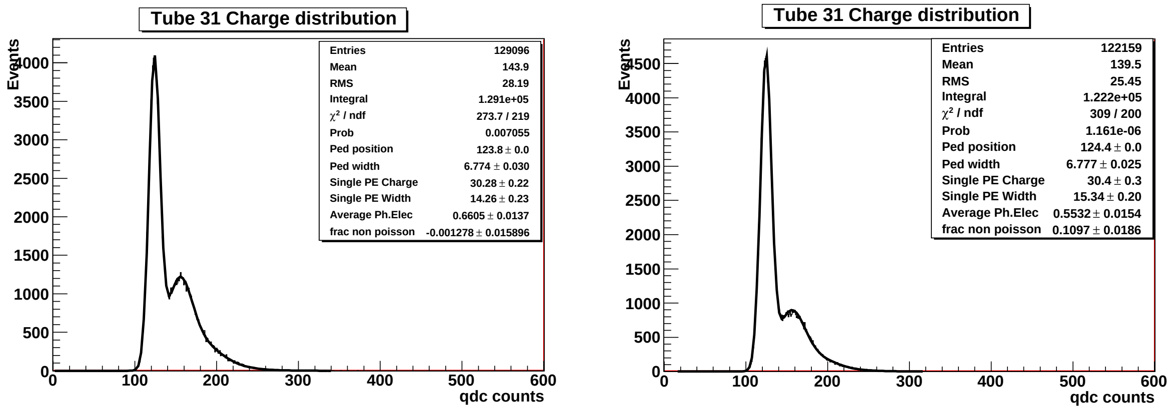

Figure 4.10: Results of fit on calibration runs with magnetic field turned off (left) and with magnetic field turned on (right) for tube 31.

The difference in the average number of photoelectrons is about 14%: from 0.6677 with toroid magnetic field turend off, to 0.5725 with toroid magnetic field turned on. The calibration constant is lower, while the width of the signal is larger in presence of magnetic field. This has an influence on the signal resolution, defined as the ratio between the width and the mean of the signal. The resolution is 0.47 when there is no magnetic field and 0.54 in presence of magnetic field: the resolution increases by about 13% when the magnetic field is turned on. A small value of resolution is important for example to resolve two or more tracks that enter the LUCID volume. To verify if these effects are present for all tubes and with the same strenght, all the calibration runs when the toroid magnetic field was turned on have been compared with all the calibration runs when the magnetic field was turned off. Since ATLAS normally runs with both solenoid and toroid fields on, only few calibration runs have been performed with the toroid field turned off. The position and the width of the single photoelectron distribution, as well as the resolution, have been evaluated for each run and tube. The average value of

the resolution over all the runs has been calculated in case of both magnetic field turned on and off. The difference between the average resolutions in case of B-field on and off has been compared with the spread of the resolutions over all the runs. If the difference between the average resolutions is larger than the spread over the runs, some systematics effects can be assumed to be due to the residual magnetic field. Table 4.5 lists the average resolutions in case of toroid field both turned off and on and the spread of the measurements over all the runs. No clear evidence of a worsening in the resolution is visible from this study. However, those tubes which in presence of magnetic field show no peaks, are also characterized by a larger signal width, a smaller average number of photoelectrons and a larger fraction of non poissonian component of pedestal in case of calibration with magnetic field on.
In conclusion, an adjustment of the applied voltages of PMTs is sufficient to recover the decrease of the gain which arise in presence of B-field.

Effect of Magnetic Field on Peak Positions

Although increasing the PMT voltages seems to be sufficient to recover the gain loss observed in presence of magnetic field, in some tubes the peaks are not distinguishable from the smooth part of the distribution in case of toroid magnetic field tuned on. Figure 4.11 shows the charge distributions in case of both toroid and solenoid on resulting from Monte Carlo predictions, in dashed line, and from real data, in solid line, for tube 0 on the left and tube 23 on the right.

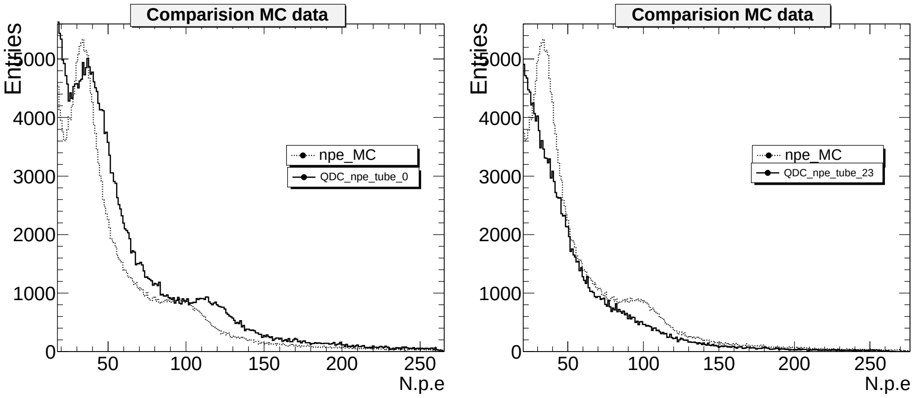

Figure 4.11: Charge distributions in case of both toroid and solenoid on resulting from Monte Carlo predictions, in dashed line, and from real data, in solid line, for tube 0 (left) and tube 23 (right): no peaks are visible for tube 23.

The demonstration that this effect is due to the residual magnetic field in the LUCID region is provided by the fact that the peaks are there when the magnetic

Tube	$\overline{Res}$ **B off**	$\overline{Res}$ **B on**	**Spread B off**	**Spread B on**	**Mean diff**
0	0.458	0.480	0.0085	0.0011	0.0224
2	0.453	0.468	0.0116	0.0013	0.0152
3	0.456	0.464	0.0063	0.0023	0.0082
4	0.458	0.480	0.0102	0.0011	0.0214
5	0.448	0.469	0.0025	0.0018	0.0209
6	0.442	0.442	0.0092	0.0005	0.0008
7	0.465	0.460	0.0068	0.0003	0.0048
8	0.455	0.451	0.0101	0.0021	0.0038
9	0.432	0.494	0.0085	0.0015	0.0617
10	0.447	0.445	0.0063	0.0015	0.0025
11	0.487	0.506	0.0038	0.0009	0.0196
12	0.480	0.481	0.0103	0.0005	0.0011
13	0.508	0.501	0.0043	0.0002	0.0069
14	0.469	0.474	0.0037	0.0007	0.0042
15	0.457	0.468	0.0084	0.0018	0.0106
20	0.469	0.452	0.0154	0.0007	0.0171
21	0.469	0.500	0.0034	0.0022	0.0302
22	0.469	0.497	0.0045	0.0002	0.0277
23	0.480	0.512	0.0067	0.0025	0.0311
24	0.465	0.469	0.0077	0.0012	0.0034
25	0.451	0.483	0.0091	0.0011	0.0322
26	0.430	0.457	0.0137	0.0021	0.0271
27	0.457	0.463	0.0029	0.0017	0.0068
28	0.462	0.469	0.0061	0.0012	0.0073
29	0.460	0.462	0.0121	0.0020	0.0014
30	0.456	0.483	0.0120	0.0001	0.0272
31	0.463	0.498	0.0082	0.0011	0.0352
32	0.445	0.442	0.0057	0.0008	0.0033
33	0.438	0.455	0.0163	0.0007	0.0166
34	0.431	0.445	0.0089	0.0016	0.0134

Table 4.5: Results of the means over all the runs of the resolutions in case of both toroid field turned off (firts column) and turned on (second column) reported for each tube. The spread of the two former measurements are reported in the third and fourth colums. The mean differences (max value - min value)/2 of the resolution are reported in the last column. No results are reported for tube 1 and 35 because they correspond to broken PMTs.

field is off, as shown in figure 4.12.

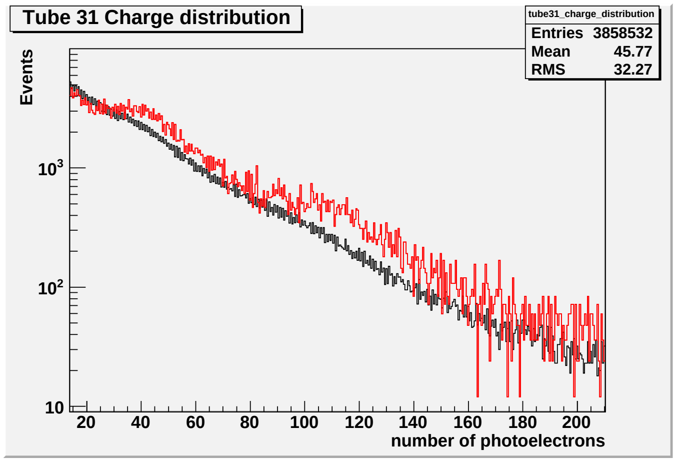

Figure 4.12: Charge distributions obtained from real data for tube 23 in case of both toroid and solenoid fields turned on (black line) and off (red line). The peaks are visible only in case of magnetic field turned off.

Effect of Magnetic Field on Hit Counting

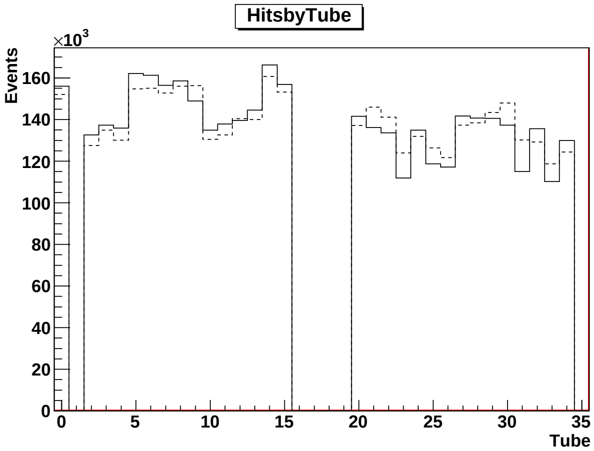

Figure 4.13: Hits by tube for a run with solenoid and toroid fields turned on (solid line) and a run with the toroid field turned off (dashed line). The two histograms are normalized to the same number of entries.

The influence of magnetic field on tubes of side C can also be observed studying the different number of hits per tube that are recorded in case of B-field both turned

on and off.
Figure 4.13 shows the number of hits per tube measured with the toroid and solenoid on, in solid line, and off, in dashed line. In absence of magnetic field the tubes in side C record a larger number of hits than in presence of magnetic field, the average number of hits in side C is more similar to the one in side A. On the contrary, side A is less affected by the residual magnetic field.

4.3.4 Monte Carlo Tuning

Two main differences are observed when comparing the charge distribution in data and Monte Carlo predictions. In some tubes the peaks are indistinguishable from the smooth part of the distribution. Moreover, in the Monte Carlo distributions, the position of the peaks is not the same observed in data and the widths of the peaks are smaller.
A fine tuning of the Monte Carlo predictions is necessary to restore the agreement. Two effects, in particular, were not simulated and could affect the Monte Carlo predictions. First, all the PMTs and the tubes were simulated with the same features. This is not realistic since the tubes have different characteristics of reflection, mechanical dimentions and polish. Second, the effect of the residual magnetic field is not simulated at all.
The tuning is performed in several steps. The first step is to find the scale factors that have to be applied to the simulated data in order to obtain the same number of photoelectrons, as found in the data, both for the quartz window and the gas. A run without gas inside LUCID has been performed to evaluate the factor to be applied to the first peak position. In case of no gas, in fact, the relation between the number of simulated and recorded photoelectrons is:

$$n_{quartz}^{MC} \cdot f_{quartz}^{MC} = n_{quartz}^{data} \tag{4.9}$$

where n_{quartz}^{MC} and n_{quartz}^{data} are the mean value of the peak obtained by fitting the charge distribution with a Gaussian in Monte Carlo and data respectively and f_{quartz}^{MC} is the scale factor. Once the scale factor for the quartz window charge distribution has been found, the scale factor to be applied to the gas contribution is evaluated from the relation:

$$n_{quartz}^{MC} \cdot f_{quartz}^{MC} + n_{gas}^{MC} \cdot f_{gas}^{MC} = n_{quartz}^{data} + n_{gas}^{data} \tag{4.10}$$

where f_{quartz}^{MC} is the scale factor for the quartz contribution, f_{gas}^{MC} is the scale factor for the gas contribution, n_{gas}^{MC} and n_{gas}^{data} correspond to the positions of the second peak in simulated and real data respectively. For real data the positions of the peaks have been evaluated mediating the results of fits to all the runs taken during the 2010 LHC running. Table 4.6 lists the values of the scale factors to be applied

Side A		
Tube	f^{MC}_{quartz}	f^{MC}_{gas}
0	1.010	1.176
2	0.991	1.217
3	0.948	1.108
4	1.152	1.143
5	1.221	1.105
6	1.160	1.103
7	0.988	1.144
8	1.092	1.075
9	1.063	1.069
10	1.143	1.100
11	1.091	1.208
12	1.109	1.212
13	1.117	1.125
14	1.185	1.026
15	1.142	1.037

Side C		
Tube	f^{MC}_{quartz}	f^{MC}_{gas}
20	1.023	1.064
21	1.127	0.956
22	1.043	0.975
23	0.986	0.938
24	1.148	1.205
25	0.899	1.095
26	0.898	1.137
27	1.098	1.222
28	1.115	1.262
29	1.109	1.160
30	1.127	0.923
31	1.043	0.969
32	1.085	1.132
33	1.043	0.969
34	1.063	1.174

Table 4.6: Scale factors to be applied to the number of photoelectrons expected by the Monte Carlo predictions for both quartz and gas plus quartz contribution in order to tune the positions of the peaks of real data. No results are reported for tube 1 and 35 because they correspond to broken PMTs.

to both first and second peak position for each tube.

The second step is smearing the Monte Carlo data in order to reproduce the resolution found in the data. A smearing to the expected number of photoelectrons from the quartz window is sufficient to adjust also the width of the second peak. The smearing factor has been evaluated so that the resolutions of the peaks in simulated and real data agree. The factors applied to the Monte Carlo data for each tube are listed in table 4.7.

Figure 4.14 shows the charge distributions obtained from real data (solid line) and Monte Carlo predictions after the application of the scale and smearing factors (dashed line) for tube 0 on the left and tube 23 on the right. The agreement is satisfactory.

The smearing factor applied to the number of photoelectrons expected from the quartz window results in a suppression of the peaks which can well simulate the inefficiency of those tubes that are most affected by the residual magnetic field.

Side A	
Tube	**Smearing**
0	0.318
2	0.292
3	0.316
4	0.208
5	0.179
6	0.204
7	0.281
8	0.233
9	0.261
10	0.223
11	0.250
12	0.254
13	0.239
14	0.202
15	0.224

Side C	
Tube	**Smearing**
20	0.268
21	0.277
22	0.297
23	0.310
24	0.203
25	0.347
26	0.269
27	0.241
28	0.234
29	0.234
30	0.277
31	0.297
32	0.225
33	0.297
34	0.238

Table 4.7: Results of the smearing factors to be applied to the number of photoelectrons from quartz peak predicted by Monte Carlo simulation in order to reproduce the resolution of both quartz and gas peak in real data. No results are reported for tube 1 and 35 because they correspond to broken PMTs.

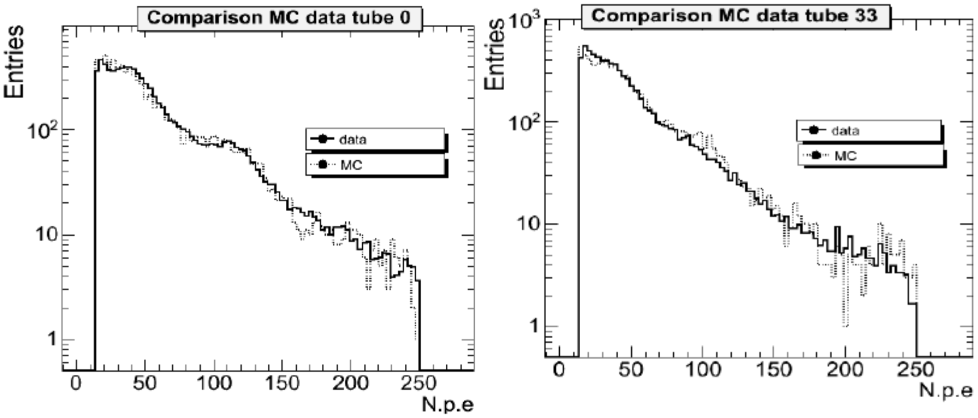

Figure 4.14: Charge distributions obtained from real data (solid line) and Monte Carlo predictions after the application of the scale and smearing factors (dashed line) for tube 0 (left) and tube 33 (right).

Efficiency

An event in the LUCID detector corresponds to a bunch crossing with at least one signal from a PMT above threshold, called a hit. An event can be selected in single side more or in coincidence mode.In single side mode, at least one hit must be detected in any of the two LUCID modules, while in coincidence mode at least one hit must be detected in each of the two modules.
The efficiency of the Monte Carlo predictions has been evaluated performing the ratio between the number of events recorded according to the LUCID threshold, in both single side and coincidence mode, and the total number of events generated by the Monte Carlo simulations, which are aware of the LUCID threshold. The efficiencies for both single side mode and coincidence mode are reported in table 4.8 before and after the corrections on the Monte Carlo predictions. The efficiencies for the corrected Monte Carlo do not significantly differ from those obtained for the uncorrected one.

MC	**Event AND**	**Event OR**
Uncorrected	23.30%	66.04%
Corrected	23.64%	66.51%

Table 4.8: Efficiencies of Monte Carlo predictions for both single side and coincidence event selection before and after the corrections.

Hit Multiplicity

The effects of the Monte Carlo adjustment are studied also on the dependency of the hit multiplicity on the mean number of interactions per bunch crossing (μ). How μ can be evaluated will be described in chapter 5. Figure 4.15 shows the dependency of the hit multiplicity on the mean number of interactions per bunch crossing (mu) in real data (black boxes) and in the Monte Carlo predictions before (green points) and after (red points) the application of the scale and smearing factors: a better agreement is reached with the corrected Monte Carlo. To quantify the improvement obtained with the corrected Monte Carlo, the dependency of the fractional ratio $(Mult^{data} - Mult^{MC})/Mult^{data}$ on the mean number of interactions per bunch crossing has been evaluated. As visible from figure 4.16, before the corrections the difference between Monte Carlo and data is about 10-11%, while it decreases to about 3-4% after the corrections. As a general comment, it must be noticed that the multiplicity calculated from data is smaller than the one predicted by Monte Carlo simulation, even including the afore mentioned corrections. This means that some other effects must be included in the Monte Carlo simulation.

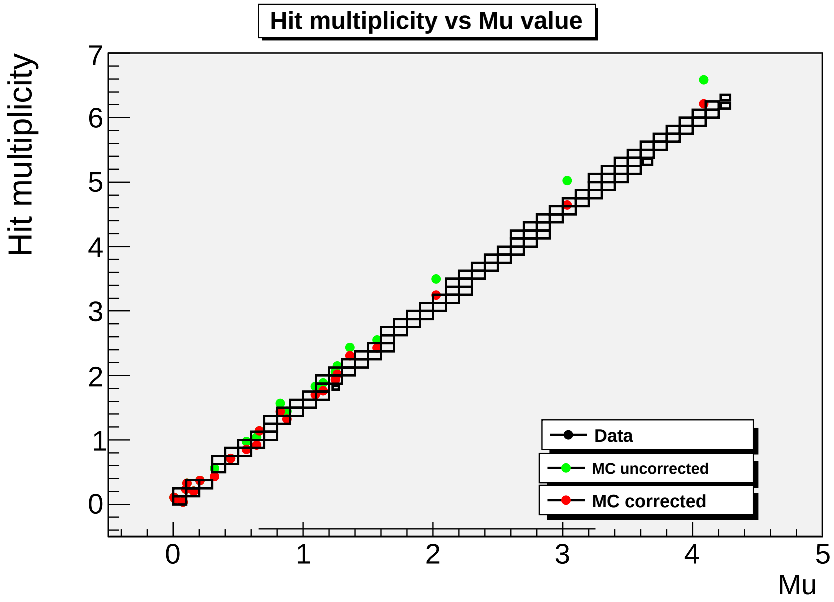

Figure 4.15: Dependency of the hit multiplicity on the mean number of interactions per bunch crossing (mu) in real data (black boxes) and Monte Carlo predictions before (green points) and after (red points) the Monte Carlo adjustment.

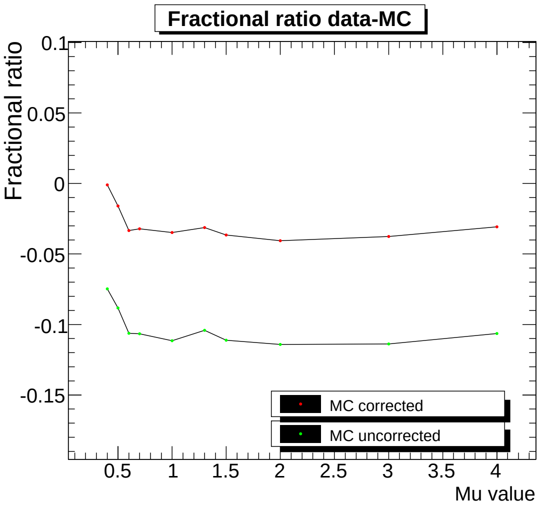

Figure 4.16: Fractional ratio $(Mult^{data} - Mult^{MC})/Mult^{data}$ obtained using Monte Carlo predictions before (green points) and after (red points) the corrections versus the mean number of interactions per bunch crossing (mu).

4.4 Determination of the CFD Thresholds by Data

Befor the LHC start up, the correspondence between the value of the CFD thresholds in mV and the number of photoelectrons has been evaluated, knowing the relation between the charge and the amplitude of the signals. The CFD thresholds have been set so as to correspond to 15 photoelectrons using the procedure described in section 4.4.1. The CFD thresholds are important to define a hit in LUCID. As a consequence, a correct evaluation of the CFD thresholds is mandatory for the measurement of the efficiency. Moreover, it is important to estimate how the efficiency in the detection of hits will change as a function of the threshold positions. An increase in the threshold may be necessary with increasing luminosity to cope with the migration effect. At high luminosity, in fact, a lot of secondary particles at low energy will be produced. It may happen that the small signals given by these particles sum up and pass the threshold, faking the effect of a high energy track.

4.4.1 CFD Threshold Calibration with Pulser Signals

Setting the optimal thresholds is not trivial. They should be as high as possible to avoid triggering noise, but low enough to collect all the usefull data. Before the LHC start up, the CFD thresholds have been calibrated using signals from a pulser.

The first step was to evaluate the transfer functions of the electronics as measured by the QDC and the FADC. The method consisted into injecting a signal of known amplitude into the electronics immediately after the PMTs and measuring the output. The input signal has then gradually increased and the measurement repeated until the output was known for every input, yelding a transfer function. Figures 4.17 and 4.18 show the charge and amplitude transfer functions for tube 29 as obtained by the QDC and the FADC respectively. The saturation point of the two modules has been measured as well as the range of linearity. Table 4.9 reports the values of the slope and the amplitude of both the QDC and FADC transfer functions for each tube, as obtained fitting the transfer function with a polinomial of first order.

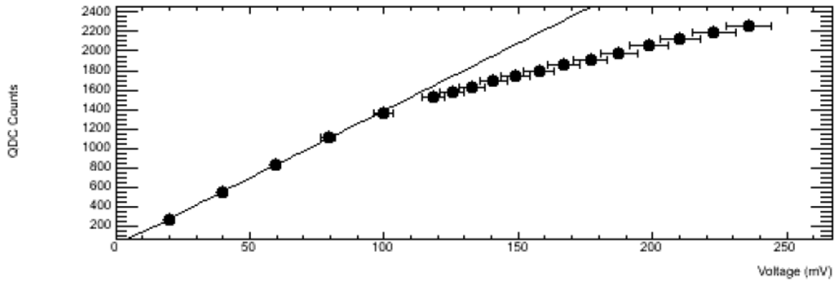

Figure 4.17: Charge transfer function for tube 29 as measured by QDC.

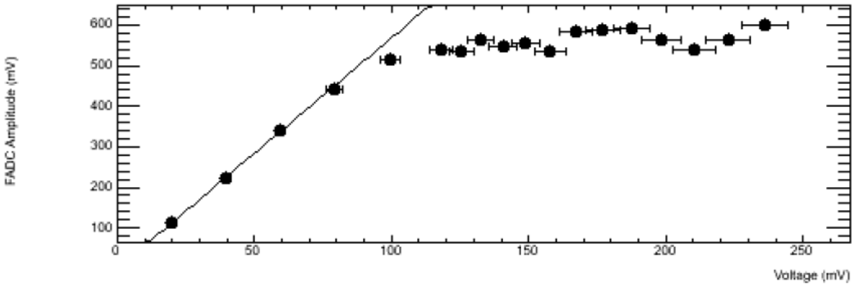

Figure 4.18: Amplitude transfer function for tube 29 as measured by FADC.

	Side A			*Side C*	
Tube	**Charge TF slope** (QDC counts/mV)	**Amplitude TF Slope**	**Tube**	**Charge TF slope** (QDC counts/mV)	**Amplitude TF Slope**
0	12.77	4.66	20	13.65	4.86
2	12.80	5.04	21	14.15	5.69
3	13.47	5.18	22	13.78	5.58
4	12.10	4.86	23	13.68	5.05
5	12.44	4.68	24	13.57	5.13
6	13.11	5.10	25	13.35	5.24
7	13.02	4.97	26	13.21	5.18
8	12.50	4.34	27	13.54	5.32
9	13.17	4.92	28	13.81	4.71
10	12.83	4.97	29	13.87	5.69
11	12.91	4.81	30	14.09	5.31
12	13.17	5.15	31	14.17	4.86
13	13.07	5.03	32	12.49	4.83
14	12.89	4.90	33	13.81	5.24
15	12.82	4.81	34	13.37	5.21

Table 4.9: Angular coefficients of the charged and amplitude transfer functions for each tube. The amplitude transfer function slope has no unit since both the FADC amplitude and the input signal are measured in mV. The transfer functions are assumed to pass through the origin and the slope are only valid up to roughly 100 mV. No results are reported for tube 1 and 35 because they correspond to broken PMTs.

In the second step, the electronics after the PMTs was pulsed at a constant rate of 700 Hz with an input signal of a certain voltage. Initially, the CFD threshold

was set to its maximum value, so that no events were registered. The logic OR of the CFD, in fact, gives the trigger for the local stream data to be recorded. The threshold was gradually lowered until the trigger rate reached the pulser rate. The input voltage was increased and the measurement repeated until the proper threshold was known for every input, yelding a calibration function. Figure 4.19 shows the calibration function for tube 8, while table 4.10 reports the offset and slope obtained by fitting the calibration functions for each tube.
If the expected mean number of photoelectrons produced in the Cherenkov tube can be estimated, the CDF calibration function can be used together with the charge transfer function to calculate the appropriate CDF threshold for any tube. The CDF thresholds have been initially set at 15 photoelectrons for each tube to see the first splash events (see chapter 3) and was then kept at this value, since the background remains at a level of about 1 Hz.

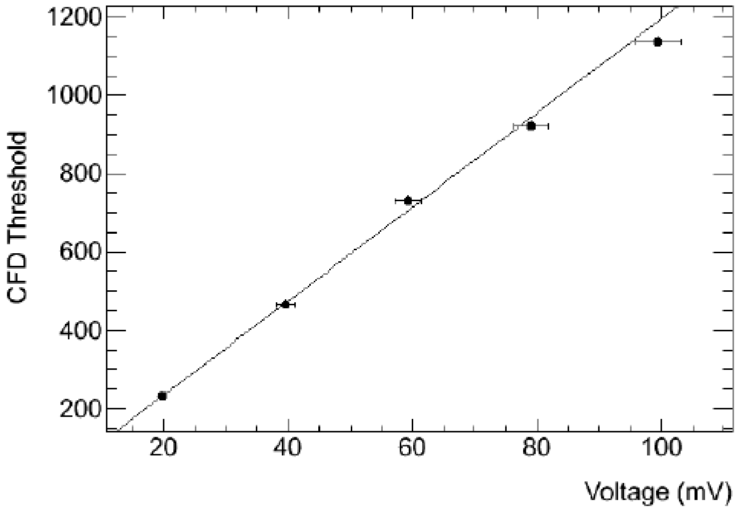

Figure 4.19: The calibration function for the CFD threshold for tube 8.

4.4.2 Threshold Positions from Data

Once LHC started to take data, the positions of the CFD thresholds had to be controlled with real data. The relation between charge and amplitude of the signals can differ from calibration to real data, due to the fact that the shape of pulser signals can differ from the one of PMT signals. The QDC charge distribution for events where only one hits was recorded (see figure 4.20) has been fitted tube by tube in the region from 10 to 20 photoelectrons with a S-shaped Fermi function.

	Side A			*Side C*	
Tube	**Offset** (mV^{-1})	**Slope**	**Tube**	**Offset** (mV^{-1})	**Slope**
0	-8.16	12.75	20	-13.56	13.67
2	-20.21	14.60	21	-12.78	15.70
3	-17.18	13.18	22	-26.66	15.71
4	-1.23	13.57	23	-6.77	14.20
5	-14.00	13.23	24	0.35	14.10
6	-18.73	14.55	25	-17.21	14.03
7	-2.74	14.01	26	-17.64	14.36
8	-5.72	12.01	27	-8.78	13.48
9	-19.73	14.31	28	-12.15	13.41
10	-15.57	14.42	29	-8.35	15.44
11	-13.66	13.67	30	-18.07	15.50
12	-8.14	14.62	31	-3.30	15.17
13	-18.60	14.18	32	0.10	13.45
14	-15.43	14.28	33	-13.27	13.83
15	-9.95	13.80	34	-13.63	14.27

Table 4.10: Offset and slope obtained from fitting the CFD calibration function for each tube. No results are reported for tube 1 and 35 because they correspond to broken PMTs.

The Fermi functions goes from 1 to 0 and is shaped like an S. The width of the S depends on kT, where T is the temperature and k is the Boltzman constant, and at the absolute zero it is a step function:

$$f(E) = \frac{1}{1 + e^{(E-E_F)/kT}} \tag{4.11}$$

where E is the energy and E_F is the Fermi energy. The fit used here is a modification of the Fermi function, obtained by negating the exponent so that the function goes from 0 to 1. The function is then scaled by an amplitude factor yielding the formula:

$$f(x) = \frac{A}{1 + e^{(\mu-x)/w}} \tag{4.12}$$

where A is the amplitude, μ is the inflection point and w is the width. The real thresholds with their statistical errors are listed in table 4.11 for each tube.

Tube	Real threshold	Tube	Real threshold
0	17.0 ± 0.41	20	17.3 ± 0.30
2	15.9 ± 0.46	21	16.2 ± 0.36
3	16.4 ± 0.32	22	16.4 ± 0.57
4	18.2 ± 0.31	23	16.7 ± 0.33
5	16.1 ± 0.29	24	16.5 ± 0.36
6	16.4 ± 0.35	25	15.2 ± 0.39
7	17.9 ± 0.47	26	16.1 ± 0.30
8	16.6 ± 0.32	27	16.1 ± 0.26
9	15.7 ± 0.72	28	17.0 ± 0.29
10	16.4 ± 0.37	29	16.4 ± 0.34
11	16.5 ± 0.30	30	14.8 ± 0.36
12	18.8 ± 0.41	31	17.1 ± 0.77
13	16.4 ± 0.28	32	17.2 ± 0.30
14	16.2 ± 0.58	33	15.2 ± 0.29
15	16.6 ± 0.31	34	16.1 ± 0.26

Table 4.11: Position of the CFD threshold for each tube as measured for real data. The nominal value is 15 photoelectrons for each tube. No results are reported for tube 1 and 35 because they correspond to broken PMTs.

Accuracy on the Threshold Positions

Knowing the accuracy on the determination of the position of the thresholds is important when determining the efficiency of the detector. The same distributions

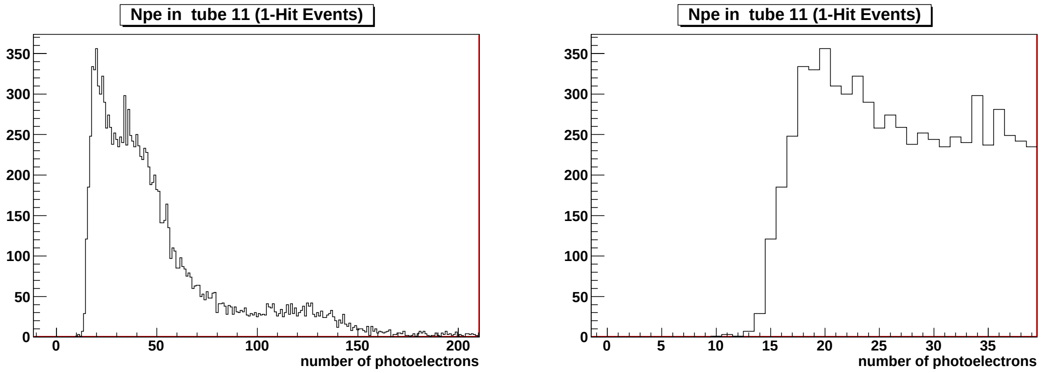

Figure 4.20: Left: charge distribution for tube 6 for events where only one hit is recorded in the tube under study. Right: zoomed view of the first region of the plot on the left, region in which the accuracy on the threshold position is evaluated.

as studied for the evaluation of the threshold positions have been used to measure the accuracy on the threshold positions itself. The accuracy on the threshold position has been evaluated as half of the width of the Gaussian function that best fits the region between 10 and 20 photoelectrons. A typical QDC charge distribution with relative zoomed view in the region of interest is shown in figure 4.20. The accuracy on the threshold position is reported tube by tube in table 4.12. The statistical error on the accuracy is about 2%.

Side A	
Tube	**Accuracy**
0	1.015
2	1.073
3	1.081
4	0.923
5	1.172
6	1.126
7	1.248
8	1.153
9	1.098
10	1.155
11	1.093
12	1.245
13	1.098
14	1.112
15	1.211

Side C	
Tube	**Accuracy**
20	1.063
21	1.112
22	1.053
23	1.102
24	0.922
25	1.259
26	1.084
27	1.217
28	0.961
29	1.189
30	1.206
31	1.197
32	0.977
33	1.208
34	1.020

Table 4.12: Accuracy on threshold position tube by tube. Statistical error on the accuracy is about 2%. No results are reported for tube 1 and 35 because they correspond to broken PMTs.

4.4.3 Relation between Amplitude and Charge in Data

The knowledge of the exact position of the threshold is important when using the Monte Carlo simulation to provide accurate predictions on the algorithms for luminosity calculations. A check on the threshold position can be done using the relation between the amplitude provided by the FADC and the charge measured by the QDC.

Once the transfer functions of both QDC and FADC have been measured with pulser data, the relation between amplitude provided by the FADC and charge measured by QDC is known. The amplitude versus charge calibration have to be compared with the ones obtained from real data, once LHC started running. This comparison is important because the relation between amplitude and charge strongly depends on the shape of the signal, that may differ from pulser to data signals.

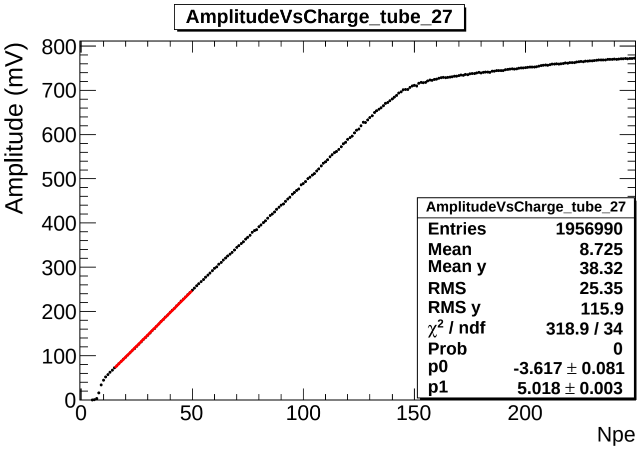

Figure 4.21: Dependency of amplitude provided by FADC on charge measured by QDC for tube 27. Different regions of linearity are present. The results of the linear fit of the first region, from 15 to 50 p.e, in which LUCID worked in 2010 LHC running, is shown.

The typical amplitude versus charge dependency for a tube is shown in figure 4.21. Different regions of linearity are present. The region before 15 photoelectrons will be not considered in next analysis since it is below the CFD threshold. The first region of linearity extends from about 15 to 50 photoelectrons, fitted in red line in figure 4.21. The second one extends from about 50 photoelectrons to the region of saturation, that differs from tube to tube. The two regions of linearity are not very well distinguishable, but from fitting separately the plot in the two different regions it is visible that the slopes are different. The two regions of linearity correspond to different linearity dependencies in the range of work of the electronics. The results of the linear fit in the two regions are reported in table 4.13.

The saturation plateau is reached when, beyond a certain threshold, an increase in the input signal amplitude does not imply an increase in the amplitude as measured by the FADC. Since the amplitude is evaluated using only the baseline and the peak position of the FADC shape, the amplitude remains constant. On the contrary, the charge integrated by the QDC continues to increase because the signal becomes larger while the QDC gate is fixed in time.

Knowing the linearity regions of the electronics is important to understand what

Range	**Offset**	**Slope**
15-50 pe	-3.617±0.081	5.018±0.003
50-140 pe	5.562±0.260	4.842±0.004

Table 4.13: Results of the linear fit over the two different regions of linearity that characterized the dependency of amplitude on charge in real data.

factor of amplification is necessary to best exploit the dynamic range of the QDC and FADC. It is possible to define tube by tube a rought estimate of the amplitude and relative number of photoelectrons at which the saturation begins from plots in figure 4.21. The results are listed in table 4.14 for each tube. The accuracy of the results can not be better than the intrinsic resolution given by the precisions of the calibration constant (2-3 photoelectrons) as well as the threshold position (see table 4.12). In 2010, LUCID worked in the first region of linearity. Only the region from 15 to 50 photoelectron is considered for the next analysis.

	Side A			*Side C*	
Tube	**Ampl (mV)**	**Npe**	**Tube**	**Ampl (mV)**	**Npe**
0	740	180	20	750	180
2	740	160	21	730	160
3	740	170	22	710	150
4	740	160	23	750	180
5	750	180	24	750	180
6	740	160	25	700	150
7	730	160	26	700	150
8	740	190	27	700	150
9	740	180	28	730	180
10	700	150	29	700	150
11	740	170	30	670	170
12	750	170	31	720	180
13	750	170	32	750	180
14	750	170	33	730	180
15	760	190	34	750	180

Table 4.14: Typical values of amplitude and number of photoelectrons corresponding to saturation for each tube. No results are reported for tube 1 and 35 because they correspond to broken PMTs.

To evaluate the slope of the dependency of the amplitude on the charge all the

Tube	$\overline{Slope}$	**Var Slope**	$\overline{Offset}$	**Var Offset**	**Calib Slope**	**Calib Offset**
0	4.698	0.002	-4.519	0.059	5.497	0.204
2	5.137	0.002	-3.951	0.057	5.943	-0.342
3	5.056	0.004	-3.486	0.154	5.805	-0.438
4	5.032	0.001	-4.401	0.140	6.053	0.134
5	4-985	0.001	-4.275	0.092	5.671	-0.105
6	5.150	0.002	-4.198	0.188	5.865	0.038
7	5.069	0.004	-4.388	0.267	5.750	0.323
8	4.614	0.001	-4.182	0.228	5.240	-0.344
9	4.891	0.005	-4.409	0.186	5.641	-0.593
10	5.068	0.006	-3.734	0.240	5.839	-0-022
11	4.852	0.004	-2.952	0.138	5.609	0-549
12	5.122	0.006	-3.809	0.675	5.897	-0.105
13	5.003	0.002	-4.172	0.165	5.798	0.204
14	5.092	0.006	-3.527	0.218	5.738	-0.521
15	4.919	0.001	-3.080	0.299	5.656	0.121
20	4.915	0.003	-3.512	0.363	5.370	-0.106
21	5.199	0.005	-3.301	0.701	6.061	0.0504
22	5.105	0.005	-3.637	0.264	6.103	0.134
23	5.066	0.003	-2.551	0.118	5.565	0.097
24	4.970	0.001	-3.694	0.475	5.698	0.204
25	5.091	0.004	-3.956	0.627	5.907	0.621
26	5.013	0.003	-3.584	0.445	5.910	0.050
27	5.022	0.009	-3.535	0.562	5.925	0.014
28	4.636	0.002	-3.896	0.357	5.144	-0.107
29	5.253	0.002	-4.782	0.452	6.185	-0.009
30	4.874	0.058	-3.808	0.725	5.682	-0.070
31	4.798	0.011	-3.330	0.338	5.169	-0.106
32	5.241	0.002	-2.623	0.376	5.824	0.014
33	4.859	0.005	-3.586	0.237	5.724	0.014
34	5.003	0.001	-3.878	0.373	5.877	0.133

Table 4.15: Average offset and slope over all the runs taken in 2010 LHC running, as well as their variances, as obtained from fitting the relation between amplitude, provide by FADC, and charge, measured by QDC, in the region between 15 and 50 p.e. The results from calibration data are reported in the last two columns. The errors on the fit results are less than 1%. No results are reported for tube 1 and 35 because they correspond to broken PMTs.

runs taken during the LHC running have been studied. The fit to the dependency of amplitude on charge in the region under study has been performed for each tube and run. The results of the means of slopes and offsets over all the runs, as well as their variances, are listed in table 4.15 for each tube. The results of the fit on pulser data are reported in the last two columns. The errors on the fit results for both the slope and the offset are less than 1%. The slopes are stable within 1 and 5% from tube to tube, while they are in disagreement with the results from pulser data: the nominal thresholds, set before the LHC start up, corrspond in real data to signals of lower amplitude. This aspect, actually, does not represent a problem for the luminosity evaluation, once the efficiency of single interaction is kwown for each threshold, as presented in section 4.4.4.

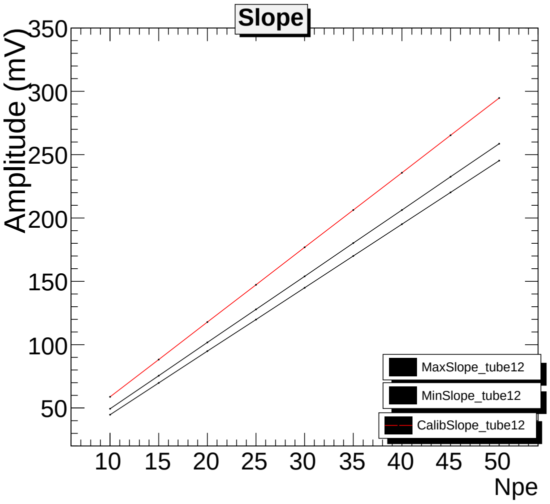

Figure 4.22: The function that fit the slope of the amplitude-to-charge relation as observed with calibration data (red line) is compared with the functions obtained fitting real data (black lines) for tube 12. Both the maximum and minimum slopes and offsets of the fit have been used to build the black functions. The value of the threshold provided by calibration data is understimated with respect to one obtained from real data.

The relation between amplitude and charge as obtained from pulser data and real data is shown in figure 4.22 for tube 12. All the other tubes show similar behaviour. The two functions plotted in balck have been built using the maximum and minimum slopes and offsets obtained while fitting the amplitude vesus charge relation run by run. The slope and the offset obtained from pulser data are used to build the function plotted in red. In calibration data, the threshold at 15 photoelectrons corresponds to a signal amplitude of 90 mV. The same amplitude in real data is obtained setting the threshold to about 19 photoelectrons, value which corresponds to the position of the threshold as evaluated with real data (see table 4.11). The initial values of the thresholds provided by pulser data are, in conclusion, understimated, but it is not a problem for the luminosity calculation.

4.4.4 Relation between Efficiency and Threshold

With the increase of the luminosity, the migration effect will begin to increase as well. To cope with the migration effect, it may be useful to increase the CFD thresholds. It is advisable to evaluate the resulting change in the efficiency for the detection of a single interaction, because changing the threshold also means changing the luminosity calibration. The variation of the single interaction efficiency is, in fact, the parameter needed to evaluate the change in the normalization of the luminosity, as described in details in chapter 5. The efficiency for a single interaction can be evaluated from runs in which the mean number of expected interactions per bunch crossing (μ) is low, or the probability of multiple interactions in a bunch crossing is negligible.

The dependency of the efficiency on the CFD threshold has been studied. The efficiency of the detection of a *pp* interaction in both single side and coincidence mode has been evaluated using the charge collected by the QDC. For each event the maximum and minimum charges collected by the tubes are considered. The maximum QDC charge corresponds to the CFD threshold cut in single side mode while the minimum QDC charge corresponds to the CFD threshold cut in coincidence mode the event passes. The bins of the histograms are filled till the value of the CFD threshold. The efficiency for each CFD threshold is evaluated performing the ratio between the number of events which pass the CFD threshold cut and the total number of events. The dependency of the efficiencies on the CFD threshold are shown in figure 4.23. A normalization has been done with respect to the number of events that pass the standard cut at 15 photoelectrons. As visible from both plots, a change in the threshold cut determines a change in the number of recorded events, in percentage that depends on the threshold itself.

In practice, studying the dependency of the efficiencies for the detection of a single interaction on the CFD threshold in run at low μ provides important information on the corrections to the luminosity calibration given by $\epsilon\sigma$, where ϵ is the efficiency and σ is the cross section, as fully explained in chapter 5.

At higher μ values, the migration effect starts to play an important role: at high μ the probability of multiple interactions increases, as a consequence several particles at low energy are produced. Each low energy particle produces a number of photoelectrons that are below the CFD threshold. However, when a lot of low energy particles are produced, the total number of photoelectrons is above the CFD threshold. Studying the dependency of the efficiency for single interaction detection on the CFD threshold in runs at high value of μ provides a first evaluation of

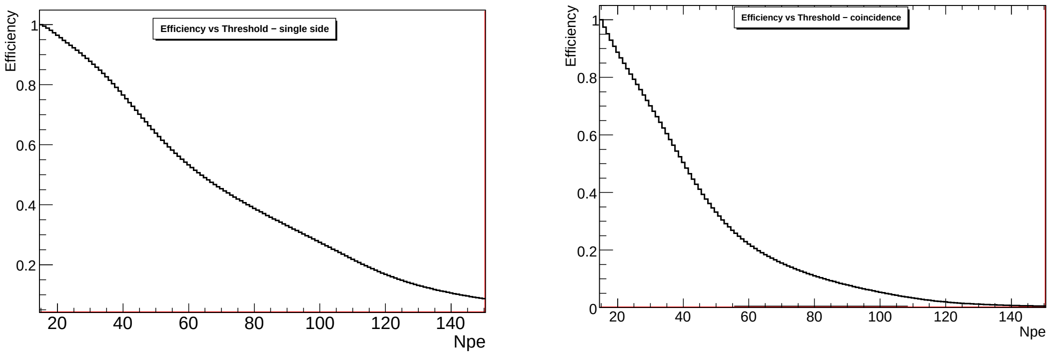

Figure 4.23: Efficiency for the detection of single pp interactions in single side mode (left) and in coincidence mode (right) with respect to the CFD threshold cut the events pass. Both plots refer to a run at a luminosity of $6 \cdot 10^{27} cm^{-2} s^{-1}$ with a μ of 0.0384. The plots are normalized to the events that pass the standard cut at 15 photoelectrons.

the effect of the migration on the efficiency. Two runs taken at different μ values have been compared. The dependency of the efficiency on the CFD threshold cut changes as visible in figure 4.24 and the slope is smoother in case of high μ, as expected, probably due to the presence of migration effect. A cross-check has been done comparing two runs taken at very similar and low μ values. In this case the difference in the behaviour of the efficiency for the two runs is negligible.

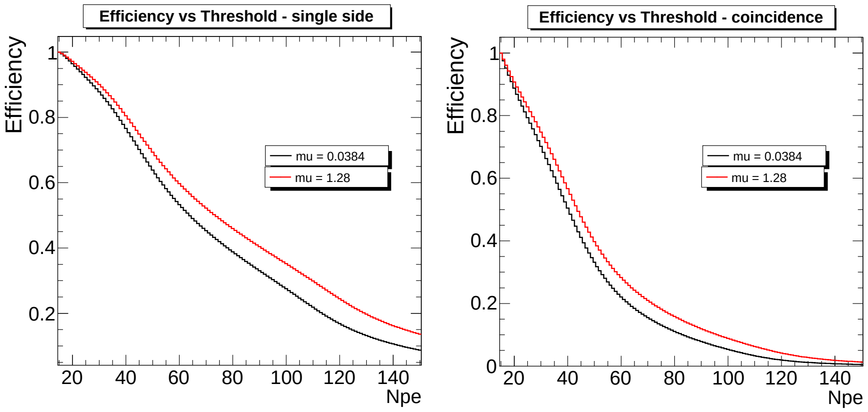

Figure 4.24: Efficiency for the detection of single pp interactions in single side mode (left) or in coincidence mode (right) as a function of the CFD threshold the events pass for two runs at different μ values: μ=1.28 in red line and μ=0.0384 in black line. The plots are normalized to the events that pass the standard cut at 15 photoelectrons. The dependency of the efficiency on the CFD threshold is affected by the migration effect.

4.5 LUCID Timing

It is important to verify that the LUCID signals have the necessary time resolution to separate collisions coming from different bunch crossing.
The shapes of the signals from the PMTs are sampled by four FADC modules, two for side A and two for side C. The local stream trigger, given by the OR of the CFDs, is fanned-out and distributed to the four modules. The FADC trigger is used to gate the readout, in order to sampling the signals in a programmable window on time every 4 ns. Since the PMTs 1 and 35 are broken, the FADC channels corresponding to those PMTs are used to monitor the LHC clock. The difference in time between the arrival of the FADC signal and the LHC clock has been measured. A typical time distribution of the fitted peak position of the signal from one photomultiplier as measured by the FADC is shown in figure 4.25. The time is here measured with respect to the arrival of the bunch crossing signal but with an arbitrary zero time in the plot. The tail in the distribution is caused by secondary particles with a slightly longer flight path than the primary particles. The time of arrival of the signals has an intrinsic resolution of 1 ns, as shown in figure 4.25.

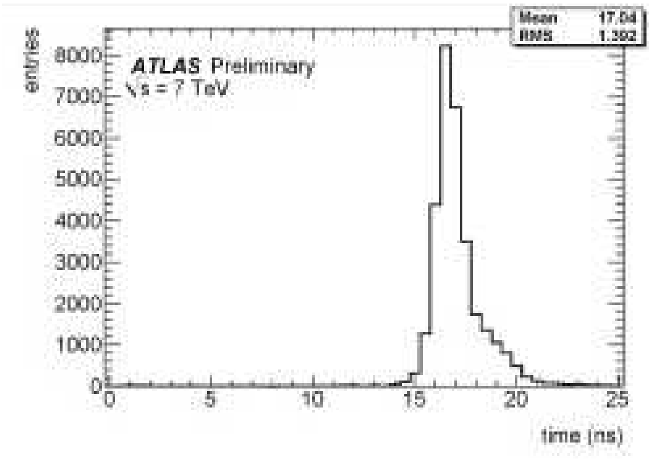

Figure 4.25: Typical time distribution of the fitted peak position of the signal from one photomultiplier as measured by the FADC. The time is measured with respect to the arrival of the bunch crossing signal but with an arbitrary zero time. The tail in the distribution is caused by secondary particles with a slightly longer flight path than the primary particles. The typical time resolution is about 1 ns.

The time alignment of all the signals coming from the PMTs is important for the luminosity calculation as it is implemented in the LUMAT card. The LUMAT card receives a logic signal 10 ns long from the CFD, if the correspondent signal

in the tube is above threshold. Since the CFD are not aware of the LHC timing, the signals must be aligned with the LUMAT registers so as to make each logical hit fall within a 25 ns time window (BC). If a signal falls between two successive window, the LUMAT counts double and the luminosity is incorrectly evaluated. Considering the time resolution of 1 ns and the duration of 10 ns of the signal in input to the LUMAT, an alignment of all the PMT signals of about 3-4 ns is sufficient to guarantee that all signals are received in the time window of 25 ns.
To control the time alignment, the time of arrival of the PMT signals to the LUMAT register has been studied; an example is shown in figure 4.26. Each column in the plot shows the time distribution of the signals from one PMT whitin a window of 25 ns corresponding to one BCID. Tubes on side C are, on average, earlier than in side A by about 3 ns (fixed offset), but it is possible to conclude that the time allignement is sufficient to accomplish consistent luminosity measurements.

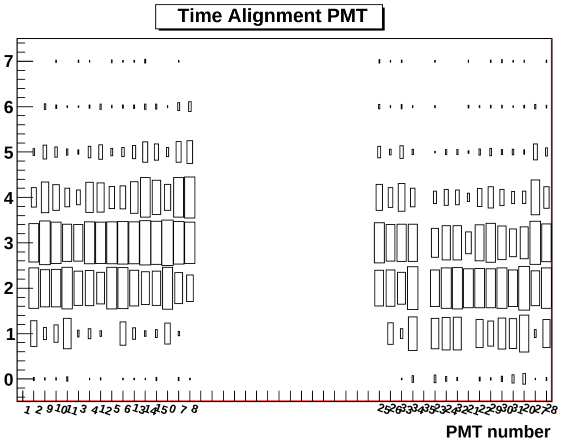

Figure 4.26: Time arrival of signals from all tubes as seen by the LUMAT card for a typical run.

4.6 Stability Studies

LUCID is a luminosity monitor, that implies that it can only measure the relative luminosity. To have the absolute luminosity, some calibration is needed, as described in more details in chapter 5. Once a calibration constant is provided, it is possible to correct all the data collected with the LUCID detector till that moment. Verifying the stability of LUCID over long periods is thus mandatory. Stability checks are also important to guarantee the good performances of the detector. Some of the most relevant checks on the LUCID stability are described in this section.

4.6.1 Stability of Peaks Positions

Assuming the stability of the PMT gains thanks to the day-by-day adjustments, the study on the stability of the peak positions can provide some information about the amount of the migration effect.
All the runs thaken during the 2010 LHC running have been studied; in figure 4.27 only a small group of runs is shown since the general behaviour of the trending of the peak positions is well represented by this smaller subset of data. For each run and tube, the two peaks of the charge distribution obtained from the QDC have been fitted with a Gaussian. An exponential has been used to model the smooth part of the distribution. The statistical errors on the fit results are less than 1%. The requirement of the chi-square parameter to be smaller than 2 guarantees the robustness of the fit. The peak positions found by the fits for both quartz and quartz plus gas peaks are plotted together with the results of calibration runs performed just after and just before the runs under study. The trending plots of mean number of photoelectrons corresponding to both the quartz peak and the quartz plus gas peak are presented in figure 4.27 for tube 10. The calibration values are reported in number of QDC bins.

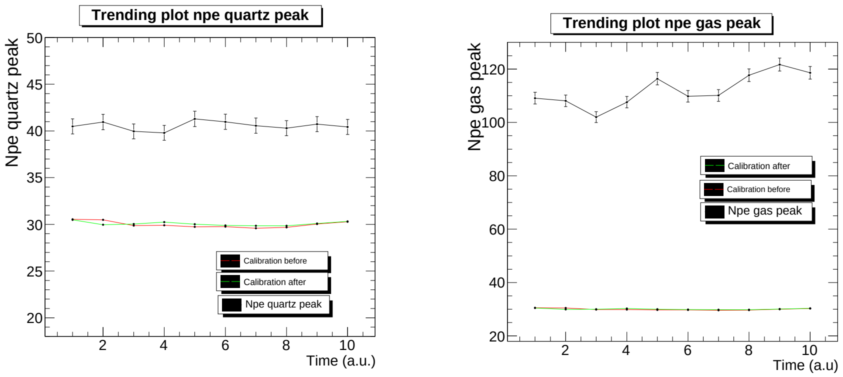

Figure 4.27: Trending plots over ten runs (in arbitrary time units) of the npe corresponding to the quartz peak (left) and quartz plus gas peak (right) for tube 10 as obtained fitting the charge distribution. The results for calibration runs performed just before (red) and just after (green) the run under study are reported in number of QDC bins.

To evaluate the stability of the peak positions, the fractional ratio between the first run, taken as reference, and the other runs has been performed tube by tube.

The results for tube 10 are shown in figure 4.28. The same procedure has been done for all tubes. The first peak position is stable within 1-5% while the second peak position is stable within 10-15%. The slow rise of the position of the second peak in time is probably due to the migration effect and not to fluctuation on the PMT gain, since the calibration is stable in time as visible in figure 4.27.

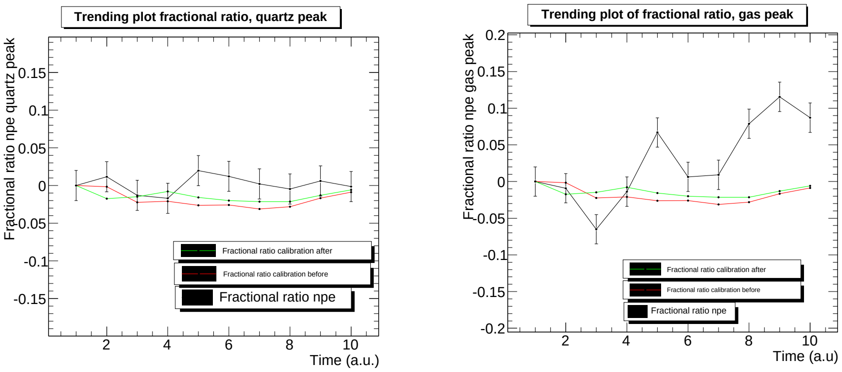

Figure 4.28: Trending plots over 10 runs (in arbitrary time units) of the fractional ratio of the npe corresponding to the quartz peak (left) and quartz plus gas peak (right) for tube 10. The first run has been considered as the reference one.

4.6.2 Stability of Hit Definitions

A hit is defined as a signal in a tube above the CFD threshold. The stability of the definition of a hit is important for the luminosity calculation, as it will be described in chapter 5. In case of high rate of *pp* interactions, the baseline of a PMT signal as measured by the FADC can not be restored quickly enough before the arrival of a second signal. Baseline migration at high rate is a typical problem in signal analysis. It affects the actual position of the CFD threshold, which acts on the FADC amplitude.

To verify the stability of the thresholds definition, all the runs with sufficient statistics taken during 2010 LHC running have been considered. The threshold position has been evaluated as described in section 4.4 for each tube and for each run. The trending plot of the threshold position for tube 11 is shown in figure 4.29. The threshold position remains stable within the intrinsic uncertainty listed in table 4.12. The stability guarantees the robustness of the luminosity calculation. Moreover, different cross checks on the luminosity measurements using other ATLAS monitors confirm the method used by LUCID for the luminosity calculation.

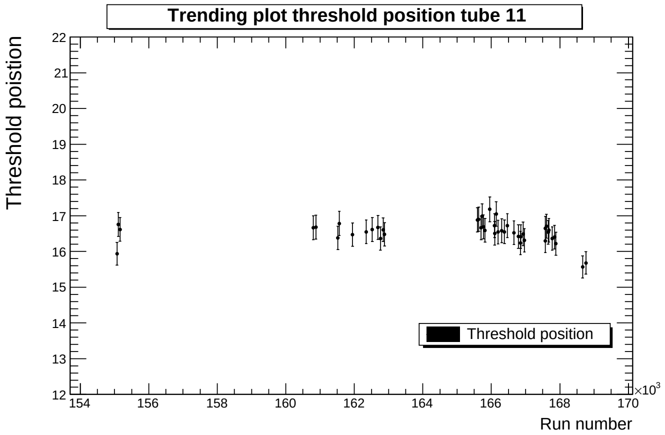

Figure 4.29: Trending plot of the threshold positions for tube 11 for the runs with sufficient statistics taken during 2010 LHC running.

4.6.3 Stability of Module Response

Another check on the stability of LUCID can be done by observing the hits recorded tube by tube during a Luminosity Block (LB). The typical pattern of the number of hits recorded tube by tube in a LB is shown in figure 4.30.
Many aspects can be controlled using these data. First of all, the number of recorded hits must be similar in side A and in side C to guarantee the same efficiency in the detection of *pp* interactions. Second, the number of hits counted by each tube must be similar tube by tube, since the the PMT gains are equilized on day-by-day basis. On the contrary the absolute number of hits recorded by each tube differs according to the luminosity of the runs under study.

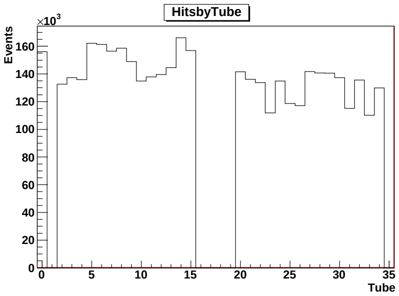

Figure 4.30: Typical pattern of number of hits recorded tube by tube for a run in a LB.

As is visible in figure 4.30, module A is more efficient than module C. This result is not surprising after having studied the effects of the residual magnetic field on tubes performances, as see in section 4.3.3. In side A some tubes seem to count more than the others: 5, 6, 7, 8, 9, 14, 15. In side C, on the contrary, some tubes seems to count less: 23, 25, 26, 31, 33. The relative positions of the most efficient tubes in side A is shown in figure 4.31: they all belong to the bottom-right part of the vessel. The calibration were fine for all these runs and the background evaluated from a run without collisions confirms that it is kept at a level of 1 Hz. A possible explanation of the clustering of the most efficient tubes is given by some hypotetical asymmetries in the alignment of the vessels with the beam line, but this hypothesis can not be further demonstrated.

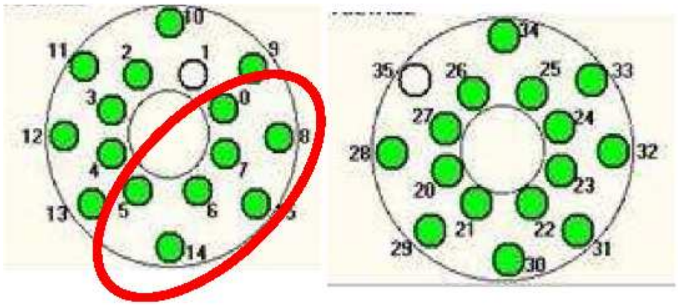

Figure 4.31: Relative positions of tubes in vessel A (left) and vessel C (right). The red circle corresponds to the most efficient tubes.

However, the most important aspect is that this behaviour of LUCID does not change in time. In order to verify the stability in time, the shape of the hit distribution over tubes have been studied for all the runs taken during 2010 LHC running. The pattern of the number of hits recorded tube by tube remains similar during all 2010 LHC running, which guarantees the stabililty in time of the LUCID response. The comparison for two runs randomly choosen among all runs is shown in figure 4.32.

4.7 Conclusions

Before the LHC start up, the electronics transfer function as measured from both the QDC and FADC have been built using pulser signals, and the CFD thresholds have been calibrated in terms of photoelectrons. Combining the results of the transfer function of QDC and FADC, the relation between amplitude as provided by FADC and charge as measured by QDC has been evaluated. Since pulser signals are not identical in shape to the PMT signals, the CFD threshold positions have been re-evaluated a posteriori using real data. The exact position

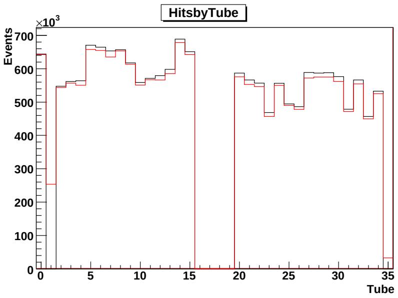

Figure 4.32: Shape of the distribution of the number of hits recorded tube by tube during a LB for two runs randomly choosen during the 2010 LHC running. The two histograms are normalized to the same number of entries. The pattern of the hits recorded tube by tube is very similar in both runs, that guarantees the stability of the LUCID performances. The entries which are visible in the tubes 1 and 35 are referred to fibers for side A and side C respectively, only for study purposes.

of CFD thresholds is important for the definition of a hit in LUCID: a PMT signal in a tube above threshold. Real CFD threshold positions as well as the functional dependency of the amplitude on charge have been evaluated using real data.

Moreover the charge distribution provided by the QDC for each tube has been used to adjust the Monte Carlo predictions. A tuning of Monte Carlo prediction was necessary to simulate the effect of the residual toroid magnetic field in the LUCID region, effect not yet included in previous simulations, as well as difference in the mechanical characteristics from tube to another.

Finally, the local stream plays an important role in assessing the detector stability. All the checks performed in this chapter have demonstrated the correct behaviour of the LUCID detector during all the 2010 LHC data taking.

Chapter 5

Luminosity Monitoring with LUCID

5.1 Introduction

A stable monitor of the relative luminosity is mandatory to control the bunch structure as well as the beam degradation, in order to change efficiently the trigger, and for the machine optimization. This section is dedicated to the description of LUCID detector as luminosity monitor.

5.2 Luminosity Algorithms

Relative luminosity monitoring is in principle simple. It is based on the idea that the number of particles detected is proportional to the number of particles produced. Thus, once the exact form of the proportionality is known, only a fraction of the produced particles actually need to be counted. As discussed in chapter 2, the instantaneous luminosity can be calculated as:

$$L = \frac{\mu n_b f_r}{\sigma_{inel}} = \frac{\mu^{meas} n_b f_r}{\epsilon \sigma_{inel}} = \frac{\mu^{meas} n_b f_r}{\sigma^{vis}} \tag{5.1}$$

where, in the specific case of LHC, μ is the average number of interactions per bunch crossing, σ_{inel} is the pp inelastic cross section and ϵ is the efficiency of the considered luminosity algorithm including detector acceptance, $\mu^{meas} = \mu\epsilon$ is the average number of interactions that pass the selection requirements of the algorithm and the *visible* cross section $\sigma_{vis} = \epsilon \cdot \sigma_{inel}$ is the detector calibration constant, also referred to as the normalization. In general, this equation is valid only in the case of a linear response of the detector with respect to μ, otherwise corrections for the non linearity must be taken into account.

The LUCID detector, located in the forward region, is designed to measure charged particles produced in inelastic proton-proton scattering processes. It makes use of different counting methods [36] to evaluate the value of μ^{meas} needed for the luminosity calculation. A full description of these methods is presented in next sections.

5.2.1 Counting Methods

LUCID consists of two modules simmetrically placed with respect to the ATLAS interaction point. Two criteria to detect a *pp* collision can be defined considering LUCID geometry: single side mode and coincidence mode. In single side mode, a *pp* interaction is detected if at least one hit is counted in any module. In coincidence mode, a *pp* interaction is detected if at least one hit is counted in each module. A pictorial view of the counting logic is presented in figure 5.1: in case a) each module detects a particle, so that the interaction is detected both in single side mode and in coincidence mode; in case b) two particles traverse the same module giving a hit: this interaction is detected in single side mode only; in case c) no particle traverses any module and no interaction is detected.

The advantage of requiring a coincidence is that background produced by cosmics, beam interactions with residual gas inside the beam pipe or by the beam-halo is reduced. Since these events are uncorrelated with the ATLAS interaction point, such interactions are, in fact, detected in one module only.

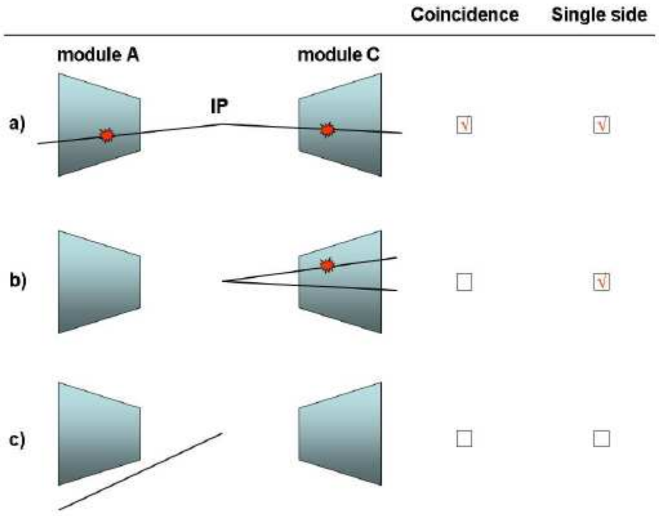

Figure 5.1: Principle of detection in single side and coincidence modes.

A fundamental ingredient of the ATLAS strategy to assess and control the systematic uncertainties affecting the absolute luminosity determination is to compare the measurements of several luminosity detectors, most of which use more than one counting thecnique. These multiple algorithms are characterized by significantly different acceptance, pile-up response and sensitivity to instrumental effects and to beam-induced background. The level of consistency across the various methods, over the full range of single-bunch luminosities and beam conditions, provides valuable cross-checks as well as an estimate of the detector-related systematic uncertainties. Techniques for luminosity determination can be classified as follows:

- *hit counting*: the number of hits per bunch crossing are counted.
- *event counting*: the fraction of bunch crossings during which at least one event satisfies a given selection requirement is counted. For LUCID, a pp collision is detected as an event if it induces at least one observed hit.

At present, ATLAS relies only on event-counting methods for the determination of the luminosity, but all these methods are implemented in the LUMAT card both in AND (coincidence) and in OR (single side) logic.
The event AND probability per beam crossing $P^{eventAND}$ is related to the zero OR probability. The event AND algorithm corresponds to case a) in figure 5.1, in the other cases either one of the two modules or both of them have no hits: this configurations corresponds to the zero OR algorithm. The probability of having an event AND counting (case a) is thus the complementary of the probability of having a zero OR counting (case b and c):

$$P^{eventAND} = 1 - P^{zeroOR} \tag{5.2}$$

In single side event counting (event OR) at least one hit is detected in any of the two modules, which corresponds to cases a) and b) in figure 5.1. The last case c) corresponds, on the contrary, to the zero AND algorithm. The event OR probability per beam crossing $P^{eventOR}$ is thus the complementary of the zero AND probability:

$$P^{eventOR} = 1 - P^{zeroAND} \tag{5.3}$$

All the counting methods are summarized in table 5.1.

The hit counting method is equivalent to the event counting at the level of single tube, the result being the average on all tubes.

5.2.2 Determination of μ

The LUCID LUMAT card provides bunch-by-bunch, raw luminosity information for each LB, as well as the luminosity at Hz frequency over all colliding bunches. The general formula used to evaluate the luminosity is an extension of

Measured quantity	**Side A**	**Side C**	**Name**
$P^{OR}_{hits/BX}$	$N_{hits} \geq 1$	$N_{hits} \geq 1$	event counting OR
	$N_{hits} = 0$	$N_{hits} \geq 1$	
	$N_{hits} \geq 1$	$N_{hits} = 0$	
$P^{AND}_{hits/BX}$	$N_{hits} \geq 1$	$N_{hits} \geq 1$	event counting AND
$P^{OR}_{0/BX}$= 1-$P^{AND}_{hits/BX}$	$N_{hits} = 0$	$N_{hits} = 0$	zero counting OR
	$N_{hits} = 0$	$N_{hits} \geq 1$	
	$N_{hits} \geq 1$	$N_{hits} = 0$	
$P^{AND}_{0/BX} = 1 - P^{OR}_{hits/BX}$	$N_{hits} = 0$	$N_{hits} = 0$	zero counting AND
$N^{OR}_{hits/BX}$	$N_{hits} \geq 1$	$N_{hits} \geq 1$	hit counting OR
	$N_{hits} = 0$	$N_{hits} \geq 1$	
	$N_{hits} \geq 0$	$N_{hits} = 0$	
$N^{AND}_{hits/BX}$	$N_{hits} \geq 1$	$N_{hits} \geq 1$	hit counting AND

Table 5.1: Counting methods.

equation 5.1 that remains valid even when, because of different bunch currents and/or emittances, each bunch pair produces a different luminosity (reflecting a different value of μ):

$$L = \sum_{i \in BCID} \mu_i^{vis} \frac{f_r}{\sigma_{vis}} \tag{5.4}$$

where the sum is performed over the colliding BCIDs.
The value of μ_i^{vis} used to determine the bunch luminosity in equation 5.4 is obtained from the raw number of counts N_i and the number of bunch crossing N_{BC}, using an algorithm-dependent expression, and under the assumptions that:

- the number of *pp* interactions occurring in any bunch crossing obeys a Poisson distribution. This assumption drives the combinatorial formalism described below.

- the efficiency to detect a single inelastic *pp* interaction is constant, in the sense that it does not change when several ineractions occurr during the same bunch crossing. This is tantamount to assuming that the efficiency ϵ_n for detecting one event containing n interactions in the same crossing is given by $\epsilon_n = 1 - (1 - \epsilon_1)^n$ where ϵ_1 is the detection efficiency corresponding to a single inelastic interaction in a bunch crossing. The same definitions are valid for the efficiency ϵ^{OR}, ϵ^{A}, ϵ^{C} and ϵ^{AND} used below.

For all the described methods, the relationship between the number of hits or events counted by LUCID and the value of μ exhibits non-linearities at large μ due to migration effect. Corrections for such non-linearities depend on the efficiency for an inelastic event to pass the specified selection criteria. The form of the corrections is different for algorithms that require a single hit with respect to those that require a coincidence between both sides of the detector.

Event OR algorithm

In the Event OR case, the logic to evaluate μ from N_i is quite simple. Since the Poisson probability for observing zero events in a bunch crossing is

$$P_0(\mu^{vis}) = e^{-\mu^{vis}} = e^{-\mu\epsilon^{OR}} \tag{5.5}$$

the probability of observing at least one event is:

$$P_{Event-OR}(\mu^{vis}) = \frac{N_{OR}}{N_{BC}} = 1 - P_0(\mu^{vis}) = 1 - e^{-\mu^{vis}} \tag{5.6}$$

The raw event count N_{OR} is the number of bunch crossing, during a given time, in which at least one *pp* interaction satisfies the event-selection criteria of the Event-OR algorithm, and N_{BC} is the total number of bunch crossings during the same interval. Equation 5.6 reduces to intuitive result $P_{Event-OR}(\mu^{vis}) \sim \mu^{vis}$ when $\mu^{vis} << 1$. Solving for μ^{vis} in term of event-counting rate yields:

$$\mu^{vis} = -ln\left(1 - \frac{N_{OR}}{N_{BC}}\right) \tag{5.7}$$

Event AND algorithm

For methods requiring a coincidence between sides, the formula is more complicated, since the probability in this case depends on three exponentials and three parameters: the probability of detecting an interaction on side A, ϵ_A, the probability of detecting an interaction on side C, ϵ_C, and the probability of detecting a coincidence between the two sides, ϵ^{AND}. These efficiencies are related to the Event OR efficiency by $\epsilon^{OR} = \epsilon^A + \epsilon^C - \epsilon^{AND}$.
The probability $P_{Event-AND}(\mu)$ of there being at least one hit on both side is one minus the probability $P_0^{Zero-OR}$ of there being no hit on at least one side. The latter, in turn, equals the probability that there be no hit on at least side A, $P_{0A} = e^{-\mu\epsilon^A}$, plus the probability that there be no hit on at least side C,

$P_{0C} = e^{-\mu\epsilon^C}$, minus the probability that there be no hit on either side, $P_0 = e^{-\mu\epsilon^{OR}}$:

$$\begin{aligned} P_{Event-AND} = \frac{N_{AND}}{N_{BC}} &= 1 - P_0^{Zero-OR}(\mu) = \\ &= 1 - (e^{-\mu\epsilon^A} + e^{-\mu\epsilon^C} - e^{-\mu\epsilon^{OR}}) = \\ &= 1 - (e^{-\mu\epsilon^A} + e^{-\mu\epsilon^C} - e^{-\mu(\epsilon^A+\epsilon^C-\epsilon^{AND})}) \end{aligned} \tag{5.8}$$

The final expression can not be inverted analytically. The most appropriate functional form depends on the values of ϵ^A, ϵ^C and ϵ^{AND}. The above equation can be simplified using the fact that $\epsilon^{AND} << \epsilon^{A,C}$ and assuming that $\epsilon^A \sim \epsilon^C$. The efficiencies ϵ^{AND} and ϵ^{OR} are defined by respectively $\epsilon^{AND} = \sigma_{vis}^{AND}/\sigma_{inel}$ and $\epsilon^{OR} = \sigma_{vis}^{OR}/\sigma_{inel}$. The average number of visible inelastic interactions per BC is computed as $\mu^{vis} = \epsilon_{AND}\mu$. Equation 5.8 becomes:

$$\begin{aligned} \frac{N_{AND}}{N_{BC}} &= 1 - 2e^{-\mu(\epsilon^{AND}+\epsilon^{OR})/2} + e^{-\mu\epsilon^{OR}} = \\ &= 1 - 2e^{-(1+\sigma_{vis}^{OR}/\sigma_{vis}^{AND})\mu^{vis}/2} + e^{-(\sigma_{vis}^{OR}/\sigma_{vis}^{AND})/\mu^{vis}} \end{aligned} \tag{5.9}$$

Equation above is then solved numerically.

Pile-up-related Instrumental Effects

The μ-dependency of the probability functions for the Event AND and the Event OR algorithms is displayed in figure 5.2. The algorithms saturate at high μ, reflecting the fact that as the migration increase, the probability of observing at least one event per bunch crossing approaches one. Any event counting luminosity algorithm will therefore loose precision and ultimately become unusable, as the LHC luminosity per bunch increases far beyond the level reaches in 2010. The tolerable pile-up level is detector- and algorithm- dependent: the higher the efficiency, the earlier the onset of the saturation.

The accuracy of the event counting formalism can be verified using simulated data. The Monte Carlo data used here are not corrected for the scale and smearing factors, but, for the event counting methods, the efficiency does not differ using the corrected or uncorrected Monte Carlo predictions. Figure 5.2 (bottom) shows that the parametrizations used for the event algorithms deviate from the full simulation by ±2% at most: possible instrumental effects not accounted for by the combinatorial formalism are predicted to have negligible impact for the bunch luminosities achieved in 2010 LHC run ($0 < \mu < 5$). For all the 2010 running, the event counting algorithms were considered the preferred ones.

It should by stressed, however, that the agreement between the Poissonian formalism and the full simulation depends critically on the validity of the assumption that the efficiency for detecting an inelastic *pp* interaction is indipendent of the number of interactions that occur in each crossing. This requires, for instance, that the threshold for registering a hit in a PMT (nominally 15 photoelectrons) be low enough compared to the average single-particle response. This condition is satisfied by the simulation shown in figure 5.2. repeating this simulation with the threshold raised to 50 photoelectrons yields systematic discrepancies as large as 7% between the computed and the simulated probability functions for the Event AND algorithm. When the threshold is too high, a particle from a single *pp* interaction occasionally fails to fire the CFD threshold. But should two such particles produce enough light to register a hit. This is the migration effect.

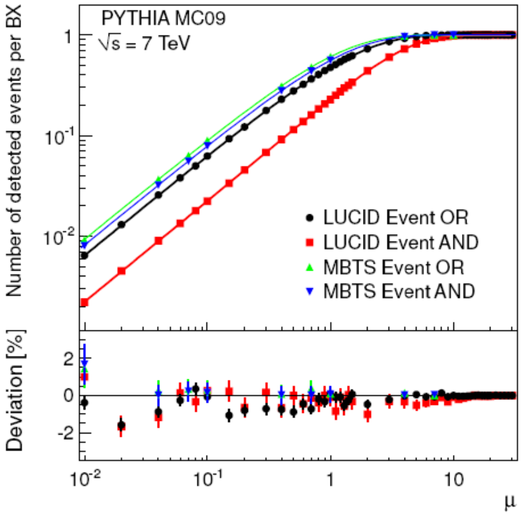

Figure 5.2: Event counting probability per bunch crossing for LUCID and MBTS algorithms as a function of μ, the true average number of inelastic *pp* interactions per BC. The symbols are the result of a Monte Carlo study performed using the PYTHIA event generator together with a GEANT4 simulation of the ATLAS detector response. The curves reflect the combinatorial formalism desbribed in the text using as input only the visible cross sections extracted from the same simulation. The bottom insert shows the difference between the full simulation and parametrization.

Hit counting algorithm

Converting measured hit-counting probabilities into instantaneous luminosity proved significantly more delicate than for event-counting algorithms expecialy due to non-linearity of the hit counting method at high μ. The calibration and the performance of the hit counting algorithm require more extensive studies. The hit

counting algorithms are not used at present for the online luminosity evaluation and will be no longer used in following analysis. Further studies are ungoing and the implementation of the hit counting methods for luminosity monitor will be done once the μ value will rise up to more than ten, case in which the event counting algorithms will be no more usable due to saturation.
A full description of the analytic way to find the expression of μ from the number of hits both for zero/event and hit counting methods are presented in appendix A and B.

5.3 Luminosity Determination using Calibration from Monte Carlo Simulation

Before using real data, the luminosity calibration has been evaluated by using Monte Carlo predictions. In this section the relevant results about the efficiencies and the systematic errors obtained with Monte Carlo predictions are presented.
Luminosity measurements were normalized to the inclusive, inelastic *pp* cross section, with simulated data used to determine the event/zero counting and/or the hit counting efficiencies. The luminosity is then calculated as:

$$L = \frac{\mu^{meas} n_b f_r}{\sigma_{vis}} = \frac{\mu^{meas} n_b f_r}{\epsilon_{ND}\sigma_{ND} + \epsilon_{SD}\sigma_{SD} + \epsilon_{DD}\sigma_{DD}} \tag{5.10}$$

where $\epsilon_{process}$ is the efficiency and $\sigma_{process}$ the cross section for non-diffractive (ND), single-diffractive (SD) and double-diffractive (DD) processes. The *pp* cross section at both 900 GeV and 7 TeV have not been measured yet. Only extrapolation of cross section to high energy predictions are available. Results on this extrapolation depend on the functional form used in the generators. Moreover, the generators must separately model the non-diffractive, single-diffractive and double-diffractive components of the cross section. There exist no unique prescription for classifying events as diffractive or non-diffractive and no calculation of the cross section from first principles. As a consequence, Monte Carlo based calibration of the absolute luminosity that relies on the modeling of the inelastic cross section will incur in a significant systematic uncertainty. This uncertainty in such extrapolations has been evaluated comparing the cross sections and acceptances predicted by two Monte Carlo generators: PHYTIA and PHOJET. Table 5.2 shows the PYTHIA and PHOJET predictions for the inelastic cross section at both $\sqrt{s} = 900$ GeV and $\sqrt{s} = 7$ TeV. The predicted cross sections in PHOJET are higher than PYTHIA by 3% at 900 GeV and 6.5% at 7 TeV. The fraction of σ_{inel} corresponding to ND events is 68% in PYTHIA and 81% in PHOJET, while the DD fractions are 13% in PYTHIA and 5% in PHOJET. Finally there are significant uncertainties on the modeling of the predicted multiplicity- , p_T- and η- distributions for particles produced in soft pp interactions, particularly for the poorly constrained diffractive components. [17]

	900 GeV	
Process	**PYTHIA**	**PHOJET**
ND	34.4	40.0
SD	11.7	10.5
DD	6.4	3.5
Total:	52.5	54.0

	7 TeV	
Process	**PYTHIA**	**PHOJET**
ND	48.5	61.6
SD	13.7	10.7
DD	9.3	3.9
Total:	71.5	76.2

Table 5.2: Predicted inelastic pp cross sections in mb for $\sqrt{s}$ = 900 GeV (left) and $\sqrt{s}$ = 7 TeV (right) for PYTHIA and PHOJET.

Event AND	$\sqrt{s}$ = *7 TeV*	
Process	**PYTHIA**	**PHOJET**
ND	30.8	25.5
SD	1.2	2.4
DD	4.4	14.8
σ_{vis}	15.5	16.4

Event OR	$\sqrt{s}$ = *7 TeV*	
Process	**PYTHIA**	**PHOJET**
ND	79.2	74.2
SD	28.7	44.8
DD	39.4	62.0
σ_{vis} (mb)	46.1	52.9

Table 5.3: Efficiencies at $\sqrt{s} = 7$ TeV for the luminosity algorithms used in 2010. The σ_{vis} is obtained using these acceptances and the cross sections from table 5.2. No number can be given for $\sqrt{s} = 900$ GeV because the low average hit multiplicity at this energy made it difficult to calculate the efficiency with an uncertainty of less than 30%.

Table 5.3 shows the predicted efficiencies for observing ND, SD and DD events using either PYTHIA or PHOJET. In general, for all the algorithms used by the luminosity monitors, the PHOJET predictions are about 15% to 20% higher than those obtained with PHYTIA. One exception is the LUCID Event AND algorithm

which is less sensitive to the diffractive processes: here the two generators agree to within 5% overall. Additional systematic uncertainties on these predictions, associated with the modelling of the detector response in the simulation, are algorithm- and trigger- dependent and are at about 6% level.
Final systematic uncertainties at 7 TeV center-of-mass energy for each of the methods used to determine the absolute luminosity in 2010 are about 20%.

5.4 Luminosity Monitoring with LUCID during 2010 data taking

During all 2010 data taking, LUCID was the preferred luminosity monitor and provided online luminosity measurements.
The event counting algorithms have been the preferred ones for all the period of data taking due to two main reasons: first the maximum μ value was of 4.5, smaller than the value that saturate the event counting algortihm; second further studies are ongoing to better understand the hit counting algorithms. The hit counting methods will be necessary when the luminosity will increase and the event counting methods will be no usable any longer. As long as the background is small, the event OR counting is usually preferable to the event AND since it gives a smaller statistical uncertainty and has a less complicated dependence on the number of interactions per bunch crossing, as presented in previous section. Before the start of LHC, the level of expected background was an open question. It was later demonstrated that the background for the Event AND is neglegible and it is also small for the Event OR counting, both at 900 GeV and at 7 TeV, as long as one retains only the counts from the filled bunches colliding at the ATLAS interaction point. The background was evaluated using counts from the so-called unpaired bunches, filled bunches not colliding in ATLAS, in order to account for beam-related effects as beam-halo or beam-gas. The number of events in the unpaired bunches was counted and scaled, taking into account the ratio of paired to unpaired bunches and their currents. Results of this study for a typical run at 7 TeV are shown in figure 5.3. The background is typically 10^{-4} for the event OR counting and less than 10^{-5} for the event AND counting. Contributions from other sources of background such as cosmic rays and electronic noise have been measured in absence of beam and are negligible when selecting only the colliding BCIDs.

Typical luminosity histograms available online and used during data taking to control the luminosity measurements are presented in figure 5.4. The plots refer to an ATLAS run taken in August 2010, with an average μ value of 1.74 and 35 filled bunches. The main features of this run are listed in table 5.4. In both his-

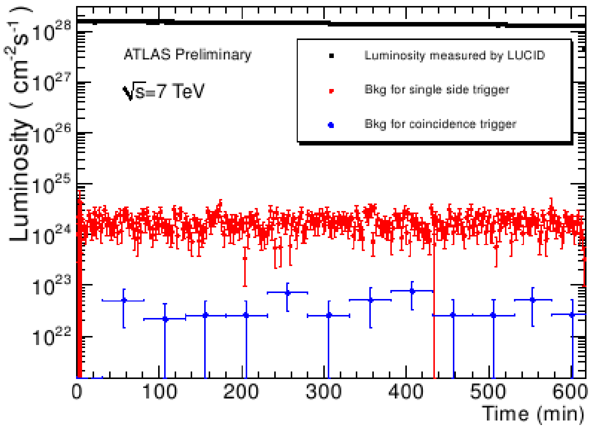

Figure 5.3: The luminosity measured at 7 TeV for one LHC fill obtained from paired bunches is displayed together with the background level for the single side event OR and for the coincidence event AND algorithm. The background is calculated from the unpaired bunches.

tograms, the instantaneous luminosity is calculated bunch by bunch for each LB, which permits to control the bunch structure: the highest peaks correspond to the colliding bunches, while the smallest peaks both in OR and in AND algorithms corrspond to unpaired bunches. The coincidence logic permits to strongly suppress the background.

Peak luminosity	9.6 $\times 10^{30} cm^{-2} s^{-1}$
Peak μ	1.74
Approx lifetime	21 h
No. of colliding bunches	35
Beam 1 intensity	34.9 $\cdot 10^{11}$ protons
Beam 2 intensity	35.0 $\cdot 10^{11}$ protons
Maximun beam energy	3500 GeV

Table 5.4: Main features of the run used to display the examples of the online histograms.

The total luminosity recorded during the run is inferred from figure 5.5, that presents the online histogram for integrated luminosity in case of event AND algorithm. An analogous histogram is available during data taking for OR algorithm. The total integrated luminosity is calculated summing up the counts bunch by bunch over all the LB. For the LUCID event AND algorithm, the total integrated

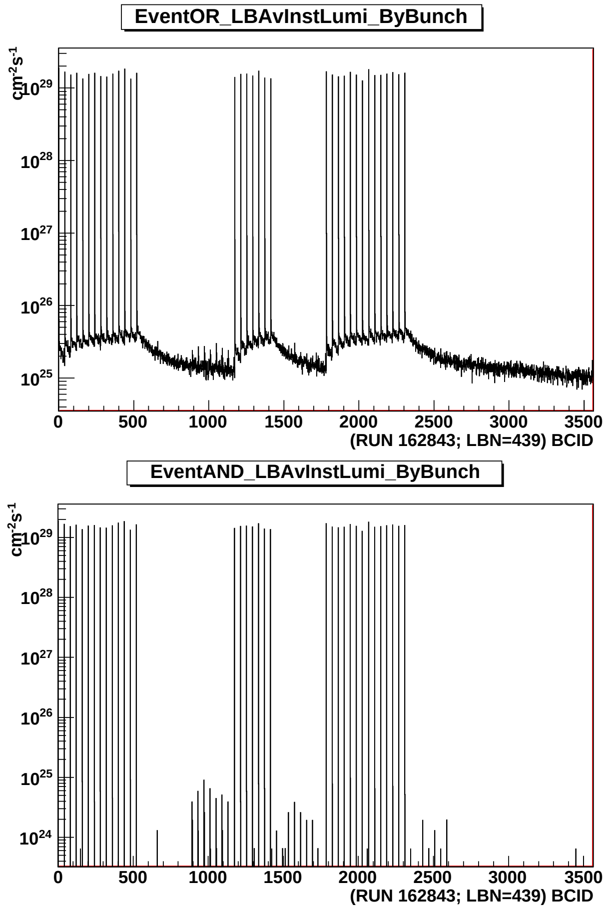

Figure 5.4: Average instantaneous bunch by bunch luminosity for a typical run evaluated with Event OR (top) and Event AND (bottom) algorithms.

luminosity for this particular run is 339.1 nb^{-1}.

The degradation of the beams is visible from the exponential decay of the instantaneous luminosity of figure 5.6. In this case the luminosity bunch by bunch provided by the Event AND algorithm is summed up over a single LB and the result is reported for each LB.

To control the robustness of the algorithms, the ratio between the luminosity obtained from the Event AND and the Event OR algorithms is performed for each run. Figure 5.7 shows this ratio for a typical run. The ratio between the two algorithms is flat within 0.5% for variations of the luminosity of about 40%.

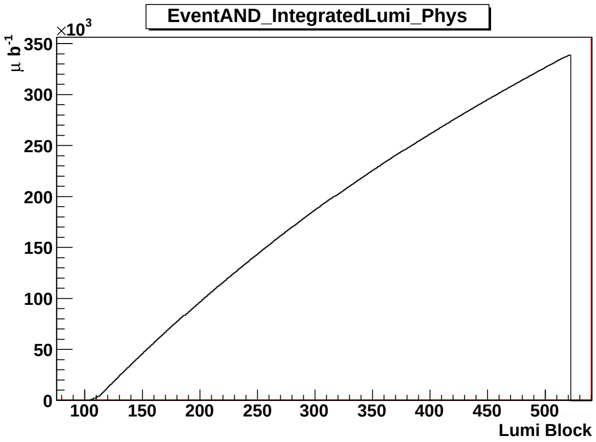

Figure 5.5: Integrated luminosity evaluated using the counts of the LUCID Event AND algorithm for a typical run summed up on all the BCID and LB.

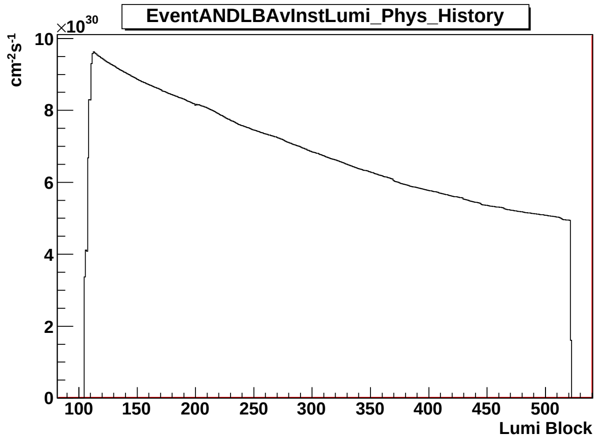

Figure 5.6: Instantaneous luminosity obtained from the Event AND algorithm summing up the counts bunch by bunch in a single LB. The results are presented for each LB. The beam degradation is well visible from the exponential decay of the luminosity.

5.4.1 Comparison between LUCID and other Luminosity Monitors

To control the validity of the algorithms used by the different detectors to calculate the luminosity, the comparison bewteen the measurements done by the different luminosity monitors is studied.

The instantaneous luminosities determined using three independent methods for a run taken on December 12, 2009 at center-of-mass energy of 900 GeV have been compared. The plot in figure 5.8 shows the performances of LAr (blu) and LUCID

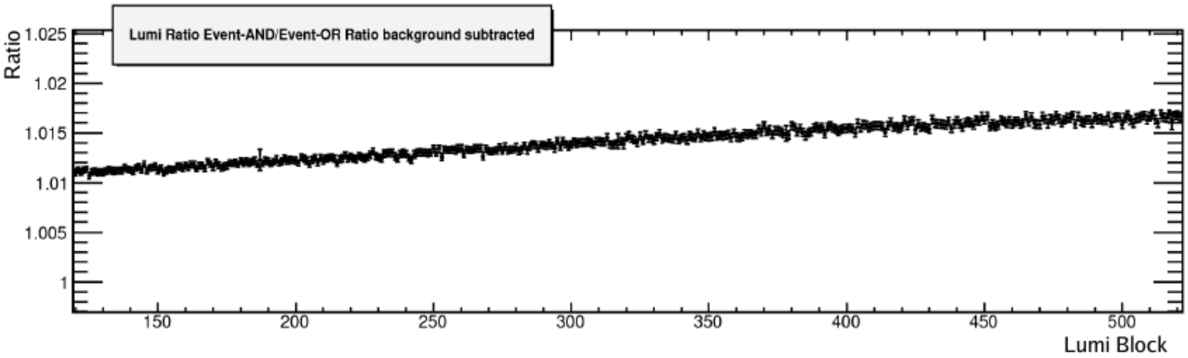

Figure 5.7: Ratio between the luminosity obtained from the Event AND and the Event OR algorithms, background subtracted. The ratio between the two algorithms is flat within 0.5% for variations of the luminosity of about 40%.

event OR (red) normalized at the MBTS results (yellow).

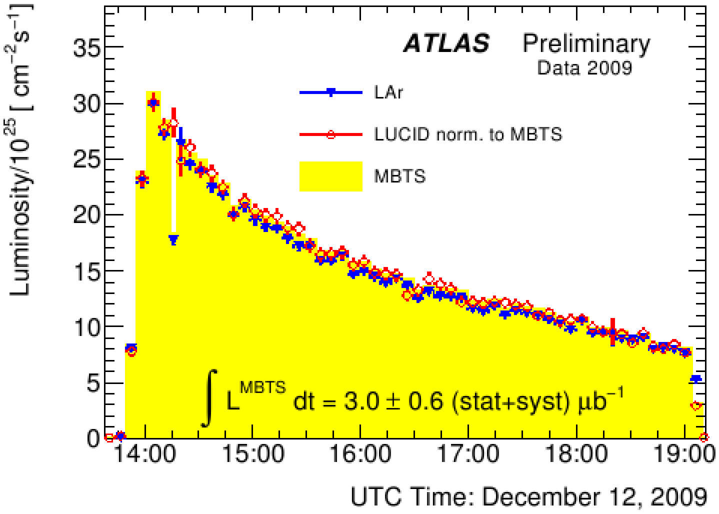

Figure 5.8: Instantaneous luminosity determined using three indipendent methods for a run taken on December 12, 2009 at center-of-mass energy of 900 GeV. The plot shows the performances of LAr (blu) and LUCID event OR (red) normalized at the MBTS results (yellow).

Figure 5.9 showns the same comparison for a typical run taken at 7 TeV. The ATLAS instantaneous luminosity as determined by LAr (blue open circles), LUCID (open squares), using Event OR algorithm, and MBTS (red triangles) for an ATLAS typical run is presented in the top plot of figure 5.9. The instantaneous luminosity provided by LAr and by LUCID normalized to the luminosity obtained using the MBTS detector is reported in the bottom plot of figure 5.9. In both cases, the LAr instantaneous luminosity is corrected for the dead-time in the data acquisition system, since it evaluate the recorded luminosity using quantities available from the offline analysis of the ATLAS data stream. Neither the MBTS nor the LUCID methods are affected by data-acquisition dead-time, since they are designed to measure the delivered luminosity. For each of the luminosity measurements, the acceptance is indipendently calculated using the PYTHIA Monte Carlo simulation of the *pp* inelastic interactions, as described in details for LUCID case in section 5.3. The agreement between the measurements of the luminosity with the different subdetectors is satisfactory.

5.5 Conclusions

In 2010, only the LUCID detector was operational to provide luminosity evaluation during all the full LHC running. Different algorithms were implemented in the LUCID electronics to measure the luminosity: event counting and hit counting algorithms. For each algorithm, LUCID was able to provide a luminosity measurement BCID per BCID per LB. Moreover, LUCID communicated to the LHC a luminosity evaluation at a frequancy of 1-2 Hz for the online monitor of the machine.

The luminosity measurements during all 2010 performed by various monitors have been in agreement within the different algorithms and within the different luminosity monitors.

Before the start of LHC, the calibration of LUCID algorithms was provided by the predictions of Monte Carlo simulation. The uncertainty on the Monte Carlo based calibration is of about 20%, precision that has been improved with the Van der Meer scan results as described in more details in chapter 6. The use of physics processes, as described in chapter 7, will start to play an important role in the future.

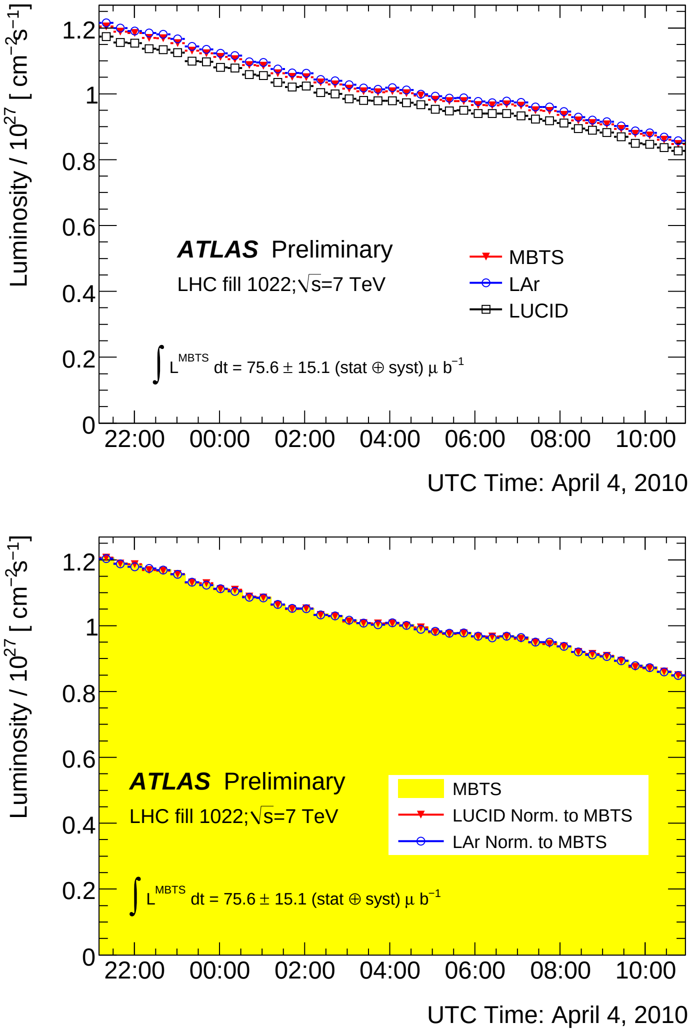

Figure 5.9: Top: the ATLAS instantaneous luminosity as determined by LAr (blue open circles), LUCID Event OR (open squares) and MBTS (red triangles) algorithms for an ATLAS run. Bottom: the instantaneous luminosity as determined by LAr (blue open circles) and the LUCID Event OR (open squares) normalized to the luminosity obtained using the MBTS (sheded area).

Chapter 6

Absolute Luminosity Determination with Van der Meer Scan Method

6.1 Introduction

Five Van der Meer luminosity scans have been performed at the ATLAS interaction point in 2010: on April 26 a single scan in both the horizontal and vertical planes, while on May 9 and October 11 two successive scans in both planes. In this chapter only the results of the analysis on the first three scans are presented. The analysis on the last two scans is still ongoing. The results of the analysis on the data of the first three scan were able to provide the uncertainty on the calibration constant for the absolute luminosity at 11% level. Including the data of the last scans, the uncertainty on the calibration constant reaches a 3.4% level [37].
The method used to measure the machine peak luminosity as well as the results of the analysis on beam-separation scan data are here reported.

6.2 Measurement of Luminosity in a Van der Meer Scan

In terms of colliding beam parameters, the luminosity can be defined as:

$$L = \frac{n_b f_r I_1 I_2}{2\pi \Sigma_x \Sigma_y} \tag{6.1}$$

where Σ_x is defined by the equation:

$$\Sigma_x = \frac{1}{\sqrt{2\pi}} \frac{\int R_x(\delta) d\delta}{R_x(0)} \tag{6.2}$$

In this case $R_x(\delta)$ is the luminosity (or equivalent μ), in arbitrary units, measured during a horizontal scan at the time the two beams are separated by the distance δ. $\delta = 0$ represents the case of zero beam separation. The Eq. 6.1 is the general formula to extract luminosity from machine parameters by performing a beam separation scan. This formula is quite general and does not depend upon the shape of the experimental rate distribution versus beam separation (although it does depend on the assumption that there is no correlation between particle density distribution in x and in y). More details about the method to calculate the luminosity from a Van der Meer scan are reported in chapter 2.

6.3 Beam Scan Data Sets

On April 26 2010 a single scan in both the horizontal and vertical planes was performed, while on May 9 2010 two successive scans in both planes were performed. A pictorial schema of the procedure is shown in figure 6.1.

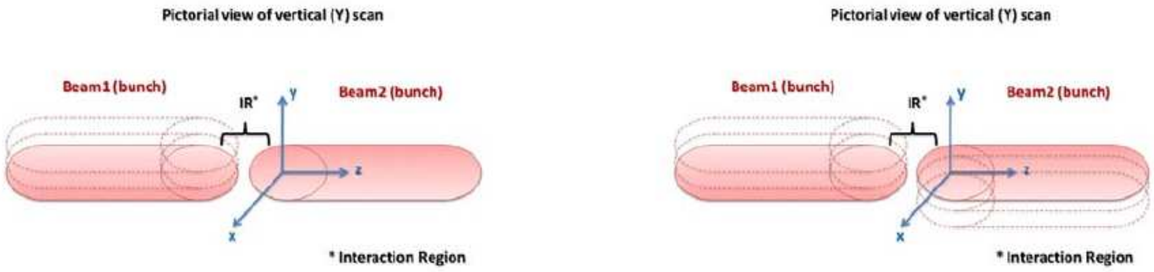

Figure 6.1: Pictorial demonstration of the vertical scan (scan-y). The left plot shows beam 1 moves with respect to beam 2 while the right plot shows both beams moving with respect to each other.

The procedure for the beam scans [38] [39] ran as follows. After centering the beams on each other at the IP a full-fledged luminosity calibration scan was carried out in the horizontal plane, spanning a range of $\pm 6\sigma_b$ in horizontal beam separation, where σ_b is the nominal transverse size of either beam at the IP. For Scan I, the relative transverse centering of the two beams was then verified using a miniscan in the horizontal plane and was found to be satisfactory. No such check was performed in the vertical plane. In the next step a full-fledged luminosity calibration scan was carried out in the vertical plane, again spanning a range of $\pm 6\sigma_b$ in relative beam separation.

The mini-scans used to first center the beams on each other in the transverse plane are done by activating closed orbit bumps around the IP that vary the IP positions of both beams by $\pm 1\sigma_b$ in opposite directions, either horizontally or vertically. The relative positions of the two beams are then adjusted, in each plane, to achieve (at that time) optimum transverse overlap. A closed orbit bump is a local distortion of the beam orbit that is implemented using pairs of steering dipoles located on either side of the affected region. In this particular case, these bumps are tuned to translate either beam parallel to itself at the IP, in either the horizontal or the vertical direction. The full-fledged horizontal and vertical scans follow an identical procedure, where the same orbit bumps are used to displace the two beams in opposite directions by $\pm 3\sigma_b$, resulting in a total variation of $\pm 6\sigma_b$ in relative displacement at the IP. This procedure is illustrated in figure 6.2: the time-history of the relative horizontal separation separation of beam 1 and 2, called *nominal separation*, is displayed. In Scan I, the horizontal scan started at zero nominal separation, moved to the maximum separation in the negative direction, stepped back to zero and on to the maximum positive separation, and finally returned to the original settings of the closed-orbit bumps (zero nominal separation). The same procedure was followed for the vertical scan. In Scan II and III, after collision optimization with the transverse miniscans, a full-fledged horizontal scan was taken from negative to positive nominal separation, followed by a hysteresis cycle where the horizontal nominal separation was run to -$6\sigma_b$, then 0 then +$6\sigma_b$, and finally followed by a full-fledged horizontal scan in the opposite direction to check for potential hysteresis effects. The same procedure was then repeated in the vertical direction.

For each scan, at each of the 27 steps in relative displacement, the beams were left in a quiescent state for about 30 seconds, during which the relative luminosity measured by all active ATLAS luminosity monitors (LUCID, BCM, MBTS and ZDC) was recorded as a function of time in a special purpose data stream.

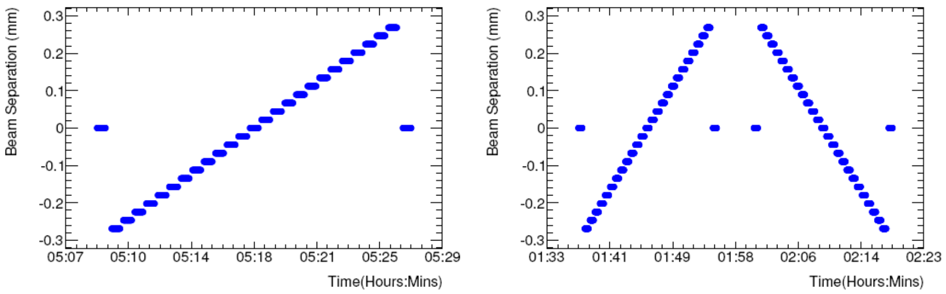

Figure 6.2: Scanning sequence for full-fledged luminosity-calibration scans in the horizontal plane. Left: time-history of the horizontal nominal separation reported by the LHC control system during the VdM-I scan (26 April 2010). Right: same for the VdM-II and VdM-III scans (9 May 2010). The x axis is Geneva local time.

The value of the nominal separation, the beam currents and other relevant accelerator parameters transmitted to ATLAS by the accelerator control system were recorded as well. In addition, the full ATLAS data acquisition system was operational throughout the scan, using the standard ATLAS trigger, and triggered events were recorded as part of the normal data collection.

The full history of the raw luminosity is illustrated in figure 6.3 (left). The luminosity was sampled every 1 to 2 seconds depending on the subdetector, and is displayed here irrespective of whether the IP beam positions were left in the quiescent state (as required for valid luminosity measurements) or being adjusted between steps. Eliminating the samples corresponding to the non-quiescent states of the closed-orbit bumps, and averaging over the quiescent scan steps, yields the raw instantaneous luminosity over quiescent pseudo-luminosity blocks displayed in figure 6.3 (right). Unless specifically stated otherwise, only the data points corresponding to steps 2 to 26 (figure 6.3 top), or 2 to 26 and 29 to 53 (figure 6.3 bottom), are retained in the analysis presented in the following sections.

Variations of the number of protons per bunch during the beam scans were almost negligible. Changes of beam emittance resulting in variations of luminosity of a few percent have been observed. The systematic uncertainty associated with this effect is discussed in section 6.3.3. The main characteristics of the three scans are summarized in table 6.1.

6.3.1 Parametrization and Analysis of Beam Scan Data

Data from all the first three scans have been analyzed both from the dedicated data stream and from the standard ATLAS data stream. Analysis using the standard ATLAS data stream suffers from reduced statistical precision relative to the dedicated stream, but allows for important cross-checks both of the background and of the size and position of the luminous region. In addition, because this stream contains full ATLAS events, these data can be used to measure the visible cross section corresponding to standard analysis selection. Measurements performed using these two streams provide a consistent interpretation of the data within the relevant statistical and systematic uncertainties.

In all cases, the analysis fits the rate distributions as a function of beam separation to find Σ_x and Σ_y defined in equation 6.2. These results are then combined with a measurement of the beam intensities to determine the luminosity by equation 6.1. To remove sensitivity to beam lifetime effects which cause a decrease in beam current with time, the data are analyzed as *specific rates* R_{sp}, obtained by dividing the measured rate by the product of beam curents measured at that scan point:

$$R_{sp} = \frac{(I_1 I_2)_{max}}{(I_1 I_2)_{meas}}(R_{meas}) \tag{6.3}$$

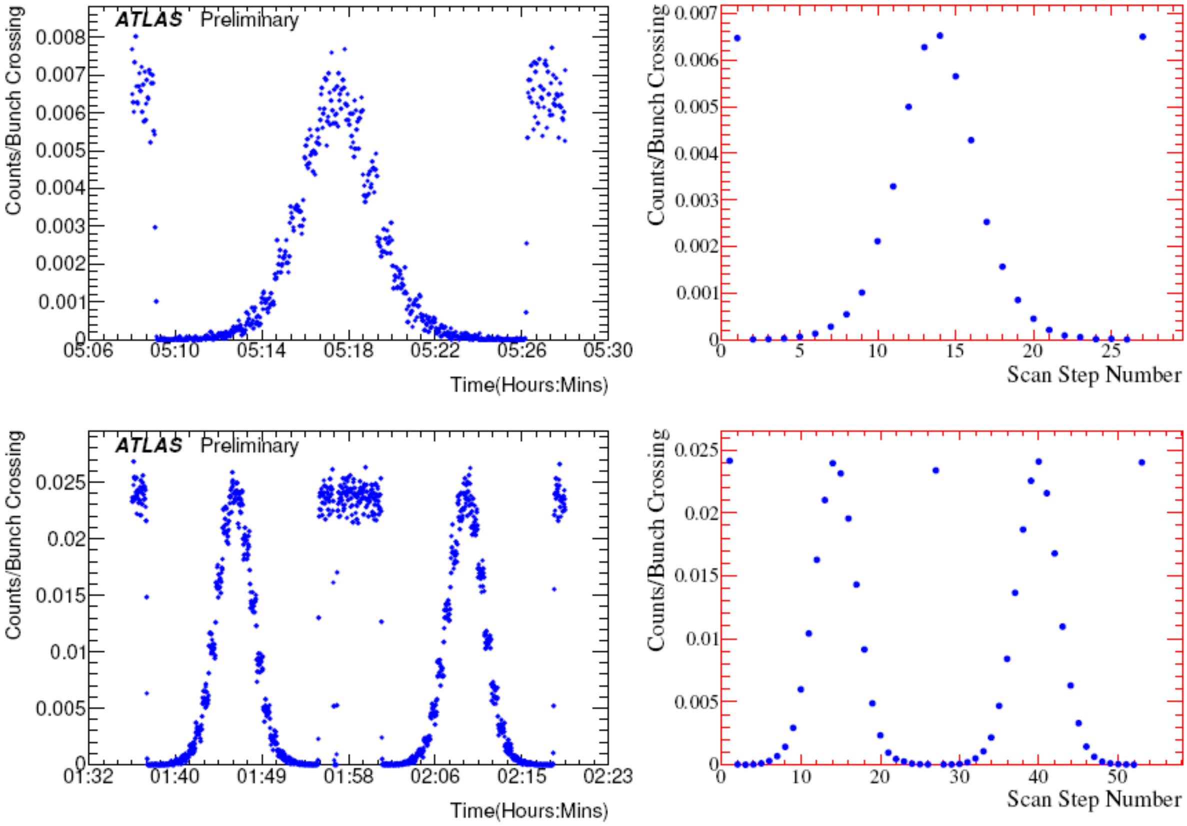

Figure 6.3: History of the raw luminosity, in units of events per bunch crossing, from the LUCID event AND algorithm during the full-fledged horizontal-calibration scan. Top: VdM-I scan (26 April 2010). Bottom: VdM-II and VdM-III scans (9 May 2010). Left: time-history of the sampled luminosity, irrespective of whether the transverse IP positions of the two beams were left in a quiescent state. Right: raw instantaneous luminosity average over the pseudo-luminosity blocks (or scan steps), where the IP positions were left unchanged. All steps are equal in duration. The points in steps 1 and 27 (top) and in steps 1, 28 and 54 (bottom) correspond to close-orbit bumps settings to zero nominal separation in both planes.

Actions	*VdM Scan - I* (April 26, 2010)	*VdM Scan - II, III* (May 9, 2010)
Scan directions	1 horizontal scan followed by 1 vertical scan	2 horizontal scans followed by 2 vertical scans
Total Scan Step/per plane	27 ($\pm 6\sigma$)	54 (27+27) ($\pm 6\sigma$)
Scan Duration/scan step	30 sec	30 sec
# of bunches colliding in ATLAS	1	1
Total # of bunches per beam	2	2
# of protons per colliding bunch	$0.09 \cdot 10^{11}$	$0.2 \cdot 10^{11}$
β^* (m)	~2	~2
σ_b (μm)	~45	~45
Crossing angle (μrad)	0	0
Typical luminosity/bunch (μb^{-1})	$4.5 \cdot 10^{-3}$	$1.8 \cdot 10^{-2}$
μ (interactions/crossing)	0.03	0.11
Detectors included	LUCID, MBTS, BCM ZDC, Inner Detector	LUCID, MBTS, BCM, ZDC, Inner Detector

Table 6.1: Summary of the main characteristics of the three beam scans performed in the ATLAS interaction point.

whre $(I_1 I_2)_{meas}$ is the value of the product of the number of protons in the two colliding bunches during the measurement, $(I_1 I_2)_{max}$ is their maximum value during the scans (see table 6.1), R_{meas} is the value of μ^{vis} at the current scan point. Beam currents are measured using two complementary LHC system: the *Fast Bunch-Current Transformers (FBCT)* and the *Direct-Current Current Transformers (DCCT)* described in cahpter 1 section 1.2.5.

Fits to the rate distribution require a choice of parametrization of the shape of scan distribution. For all algorithms, only fits using a double Gaussian with commom mean plus a flat background result in acceptable χ^2 values. In general, the background rates are consistent with zero for the algorithms requiring a coincidence between sides, while small but statistically significant backgrounds are observed for algorithms requiring only a single side. These backgrounds are reduced to less than 0.3% of the luminosity at zero beam separation by using data from the colliding bunches only. The residual is removed using the rate measured in the unpaired bunches (filled bunches not colliding at the ATLAS interaction point). No background term is therefore needed in the fit function. Examples of such fits are shown in figure 6.4, for the LUCID Event OR algorithm, for the second luminosity scan.

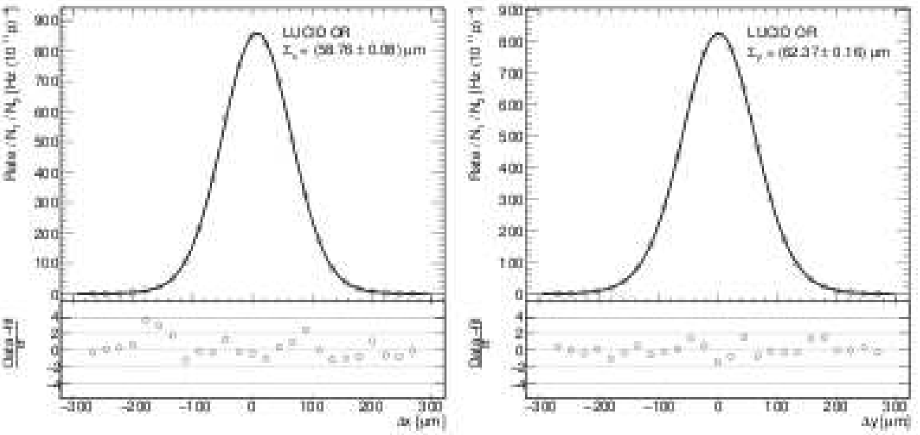

Figure 6.4: Results of fits to the second luminosity scan in the x (left) and y (right) direction for the LUCID Event OR algorithm.

In the case where the specific rate is described by a double Gaussian (named a and b), the specific rate can be written as:

$$R_x(\delta) = R_x(x - x_0) = \frac{\int R_x(\delta)d\delta}{\sqrt{2\pi}} \left[\frac{f_a e^{-(x-x_0)^2/2\sigma_a^2}}{\sigma_a} + \frac{(1-f_a)e^{-(x-x_0)^2/2\sigma_b^2}}{\sigma_b} \right] \quad (6.4)$$

where σ_a and σ_b are the widths of first and second Gaussians respectively, f_a is the fraction of the rate in the first Gaussian and x_0 is introduced to allow the possibility that the beams are not perfectly centered at the time of the scan. The value of Σ_x in equation 6.1 becomes:

$$\frac{1}{\Sigma_x} = \left[\frac{f_a}{\sigma_a} + \frac{1-f_a}{\sigma_b} \right] \quad (6.5)$$

6.3.2 Fit Results

A summary of the relevant fit parameters for the three beam scans is presented in table 6.2 for the LUCID event AND and OR algorithms.

Because the emittance during scan I was different from that during scan II and III, the values of Σ_x and Σ_y are not expected to be the same for the first and the later scans. Examination of this table indicates that the results for the mean position and for Σ for a given scan are consistent within statistical uncertainties between algorithms. These results also indicate several potential sources of systematic uncertainties. First, the fitted position of the peak luminosity deviates from zero by as much as 7 μm, indicating that the beams may not have been properly centered

Algorithm	**Mean Position (μm)**	Σ **(μm)**	**Bkc (Hz)**	R_{max} **(Hz)**	χ^2/dof
Horizontal scan I					
Event AND	-1.12 ± 0.46	47.40 ± 0.56	0.01 ± 0.04	75.6 ± 1.1	0.9
Event OR	-1.58 ± 0.25	47.27 ± 0.29	0.06 ± 0.04	247.8 ± 2.0	0.5
Vertical scan I					
Event AND	-5.04 ± 0.50	55.52 ± 0.59	0.05 ± 0.03	75.8 ± 1.0	0.8
Event OR	-5.23 ± 0.28	55.28 ± 0.33	0.16 ± 0.06	246.2 ± 1.9	1.1
Horizontal scan II					
Event AND	7.65 ± 0.25	58.78 ± 0.16	-0.02 ± 0.06	265.4 ± 3.0	1.8
Event OR	7.41 ± 0.14	58.76 ± 0.08	0.07 ± 0.12	858.9 ± 2.5	2.0
Vertical scan II					
Event AND	1.99 ± 0.27	62.75 ± 0.19	-0.21 ± 0.14	253.8 ± 2.9	1.6
Event OR	1.99 ± 0.16	62.37 ± 0.16	0.13 ± 0.13	825.3 ± 3.1	0.8
Horizontal scan III					
Event AND	5.48 ± 0.26	58.94 ± 0.19	0.04 ± 0.13	266.8 ± 3.0	1.2
Event OR	5.66 ± 0.15	58.57 ± 0.18	0.42 ± 0.10	856.8 ± 3.3	2.1
Vertical scan III					
Event AND	-0.01 ± 0.27	62.21 ± 0.30	-0.03 ± 0.08	259.9 ± 2.9	0.9
Event OR	0.08 ± 0.16	62.06 ± 0.16	0.23 ± 0.12	830.2 ± 3.1	0.8

Table 6.2: Summary of the relevant fit parameters for the three beam scans for LUCID event AND and OR algorithms.

before the start of the scan of about 1%. Second, in scan II and III, the peak luminosities for the horizontal and vertical scans, as measured with a single algorithm, show a systematic difference of as much as 5%, with a lower rate observed in the vertical scan. This systematic dependence may indicate a level of irreproducibility in the scan setup.

Calibration of the absolute luminosity from the beam scans uses the following expression for σ_{vis}:

$$\sigma_{vis} = \frac{R^{MAX}}{L^{MAX}} = R^{MAX} \frac{2\pi\Sigma_x\Sigma_y}{n_b f_r I_1 I_2} \tag{6.6}$$

where R^{MAX} and L^{MAX} are respectively the value of R_{sp} and the absolute luminosity (inferred from the measured machine parameters) when the beams collide exactly head-on. Since there are two indipendent measurements, one each for x and y directions, and each has the same statistical significance, the average of the two measurements is considered as the best estimate of R_{max}:

$$R^{max} = \frac{1}{2}(R_x^{max} + R_y^{max}) \tag{6.7}$$

The values of σ_{vis} for each method and each scan are reported in table 6.3.

Algorithm	*Scan number*	σ_{vis} *(mb)*	L_{spec} $(10^{29} cm^{-2} s^{-1})$
Event AND	I	12.15 ± 0.14	6.80 ± 0.08
	II	12.55 ± 0.10	4.85 ± 0.03
	III	12.73 ± 0.10	4.88 ± 0.03
Event OR	I	39.63 ± 0.32	6.85 ± 0.06
	II	40.70 ± 0.13	4.88 ± 0.01
	III	40.77 ± 0.14	4.92 ± 0.02

Table 6.3: Measurements of the visible cross section and peak specific luminosity for LUCID event AND and event OR algorithms for each beam scan. The uncertainties reported here are statistical only.

While the results of the second and the third luminosity scans are compatible within statistical uncertainties, those of the first luminosity scan are lower by 2.6-4.6%. These difference indicate possible systematic variation occurring between machine fills. Table 6.3 also reports the specific luminosity normalized to units of 10^{11} protons per bunch, called *specific luminosity.*

$$L_{spec} = \frac{Lc^2 10^{22} e^2}{I_1 I_2} = 10^{22} (p/bunch)^2 \frac{f_r}{2\pi \Sigma_x \Sigma_y} \tag{6.8}$$

Figure 6.5 shows the comparison of the specific luminosities obtained using various algorithms implemented in the different luminosity monitors for (a) scan II and (b) for scan III.

Because the emittance of scan 1 was difference from that of scans 2 and 3, the specific luminosity is not expected to be the same. The agreement between the algorithms within one scan is excellent. This agreement demonstrated that the variations in the measured value of σ_{vis}, with scan number for a given algorithm is due to the variation in the fitted rate R^{max} rather than in the values obtained for Σ.

6.3.3 Systematic Uncertainties

Systematic uncertainties affecting the luminosity and visible cross section measurements arise from the following effects: systematic errors affecting the measurement of absolute bunch charge, errors on the lengh scale calibration of beam

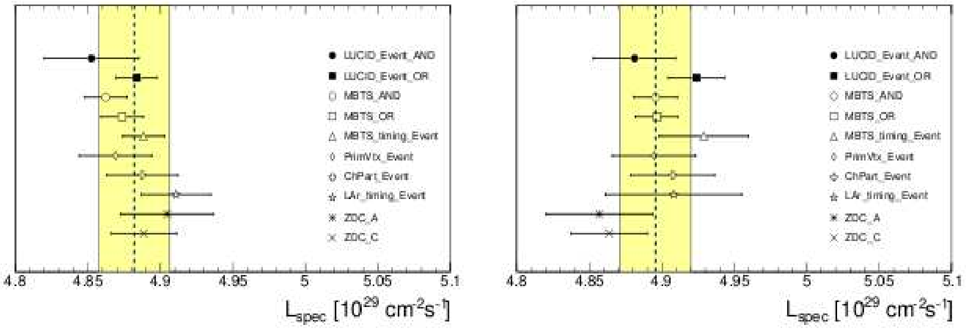

(a) (b)

Figure 6.5: Comparison of the specific luminosities obtained using various luminosity algorithms for (a) Scan II and (b) Scan III. The dashed vertical line shows the unweighted average of all algorithms; the shaded band indicates a 0.5% variation from that mean. The uncertainties on the points are the statistical errors reported by the vdM fit. Uncertainties for different algorithms using the same detector are correlated.

separation, effects due to imperfect beam centering, change in the transverse emittance, μ dependence of the counting rate, choise of the fit model as well as other sources of non-reproducibility. All these sources of systematic errors have been studied. The summary of systematic uncertainties on the visible cross section σ_{vis} obtained from the first three beam scans are reported in table 6.4 [17]. The overall uncertainty of 11% is dominated by the uncertainty on the measurements of bunch currents. Description of only the principal source of systematic error is here reported. For more details about all the uncertainty sources see [40].

Source	*Uncertainty on* σ_{vis} *(%)*
Beam intensities	10
Lenght scale	2
Imperfect beam centering	2
Transverse emittance changes	3
mu dependence	2
Fit Model	1
Total	11

Table 6.4: Summary of sytematic uncertainties on the visible cross section obtained from beam scans. Because σ_{vis} is used to determine the absolute luminosity, these results are also the systematic uncertainties on the beam-scan based luminosity calibration.

At least some portion of these uncertainties is common to interaction point 1 (AT-

LAS) and 5 (CMS); the size of this correlated uncertainty remains under study.

LHC Bunch Currents

A systematic error in the measurement of the absolute bunch charge translates directly into an uncertainty on the luminosity calibration. The accuracy of the bunch intensity measurement depends on that of the DCCT calibration. The DCCT suffers from slow drifts for a variety of reasons including temperature effects, machanical vibrations and electromagnetic pick-up in cable. For each fill, the baseline readings for each beam (corresponding to zero current) must be determined by lookong at periods with no beam immediately before and after each fill. Due to possible variation of this baseline correction over a fill, possible uncertainties have been evaluated based on the observed size of these drifts over time. Because the the baseline offset is found to have a typical variance of $\pm 0.8 \times 10^9$ protons per beam, the relative uncertainty from the baseline determination goes down as the bunch currents go up. During the scans of October the bunch currents increased of about factor ten with respect to the previous scans, that strongly reduced the uncertainty on the bunch current and, as a consequence, on the luminosity calibration [37].
Considerable work has been done since the official presentation [40] of these results by the Bunch Current Normalization Working Group (BCNWG) to improve the determination of the LHC bunch currents and better understand the systematic uncertainties. This work reduced the uncertainty on the beam currents from 10% to about 5% [37], but the analysis is still ongoing.

6.3.4 Comparison with Monte Carlo Predictions

Because the Van der Meer method does not require knowledge of the inelastic cross section nor of the detector acceptance, the values of σ_{vis} obtained from the beam scans can be used to test the accuracy of the predictions of Monte Carlo event generators. Such predictions suffer from several theoretical uncertainties. First, because the *pp* inelastic cross section has not been measured at 7 TeV, the generators obtain σ_{vis} by estrapolating from lower energy. Results of this extrapolation depend on the functional form used. The PYTHIA and PHOJET generators, for example, predict values for σ_{vis} that differ by 6.6%, as reported in table 6.5. Second, the generators must separately model the non-diffractive (ND), single-diffractive (SD) and double-diffractive (DD) components of the cross section. There exists no unique prescription for classifying events as diffractive or non-diffractive and no calculation of the cross sections from first principles. Typical uncertainties associated with such classifications are illustrated in table 5.2. The fraction of σ_{inel} corresponding to ND events is 68% in PYTHIA and 81% in PHOJET, while the

DD fractions are 13% and 5% respectively. Finally, there are significant uncertainties on the modeling of the predicted multiplicity-, p_T- and μ- distributions for particles produced in soft pp interactions, particularly for the poorly constrained diffractive components. Differences in these distributions will affect the efficiencies for events to pass the selection criteria of a specific luminosity algorithm.
There is a systematic difference between the values of σ_{vis} obtained from the first scan and those based on the second and third scans. In reporting the best estimate of the measured visible cross sections, the average the results of the first scan with the average of the second and third scans has been choosen. Comparisons of the Van der Meer scan measurements with the Monte Carlo predictions are presented in table 6.5. For a given event generator, the comparisons exhibit an RMS spread of 4-5%; on the average, the PYTHIA (PHOJET) predictions are 15% (33%) higher than the data. Given the 11% systematic uncertainty on the Van der Meer calibration, which is correlated across all algorithms, PYTHIA agrees with the data at the level of 1.5σ , while PHOJET and the data disagree at the 3σ level.

Algorithm	σ_{vis}^{meas} (mb)	σ_{vis}^{PHYTIA} (mb)	$\frac{\sigma_{vis}^{PHYTIA}}{\sigma_{vis}^{meas}}$	σ_{vis}^{PHOJET} (mb)	$\frac{\sigma_{vis}^{PHOJET}}{\sigma_{vis}^{meas}}$
Event AND	12.4±0.1	16.0±0.8	1.29±0.07	17.0±0.9	1.35±0.07
Event OR	40.2±0.1	46.4±2.8	1.15±0.07	53.1±3.2	1.32±0.07

Table 6.5: Comparison of the visible cross sections determined from the beam scans (σ_{vis}^{meas}) to the prediction of the PYTHIA and PHOJET Monte Carlo generators. The ratio of predictions to measurements is also shown. The errors affecting the measured visible cross sections are statistical only. The errors on the PYTHIA and PHOJET visible cross sections are obtained from the systematic uncertainties associated with modeling the detector response. These uncertainties are fully correlated, row by row, between PYTHIA and PHOJET; they are fully correlated between the two LUCID algorithms. The fully correlated 11% systematic uncertainty on visible cross sections, that arises from the vdM calibration, is not included in the errors listed in this table.

6.4 Conclusions

During 2010 LHC running five Van der Meer scans were performed.
With the results obtained from the analysis of the first three Van der Meer scan data, an estimation of the beam width Σ has been done. The results on Σ provided by the different algorithms show good agreement. A first calibration constant for the absolute luminosity has been provided with the Van der Meer method. The uncertainty on the calibration constant is of 11%, mainly due to the uncertainties on the beam currents. LUCID only systematics errors have been evaluated to be

of about 5%.

The analysis on the fourth and fifth scans is still ungoing. Including the data from the last scans, the uncertainty on the luminosity lowers at 3.4% level, due to the increase of the bunch currents and a better understanding of the uncertainties of their measurements.

Finally, since the Van der Meer method does not require knowledge of the inelastic cross section nor of the detector acceptance, the values of σ_{vis} obtained from the beam scans have been used to cross check the predictions of Monte Carlo simulations.

Chapter 7

Absolute Luminosity Determination with Physics Processes

7.1 Introduction

The Standard Model (SM) is currently the best description of the fundamental structure of matter components and their behaviour. During its development, predictions about the existence of new particles have been made: the discovery of $W^{\pm}$ and Z gauge bosons in 1983 is regarded as one of the most brilliant achievements in modern physics.
Z production at LHC in the ATLAS experiment, in particular in the muon decay channel, is usefull for monitoring the instantaneous luminosity and for calibrating the measurements of the relative luminosity.

7.1.1 Z Production for Luminosity Calibration

LUCID is the principal luminosity monitor for the ATLAS experiment. The instantaneous luminosity is calculated from the measurement of the mean number of pp interaction per bunch crossing via the relation

$$L = \mu \frac{f_r}{\sigma} \tag{7.1}$$

where f_r is the revolution frequency of the accelerator and σ is the inelastic pp cross section. The μ value is related to the quantities measured by LUCID through the different algorithms already described. As visible from the formula, the relative luminosity needs a calibration that depend on the detector. Calibration strategy can be summarized by the following steps:

- Monte Carlo calibration: before data taking, Monte Carlo simulation were used to evaluate the efficiecies of the different algorithms. In the simulations, the pp cross section is assumed to be well known. The accuracy on this calibration is about 20%;

- calibration using beam parameters: the calibration constant is evaluated from the luminosity values provided by the accelerator during the Van der Meer scan. The achieved accuracy with this procedure is of about 3.4% mainly due to the uncertainty on the beam currents. This is the procedure used at present for LUCID calibration;

- calibration with ALFA results: this detector, once installed, will be able to measure the absolute luminosity with an accuracy of about 3%;

- calibration with physics processes: this procedure uses the production rate of a process for which the cross section is precisely calculable to measure the luminosity. Z and W productions are the most suitable processes, due to a large cross section known with a precision of 5%[41]. This method will be described in next sections.

7.2 Z Production at LHC

7.2.1 Particle Description in the Standard Model

According to the Standard Model, all particles can be divided into three cathegories:

- three families of fundamental fermions:

$$\left\{ \begin{pmatrix} \nu_e \\ e \end{pmatrix}_L, e_R, \begin{pmatrix} u \\ d \end{pmatrix}_L, u_R, d_R \right\} \tag{7.2}$$

$$\left\{ \begin{pmatrix} \nu_\mu \\ \mu \end{pmatrix}_L, \mu_R, \begin{pmatrix} c \\ s \end{pmatrix}_L, c_R, s_R \right\} \tag{7.3}$$

$$\left\{ \begin{pmatrix} \nu_\tau \\ \tau \end{pmatrix}_L, \tau_R, \begin{pmatrix} t \\ b \end{pmatrix}_L, t_R, b_R \right\} \tag{7.4}$$

  where ν_e, ν_μ, ν_τ and e, μ, τ are leptons and u, d, c, s, t, b are quarks. Since there is no right handed neutrino, the left handed component is arranged in a doublet while the right handed component is arranged in a singlet;

- four gauge bosons which mediate the electromagnetic and weak interactions between the fundamental fermions. The $W^{\pm}$ and Z^0 are massive boson mediating the weak interactions, while the photon γ is the massless mediator for the electromagnetic interactions;
- one Higgs boson which is the quantum of the Higgs field used to give mass to the gauge boson and to the fundamental fermions without destroying the gauge invariance of the theory.

7.2.2 Z Production

In general, the Z boson, that mediate the weak interactions, decays in three different channels:

- leptonic decay: only leptons partecipate, as in Z decay $Z \to \mu^+\mu^-$;
- semi-leptonic decay: both leptons and quark are involved;
- non-leptonic decay: only hadrons and quarks partecipate, as in the Z decay $u + \bar{u} \to Z \to d + \bar{d}$ that can produce hadronic jets.

The mass and the width of the Z boson as well as the brancing ratios of its decay channels were measured by the LEP experiments to highest precision [42]. The values of the main parameter of the Z resonace are reported in table 7.1.

Mass	91.1875 ± 0.0021 GeV
Width	2.4952 ± 0.0023 GeV
Decay mode	*Probability*
e^+e^-	3.363 ± 0.004
$\mu^+\mu^-$	3.366 ± 0.007
$\tau^+\tau^-$	3.370 ± 0.008
Invisible	20.00 ± 0.06
Hadrons	69.91 ± 0.06

Table 7.1: Mass, width and branching ratio of the decay channels of the Z boson.

The production of Z bosons at LHC is due to the Drell-Yan process. The dominating processes at the LHC are $q\bar{q} \to Z/\gamma^* \to \mu^+\mu^-$ (65%) and $qg \to q\gamma^*/Z \to q\mu^+\mu^-$ (35%) which are illustrated in figure 7.1.

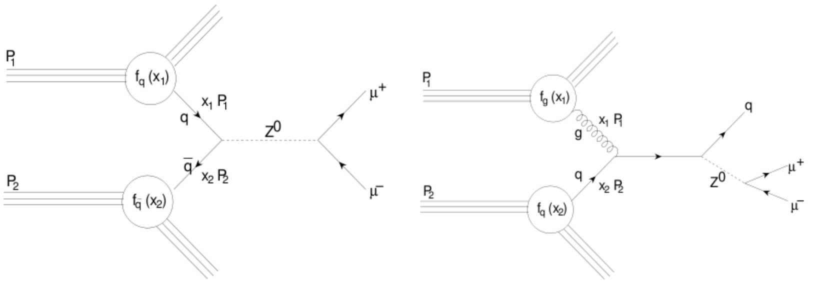

Figure 7.1: Feynmann diagram for a Drell-Yan process at the leading order (left) and next-to-leading order (right) for the Z production.

In a Drell-Yan process, a quark and an antiquark annihilate to produce a intermediate vector boson, which in turn decays in a lepton anti-lepton pair. The dominat higher order correction of the first process of figure 7.1 is the scattering of a quark with a gluon, which contributes roughly 1/3 to the overall cross section of this process. The Drell-Yan process can study the structure of the incident proton till an energy scale of Q^2 equal to the square root of the mass of the lepton pair.

The event topology $pp \rightarrow Z/\gamma^* \rightarrow \mu^+\mu^-$ has a very characteristic signature: two high energetic and isolated muons in the final state are produced. A significant contribution of QCD-background due to the overwhelming cross section of QCD processes is expected. Moreover, the decay of a W boson into one high energetic muon and a neutrino plus an additional muon from a QCD-jet and the process $Z \rightarrow \tau^+\tau^- \rightarrow \mu^+\nu_\tau\nu_\mu\nu_\tau\nu_\mu$ were studied as possible background processes in this analysis.

Due to the high collision energy of LHC, the production of top-quark pairs has a cross section in the order of the signal cross section. The top-quarks mostly decay into a W boson ansd b-quark. The W boson and the b-quark can further decay into muons, which also might fake the signal process.

The cross section in the dileptonic channel is obtained weighting the production cross section with the branching ratio for that particular channel: $\sigma_{pp\rightarrow Z} \times BR_{Z\rightarrow l^+l^-}$ where $BR_{Z\rightarrow l^+l^-}$=0.033658.

7.2.3 Parton Distribution Functions and Theoretical Cross Section

The parton model, developped by Bjorken and Feynmann, decribes hadrons as an incoherent whole of quarks and gluons that carry each of them a fraction x of the proton momentum. Only this fraction of momentum is available during the interactions between quarks. At the basis of this theory there is the so-called asymptotic freedom of quarks: the coupling constant of the strong interaction $\alpha_S(Q^2)$ decreases at energy significantly larger than the hadronic masses. The consequence is that quarks inside protons, both real and virtual, can be considered as free.

The fractional momentum carried by the partons is probabilistically distibuted according to the Parton Distribution Function (PDF): $f_p(x)dx \equiv P(x' \in [x, x+dx])$ with $p = q, \bar{q}, g$. The hadronic cross section is the convolution of the PDF and the partonic cross section.

The study of the PDF is one of the most important issue both of experimental and theoretical physics due to the fact that they represent the main source of uncertainty in the calculation of theoretical cross section of hadronic processes. Many international collaborations have studied the behaviour of the partons in order to provide the most accurate PDF according to the recent sperimental data. CTEQ [43] and MRST [44] are the main providers of instrumentations for the calculation of the PDF at ATLAS.

The PDF are extracted from data in different experiments:

- Deep Inelastic Scattering (DIS) and Drell-Yang on fixed target results (high statistics but energy lower than in colliders);
- results from H1 and ZEUS experiments at HERA $e-p$ collider: it is possible to explore minimum values of the fractional momentum carried by the quarks;
- recent data at Tevatron probe PDF at high energy, thanks to $p\bar{p}$ collisions.

All these results allow a map of the PDF in the plane $Q^2 - x$ where Q^2 is the squared transferred momentum. No mapping is possible in those regions not yet covered by sperimental data: in this case only theoretical extrapolation of the PDF at high energy are possible.

The uncertainties on the PDF dominate the uncertainties on the theoretical cross section of processes like $pp \to Z + X \to \mu\mu + X$ otherwise well understood.

The general formula for the cross section of the Z production is:

$$\frac{d\sigma(pp \to Z)}{dx_F} = \sum_{ab} \int P_{ab}(x_1, x_2, Q^2)\hat{\sigma}(ab \to Z)\delta(x_1 + x_2 - x_F)dx_1 dx_2 \tag{7.5}$$

where

$$P_{ab}(x_1, x_2, Q^2) = f_a(x_1, Q^2) f_b(x_2, Q^2) \tag{7.6}$$

In the formula a and b are two partons inside the proton and P_{ab} are the PDFs for the two partons.

The cross section at Next-to-next-to-leading-order (NNLO) is $\sigma(pp \to Z/\gamma^* \to \mu\mu)$

= 1.972 ± 0.019 nb. The theoretical uncertainty on the cross section is evaluated to be at about 5%, dominated by the uncertainty on the PDF (3%) and by the correction between NLO and NNLO (4%).

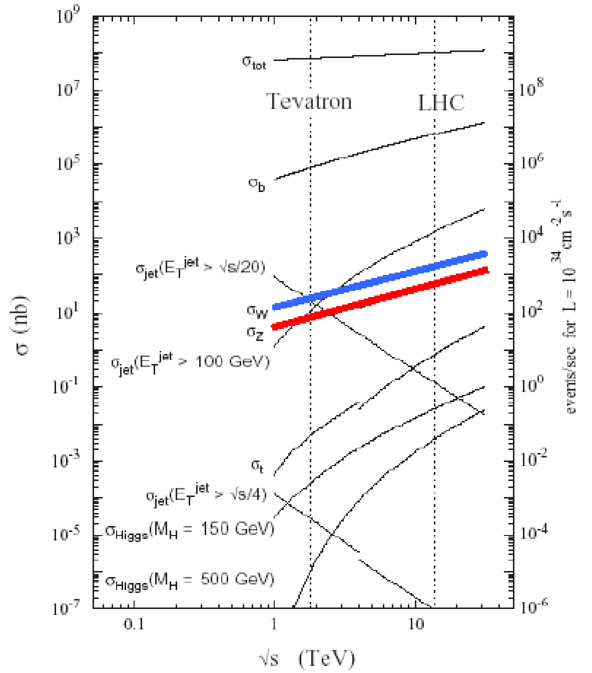

Figure 7.2: Cross section for various processes. The scale on the left represents the cross section measurements. The cross section is provided as a function of the center-of-mass energy. The dashed vertical line corresponds to the center-of-mass energy of 900 GeV and 14 TeV. The scale on the right represents the number of events produced for a luminosity of $L = 10^{34} cm^{-2} s^{-1}$. The cross sections for the Z production (red) and W production (blue) are underlined.

7.2.4 Systematics Uncertainties on Experimental Cross Section

The uncertainties on the experimental cross section are dominated by [41]:

- uncertainties on acceptance and efficiency of the detector. The uncertainty on the acceptance is evaluated from Monte Carlo simulations based on theoretical processes at leading order. The final uncertainty of efficiency × acceptance is thus estimated to be of 6.6%;

- uncertainty on luminosity. The analysis of the first three Van Der Meer scans on early 2010 provides an uncertainty on the luminosity of 11%. This uncertainty is the one used for the next analysis. Recent improvements on the luminosity calibration thanks to the Van der Meer scans of October 2010 reduced the uncertainty on luminosity of about 3.4%.

- physics background plays a marginal role in the Z event selection: the cuts in the event selection are able to remove the majority of background events.

7.3 $\sigma(Z \rightarrow \mu\mu)$ Measurement

The measurement of the luminosity starting from the knowlegde of a cross section for a certain process is based on the formula:

$$\sigma(L) = \frac{N_{sig}^{meas} - N_{back}^{meas}}{\epsilon \times L} \tag{7.7}$$

where N_{sig}^{meas} is the number of reconstructed signal events, N_{back}^{meas} is the number of reconstructed background events, ϵ is the efficiency term given by the sum of the efficiency of the geometrical acceptance of the experiment, of the trigger, of the selection criteria and of the method used for the event reconstruction ($\epsilon = \epsilon_{geom} + \epsilon_{trigger} + \epsilon_{selection} + \epsilon_{reconstruction}$) and L is the integrated luminosity.

7.3.1 Analysis of MC Data

The efficiency that has to be used in the formula 7.7 is evaluated from the Monte Carlo predictions.

MC Sampling

Monte Carlo data have been simulated using PYTHIA generator[45]. The simulation of particles passing through ATLAS has been obtained with package GEANT4[30]. The MRST LO[44] set has been used for the PDF. The migration effect has been simulated convoluting minimum bias events and hard scattering events.

Event Selection

Monte Carlo data are used to evaluate for each cut of the event selection the absolute and relative, defined with respect to the previous cut, efficiency. The original set is composed by 957395 events.
The first cut applied on Monte Carlo data is the requirement of at least one muon

with $p_T > 6$ GeV (trigger called L1_mu6). The second cut is the requirement of at least one primary vertex with a position along the z axis of $|z| < 150$ mm from the ATLAS center and reconstructed by at least three tracks in the Inner Detector. The absolute and relative efficiencies and the number of events passing the selection for each cut are presented in table 7.2.

Cut	*# of events*	*Absolute efficiency*	*Relative efficiency*
MC	957395	-	-
Trigger L1_6mu	820162	-	0.857
Primary vertex	813952	0.850	0.992

Table 7.2: Number of events that survive at each cut. The absolute and relative efficiencies for each cut are also reported.

Pre-selection of Muon Events

The major sources of background for this channel of interest are:

- QDC events: muons from decay of beauty and charmed mesons or from decay of flying pions and kaons. These muons generally belong to a jet. The requirements of the origin from a primary vertex, the isolation of the hadronic traks and high p_T thus drastically reduce this contribution;
- electroweak events: due to $Z \to \tau\tau \to \sum \mu$ and $W \to \mu\nu$ decays;
- cosmic rays: negligible contribution.

The aim of the muon preselection is to efficiently reduce the events from the backgroud thanks to the following cuts:

- the muon must be of the so-called combined type: it has to be reconstructed from a track in the Muon System plus a correspondent track in the Inner Detector. This requirement garantees the rejection of the fake muons, produced by secondary decays;
- muon p_T^{ID} after the refit of the track must be larger than 15 GeV, to reject the QDC background, typically at low p_T;
- muon p_T measured by the Muon System and extrapolated at the primary vertex must be p_T^{MS} >10 GeV;

- the pseudorapidity of the muon must be $|\mu| < 2.4$, that corresponds to the coverage of the muon trigger;
- the difference between the p_T of the track of the Inner Detector and the one of the track of the Muon System, extrapolated at the primary vertex and corrected for the energy loss in the calorimetric system, must be smaller than 15 GeV. This requirement rejects the events from cosmic rays and fake muons;
- the distance between the z coordinate of the muon track and the beam line must be smaller than 10 mm.

The number of events that pass each cut as well as the absolute and relative efficiencies are reported in table 7.3. The relative efficiency is calculated with respect to the number of events that pass the cuts described in table 7.2. The absolute efficiency is calculated with respect to the total number of MC events. These cuts have to be considered, thereby, indipendent and not in sequence.

Cut	*# of events*	*Absolute efficiency*	*Relative efficiency*
Combined	804642	0.841	0.989
$p_T^{ID} > 15$ GeV	770640	0.805	0.947
$p_T^{MU} > 10$ GeV	797533	0.833	0.980
$\|\eta\| < 2.4$	806459	0.842	0.991
$p_T^{ID} - p_T^{MU} < 15$ GeV	804600	0.841	0.989
$\|z - z_{vtx}\| < 10$ mm	804598	0.840	0.989
Total preselection	739789	0.773	0.909

Table 7.3: Number of events that pass each cut on the muon selection. The absolute and relative efficiencies are also reported.

Selection of Events with Z Candidates

The final step of the analysis is the selection of events with two muons consistent with the hypothesis of Z decay. All the kinematic characteristics of the two muons as well as of the Z boson can be then reconstructed. The following cuts are applied in sequence to reject the background:

- at least two combined muons;
- at least two muons with $|\mu| < 2.4$;

- at least two muons that satisfy all the other requirements described in table 7.3;
- at least two isolated muons: no hadronic activity in a cone of radius $\delta R = \sqrt{\Delta\Phi^2 + \Delta\eta^2} = 0.4$ around each muon. The hadronic activity is measured requiring that the sum over all the momenta of all the particles in the isolation cone is $\sum_i \frac{p_{T_i}}{p_T} < 0.2$, where p_T is the muon momentum.

Once an event passes all these cuts, the muons are combined with the requirements of opposite charge and invariant mass in the range 66 GeV $< m_Z <$ 112 GeV. The final cut flow for the Z event selection is reported in table 7.4 as well as the absolute and relative efficiencies. The total efficiency for the Z selection is 38.6%.

Cut	*# of events*	*Absolute efficiency*	*Relative efficiency*
MC	957395	-	-
Trigger L1_6mu	820162	-	0.857
Primary vertex	813952	0.850	0.992
Muon preselection	739789	0.773	0.909
Two combined muons	476684	0.498	0.644
$\|\eta\| < 2.4$	460598	0.481	0.966
p_T	386375	0.404	0.839
Isolation	379869	0.397	0.983
Opposite charge	379856	0.397	1.000
Invariant mass	369515	0.386	0.973

Table 7.4: Number of events that pass each cut for the final Z selection. The absolute and relative efficiencies are also reported.

The systematic uncertainty on the measurements has been evaluated to be of the order of 6%[41].

7.3.2 Analysis of Real Data

The values of $N_{sig}^{meas} - N_{back}^{meas}$ as well as the integrated luminosity are provided using the data acquired during the 2010 *pp* running.

Physics Runs and Data Sampling

The data used to calculate the cross section for the Z production have been taken in 2010 LHC running from April to July, called period A-D. The total number of events is about 325 millions. This choise of a subset of data permits to compare the results with the official one presented in the ICHEP conference [41]. All the runs considered for the analysis correspond to pp collisions at center-of-mass energy of 7 TeV. The data belong to the Luminosity Blocks that satisfy the criteria of good Data Quality. That guarantees that only periods of beam stability and of optimal behaviour of the detectors are considered. The integrated luminosity calculated over the good LBs are presented in table 7.5 for the period used for the analysis described in this section. More statistics was acquired during the period E-F: further studies on these data are ongoing to improve the measurements obtained using only period A-D. The integrated luminosity for period E-F is reported in table 7.5 as well.

Period	*Integrated luminosity* (nb^{-1})
A-C	17.6
D1	28.64
D2	31.76
D3	34.71
D4	87.82
D5	28.38
D6	101.85
E	1125.61
F	1948.44
Sub Total	330.8
Total	3404.85

Table 7.5: Integrated luminosity for the periods used for the measurement of the Z cross section. Periods A-D are used to compare the results with the ones described in the ICHEP note.

The data stream used for the analysis is the so called muon stream: at least one muon has to be identified by the LV1 trigger without cuts on p_T (L1_mu0). This trigger is based on RPC responce in the Barrel region and on TGC responce in the End Cap region. The pseudorapidity cut corresponds to $|\eta| < 2.4$ due to the acceptance of the detectors. In the offline analysis, the requirement of $p_T > 6$ GeV (L1_mu6) is added.

Results

The cuts used for the analysis of the real data are the same used for the MC analysis. The only difference is on the origin of the data sampling. The requirement of events from the bunch crossing is thus added. The cut flow for both periods A-D and A-F is reported in table 7.6. Note that the cut on the choise of muons of opposite charge does not improve the background reduction: the muon selection criteria are satisfactory.

Cut	*Period A-D*	*Period A-F*
Events	35748592	119380480
Trigger	5454359	28601859
Primary vertex	5092105	27477414
Muon preselection	22012	230232
Two combined muons	1944	20481
$\|\eta\| < 2.4$	1881	19637
p_T	149	1416
Isolation	122	1166
Opposite charge	122	1166
Invariant mass	114	1085

Table 7.6: Cut flow used to select Z events in the data stream. The predominant effect of applying each cut on data is the reduction of the background.

The invarianat mass of the Z boson reconstructed with the only trigger requirement and with the pre-selection on muons are presented in figure 7.3. The invariant mass after all the cuts on the event selection is presented in figure 7.4. The signal for the Z is fitted in all cases with a Breit-Wigner for the resonance plus a Gaussian to model the detector resolution. The background is reproduced with an exponential. The width of the resonance is fixed at 2.495[46], while the other parameters of the resonance are free. As visible, the signal-to-noise ratio pass from 1.6 in case of only trigger requirement, to 2.6 in case of muons selection and finally to about 15 when all cuts are applied.

The final candidate for the Z decay are 1017 ± 35 with a reconstructed invariant mass of 90.40 ± 0.14 GeV/c^2. This value must be compared with the value 91.1876 ± 0.0021 GeV/c^2 of [46]. The causes of the disagreement are still under study and probably the agreement will be better achieved using all the statistics acquired in the period A-F.

7.3.3 Comparison between MC and Data Results

All the comparisons of kinematic distributions for the Z candidates between real data and MC simulation show a good agreement, as visible for example for

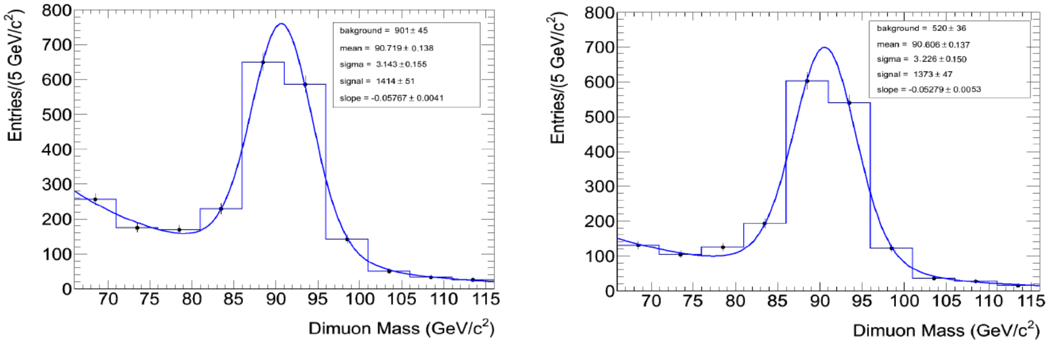

Figure 7.3: Invariant mass for the Z decay into two muons for the period A-F in case of only trigger requirement (left) and muon pre-selection (right). The signal-to-noise ratio changes from 1.6 to 2.6.

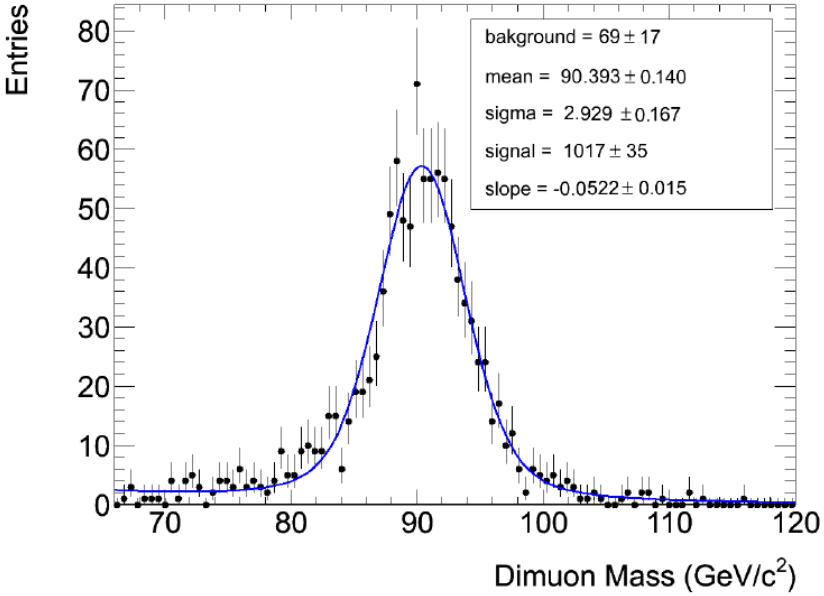

Figure 7.4: Invariant mass for the Z decay into two muons for the period A-F after all the cut flow. The signal-to-noise ratio is about 15.

the p_T value in figure 7.5 and for the pseudorapidity in figure 7.6. This guarantees the correct evaluation of the efficiencies on the cut flow from the MC data.

7.3.4 Measurement of the Cross Section for the Z Production

The relation used to calculate the cross section for the Z production is:

$$\sigma_{q\bar{q}\to Z} \times BR_{Z\to\mu^+\mu^-} = \frac{S}{\epsilon L} \tag{7.8}$$

where L is the integrated luminosity, S is the number of signal events background subtracted as evaluated from data, ϵ is the efficiency provided using Monte Carlo predictions, BR is the branching ratio for the channel under study, given by the theory ($BR_{Z\to l^+l^-} = 0.033658$).
The cross section has been evaluated for the period A-D only. The quantities used to calculate the cross section as well as the statistic and systematic uncertainties are reported in table 7.7.

Parameter	*Value*	*Stat. uncertainty*	*Sys uncertainty*
Number of signal events	104	12	-
Efficiency	0.386	<0.004	0.024 [41]
Luminosity (nb^{-1})	330.8	-	36.4 [38]

Table 7.7: Main quantities used to calculate the cross section for the Z production for period A-D. The statistic and systematic uncertainties are reported as well.

The final cross section measurement is

$$\sigma_{q\bar{q}\to Z} \times BR_{Z\to\mu^+\mu^-} = 0.81 \pm 0.09_{stat} \pm 0.10_{sys} nb \tag{7.9}$$

This value must be compared with the theoretical value

$$\sigma_{q\bar{q}\to Z} \times BR_{Z\to\mu^+\mu^-} = 0.99 \pm 0.05 nb \tag{7.10}$$

The error on the theoretical values is of about 3% due to the uncertainty on the PDF plus 4% due to the NNLO approximation, for a total of 5%. Given the large uncertainties, the experimental measurement is compatible with the theoretical value.

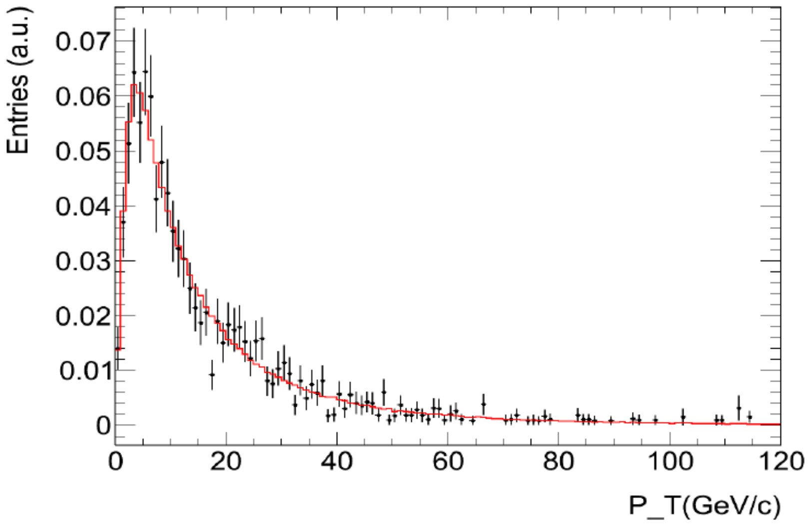

Figure 7.5: p_T distribution for Z candidates in period A-F. Black dots: real data corrected by acceptance and efficiency effects. Red line: MC simulation. Good agreement between data and MC.

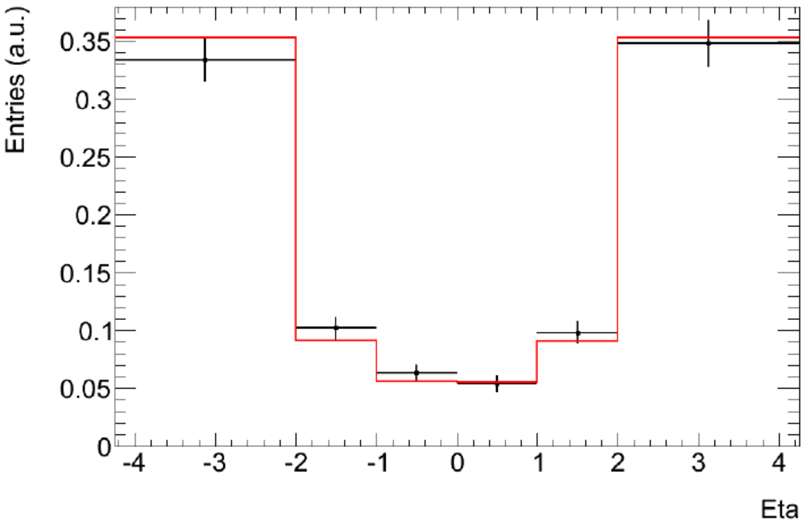

Figure 7.6: Pseudorapidity distribution for Z candidates in period A-F. Black dots: real data corrected by acceptance and efficiency effects. Red line: MC simulation. Good agreeement between data and MC.

7.4 Conclusions

LHC is a Z factory. Thanks to the deep knowledge of the physics associated with the Z production and the low background, the process of Z decay into two muons can be used to evaluate the absolute luminosity.
With a reduced set of data with respect to the all 2010 data taking, the measurement of the cross section for the Z production was in agreement with the theoretical value, given the large uncertainties. The process of Z decay into two muons represents, thus, a good candidate to provide a stable luminosity monitor and a calibration constant for all the luminosity detector with final precision of few percent.
More precision on the cross section measurement will be reached when the Monte Carlo corresponding to the total statistics will be available.

Conclusion

The work described in this thesis concerns mainly the luminosity measurements in the ATLAS experiment, thanks to the dedicated luminosity monitor LUCID. LUCID consist of two symmetric modules situated at 17 m from the interaction point of ATLAS. Each modules is equipped with 20 projective aluminum tubes filled with a radiator gas (C_4F_{10}) kept at a pressure of 1.1 bar. The fast detector response is suitable to separate different bunch crossings. LUCID covers a pseudorapidity range of $[5.6; 5.9]$. Some checks on the performances of LUCID carried out during all the 2010 data taking are reported in chapter 4. LUCID showed good performances and stability during all period of LHC running. The quality checks used to guarantee the optimal functioning of the detector have beem implemented in the ATLAS data acquisition system for the online control of LUCID. With the early data from collisions at center-of-mass energy of 7 TeV, a tuning of the LUCID simulation has also been possible.

Luminosity calculations are performed by the LUMAT card, which provides the luminosity on the basis of 2 different algorithms: the event counting, that counts the events with at least one hit recorded by LUCID, and the hit counting, which counts the mean number of hits per bunch crossing. Each of them can be used both in single side and in coincidence mode. Some performances on luminosity measurements during 2010 data taking are shown in chapter 5. The background due to beam-halo or beam-gas is strongly suppressed with the requirements of coincidence between the two modules. The comparison of luminosities provided by different luminosity monitors showed good agreement: that guarantees the correct use and knowledge of the algorithms implemented in LUCID.

LUCID as well as the other luminosity monitors can measure only the relative luminosity. They need a normalization to provide also the absolute luminosity. Different steps of calibration have been performed according to the different periods of data taking. Before LHC start running, a Monte Carlo simulation based calibration was used. The precision achieved with this method was of about 20% (fully description in chapter 5). During the first period of data taking, the calibration was done with the results of the Van der Meer scan method, described in chapter 6. The accuracy of the calibration constant using the results of the

first three scans performed in 2010 is about 11%, mainly due to the uncertainties on the bunch currents. The precision reaches the 3.4% level considering also the results of the Van der Meer scans performed in October 2010, whose analysis is still ongoing. The Van der Meer scan method for the evaluation of the luminosity calibration is the one used at present. Preliminary studies have been performed to provide a calibration using well known physics processes, as Z and W production. At present precision of 5% can be reached using $Z \rightarrow \mu\mu$ channel (see chapter 7). The ALFA detector was installed during the 2011 shutdown. When ALFA results will be available, the absolute luminosity with precision of 2-3% could be provided measuring the elactic cross section in the Coulomb-Nuclear Interference region.
Thanks to its main features and the good performances it demonstrated, LUCID was the ATLAS dedicated luminosity monitor during all the period of pp collisions. In particular the event OR algorithm was the preferred one that provide the ufficial luminosity value for all the ATLAS analyses.

Appendix A

HIT COUNTING METHODS

The basic idea of the hit counting methods is to correlate μ to the number of particles typically produced in a *pp* collision by counting the number of hit tubes. The number of particles in a bunch is expected to scale with the number of collisions occurred in the bunch. As a consequence, also the number of hit tubes is expected to scale in the same way. A drawback of this method relies on the fact that the counting is based on hit instead on particles: if two particles traverse the same tube the algorithm count only one hit. Since the number of hit per bunch is limited to 32 (total number of tubes in LUCID), a saturation effect is expected when the number of collisions in a bunch increases.

Hit OR

The average number of *pp* interactions per bunch crossing can be written as:

$$\mu = \frac{N_{particles/BX}}{N_{particles/pp}} \tag{7.11}$$

where $N_{particles/BX}$ is the average number of particles per bunch crossing and $N_{particles/pp}$ is the average number of particles per single interaction.
A signal generated by two or more particles crossing the same tube is not distinguished by the signal of a single particles. The maximun number of particles which can be registered by the detector corresponds to the number of tubes ($N_{tubes} = 32$). This leads to a saturation effect: when all the tubes are hit no further interaction can be detected. Assuming that particles spread uniformly over the detector, the average number of particles hitting one tube is $N_{particles}/N_{tubes}$ where $N_{particles}$ is the total number of detected particles. Assuming that particles distribute according to a Poissonian, the probability to have at least one particle in a tube is :

$$1 - e^{-\frac{N_{particles}}{N_{tubes}}} \tag{7.12}$$

Such probability is turned into number of hits with the following formula:

$$N_{hits} = N_{tubes}\left[1 - e^{-\frac{N_{particles}}{N_{tubes}}}\right] \tag{7.13}$$

This equation allow to exctract the number of detected particles from the number of hits using this formula:

$$N_{particles} = -N_{tubes} log\left(1 - \frac{N_{hits}}{N_{tubes}}\right) \tag{7.14}$$

The average number of *pp* interaction can be written as:

$$\mu = \frac{log\left(1 - \frac{N_{hits/BX}}{N_{tubes}}\right)}{log\left(1 - \frac{N_{hits/pp}}{N_{tubes}}\right)} \tag{7.15}$$

where the number of hits per single interaction $N_{hits/pp}$ is measured during calibration runs.

Hit AND

In hit AND counting mode, there are two possibilities to detect a bunch with multiple interactions. A *true* coincidence occurrs when at least one interaction is detected simultaneously in both modules. A *fake* coincidence occurrs when no interaction is detected simultaneously in both modules, but at least two interactions are separately detected in different modules. In both of these cases the average number of detected particles in a bunch with n interactions is the sum of two contributions:

1. the bunch contains at least one interaction which is detected in both modules, together with any number of interaction which are detected in module A but not in module C and vice versa;
2. the bunch contains 0 interactions detected in both modules, together with at least one interaction which is only detected in module A and on ewhich is only detected in module C.

Recall for completeness the definitions of efficiencies and average number of particles in tables 7.8 and 7.9.

These efficiency are related to each other through the following relations:

$$\begin{aligned} \epsilon^0 &= 1 - \epsilon^1 - \epsilon^2 - \epsilon^{coinc} \\ \epsilon^1 &= \epsilon^A - \epsilon^{coinc} \\ \epsilon^2 &= \epsilon^C - \epsilon^{coinc} \\ \epsilon^3 &= \epsilon^{coinc} \end{aligned} \tag{7.16}$$

ϵ^{sing}	efficiency in single side mode
ϵ^{coinc}	efficiency in coincidence mode
ϵ^{A}	efficiency of detecting interaction in side A (coincidence included)
ϵ^{C}	efficiency of detecting interaction in side C (coincidence included)
ϵ^{0}	efficiency of detecting no interaction
ϵ^{1}	efficiency of detecting an interaction in A but not in C
ϵ^{2}	efficiency of detecting an interaction in C but not in A
ϵ^{3}	efficiency of detecting an interaction in A both modules
ϵ^{4}	efficiency of detecting an interaction in one module but not in both

Table 7.8: Different definition of efficiencies for detecting interaction.

Efficiencies and number of particles are related by the following relations:

C_1	no. of particles per detected interaction in A but not in C
C_2	no. of particles per detected interaction in C but not in A
C_3	no. of particles per detected interaction in both modules
C_4	no. of particles per detected interaction in one modules, not in both
C^A	no. of particles per detected interaction in A
C^C	no. of particles per detected interaction in C
C^{coinc}	no. of particles per detected interaction in both modules

Table 7.9: Different definition of number of particles per detected interaction.

$$\begin{aligned} C_1\epsilon_1 &= C_A\epsilon_A - C_{coinc}\epsilon_{coinc} \\ C_2\epsilon_2 &= C_C\epsilon_C - C_{coinc}\epsilon_{coinc} \end{aligned} \tag{7.17}$$

Given these definitions, the average number of particles corresponding to terms I and II is the sum of probability of each configuration times the corresponding number of detected interactions, times the number of particles per detected interaction. Terms I and II can be written as:

$$I = \sum_{k=1}^{n} \epsilon_3^k \binom{n}{k} \left[\sum_{l=0}^{n-k} \epsilon_4^l (1-\epsilon_4-\epsilon_3)^{n-k-l} \binom{n-k}{l} \right] [kC_3 + lC_4] \tag{7.18}$$

$$II = \sum_{k=1}^{n} \epsilon_1^k \binom{n}{k} \left[\sum_{l=0}^{n-k} \epsilon_2^l \epsilon_0^{n-k-l} \binom{n-k}{l} \right] [kC_1 + lC_2] \tag{7.19}$$

Supposed n interactions occurred in a bunch crossing.

Term I

The first contribution consists of k interactions detected in both modules, l of the remaining $n-k$ interactions detected in only one module and the remaining $n-k-l$ interactions undetected.
The probability of detecting l interactions in both modules is ϵ_3^k. The probability of detecting l interactions in only one module is ϵ_4^l. The probability of no detecting $n-k-l$ interactions is $(1-\epsilon_4-\epsilon_3)^{n-k-l}$.
Binomial factors are used to account for all permutations of k out of n interactions and l out $n-k$ interactions.
The average number of particles given by k interactions detected in both modules is kC_3; the average number of particles given by l interactions detected in one module only is lC_4.

TermII

The second contribution consist of k interactions detected in module A but not in C, l of the remaining $n-k$ interaction detected in module C but not in A, and the remaining $n-k-l$ interactions undetected.
The probability of detecting k interaction in module A is ϵ_1^k. The probability of detecting l interatcion in module C is ϵ_2^l. The probability of no detecting $n-k-l$ interactions is ϵ_0^{n-k-l}.
Binomial factor are used to account for all permutations of k out of n interactions and l out of $n-k$ interactions.
The average number of particles given by k interactions detected in both modules is kC_1. The average number of particles given by l interactions detected in one module only is lC_2.

Sum over l

The l-sums in previous equations can be evaluated by means of the binomial theorem:

$$kC_3 \sum_{l=0}^{n-k} \epsilon_4^l (1-\epsilon_4-\epsilon_3)^{n-k-l} \binom{n-k}{l} = kC_3(1-\epsilon_3)^{n-k} \tag{7.20}$$

$$C_4 \sum_{l=0}^{n-k} l\epsilon_4^l (1-\epsilon_4-\epsilon_3)^{n-k-l} \binom{n-k}{l} = C_4(n-k)\epsilon_4(1-\epsilon_3)^{n-k-1} \tag{7.21}$$

$$kC_1 \sum_{l=1}^{n-k} \epsilon_2^l \epsilon_0^{n-k-l} \binom{n-k}{l} = kC_1 \left[(\epsilon_0+\epsilon_2)^{n-k} - \epsilon_0^{n-k}\right] \tag{7.22}$$

$$C_2 \sum_{l=1}^{n-k} l\epsilon_2^l \epsilon_0^{n-k-l} \binom{n-k}{l} = C_2(n-k)\epsilon_2(\epsilon_0 - \epsilon_2)^{n-k-1} \tag{7.23}$$

Sum over k

The k-sums in previous equations can be evaluated by means of the binomial theorem:

$$C_3 \sum_{k=1}^{n} k\epsilon_3^k (1-\epsilon_3)^{n-k} \binom{n}{l} = C_3\epsilon_3 n \tag{7.24}$$

$$C_4\epsilon_4 \sum_{k=1}^{n} n\epsilon_3^k (1-\epsilon_3)^{n-k-l} \binom{n}{l} = C_4\epsilon_4 n \left[\left(\frac{1}{1-\epsilon_3} \right) - (1-\epsilon_3)^{n-1} \right] \tag{7.25}$$

$$-C_4\epsilon_4 \sum_{k=1}^{n} k\epsilon_3^k (1-\epsilon_3)^{n-k-l} \binom{n}{l} = -C_4\epsilon_4 n \frac{\epsilon_3}{1-\epsilon_3} \tag{7.26}$$

$$C_1 \sum_{k=1}^{n} k\epsilon_1^k (\epsilon_0 + \epsilon_2)^{n-k} \binom{n}{l} = C_1\epsilon_1 n(\epsilon_0 + \epsilon_1 + \epsilon_2)^{n-1} \tag{7.27}$$

$$-C_1 \sum_{k=1}^{n} k\epsilon_1^k \epsilon_0^{n-k} \binom{n}{l} = -C_1\epsilon_1 n(\epsilon_0 + \epsilon_1)^{n-1} \tag{7.28}$$

$$C_2\epsilon_2 \sum_{k=1}^{n} n(\epsilon_0 + \epsilon_2)^{n-k-l} \binom{n}{l} = C_2\epsilon_2 n \left[\frac{(1-\epsilon_3)^n}{\epsilon_0 + \epsilon_2} - (\epsilon_0 + \epsilon_2)^n \right] \tag{7.29}$$

$$-C_2\epsilon_2 \sum_{k=1}^{n} k\epsilon_1^k (\epsilon_0 + \epsilon_2)^{n-k-1} \binom{n}{l} = -C_2\epsilon_2 n\epsilon_1 \frac{(1-\epsilon_3)^{n-1}}{\epsilon_0 + \epsilon_2} \tag{7.30}$$

Sum of terms I and II

Given that $C_1\epsilon_1$ is the number of particles registered in the whole detector when the interaction is detected in module A only and $C_2\epsilon_2$ is the number of particles registered in the whole detector when the interaction is detected in module C only, the sum of these terms gives the number of particles registered in the whole detector when the interaction is detected in module A or in module C but not in both:

$$C_4\epsilon_4 = C_1\epsilon_1 + C_2\epsilon_2 \tag{7.31}$$

Using this relation the sum of term I and II can be written as:

$$I + II = C_3\epsilon_3 n + C_1\epsilon_1 n \left[1 - (\epsilon_0 + \epsilon_1)^{n-1} \right] + C_2\epsilon_2 n \left[1 - (\epsilon_0 + \epsilon_2)^{n-1} \right] \tag{7.32}$$

Poissonian sum

The average number of particles per bunch is given by the convolution of the previous equation with a Poissonian of average μ:

$$N_{particles/BX} = \sum_{n=0}^{\infty}(I + II)\frac{e^{-\mu}\mu^n}{n!} \tag{7.33}$$

Given the relations:

$$\begin{aligned} \sum_{n=0}^{\infty}\frac{e^{-\mu}\mu^n}{n!} &= \mu \\ \sum_{n=0}^{\infty}\frac{k^n}{n!} &= e^k \end{aligned} \tag{7.34}$$

The average number of particles per bunch crossing becomes:

$$N_{particles/BX} = C_3\epsilon_3\mu + C_1\epsilon_1\mu\left[1 - e^{-\mu(\epsilon_2+\epsilon_3)}\right] + C_2\epsilon_2\mu\left[1 - e^{-\mu(\epsilon_1+\epsilon_3)}\right] \tag{7.35}$$

Using the definition of inclusive average number of particles described in table 7.9 the final equation for the average number of particles becomes:

$$\begin{aligned} N_{particles/BX} =& \mu C^{coinc}\epsilon^{coinc} + \\ & \mu C^{coinc}\epsilon^{coinc}\left(\frac{C^A\epsilon^A}{C^{coinc}\epsilon^{coinc}} - 1\right)\left(1 - e^{-\mu\epsilon^C}\right) + \\ & \mu C^{coinc}\epsilon^{coinc}\left(\frac{C^C\epsilon^C}{C^{coinc}\epsilon^{coinc}} - 1\right)\left(1 - e^{-\mu\epsilon^A}\right) \end{aligned} \tag{7.36}$$

as reported in chapter 5.

Appendix B

ZERO COUNTING METHODS

The basic idea of zero counting method is to correlate μ to the frequency of empty bunch crossings. The zero counting method has the advantage of simplicity but it has the drawback that the rate of empty events decreases by increasing luminosity, expecially for detector with large detection efficiency (zero starvation).

Zero AND

In the zero AND counting, a zero count is detected when both of two LUCID modules have detected zero interactions. The probability of having an empty bunch (N_0/N_{BX}) is given by two contributions:

1. probability of having 0 interactions;
2. probability of having n interactions with 0 hits in both modules.

Term I is the Poissonian probability of having zero interactions:

$$P_\mu(0) = \frac{e^{-\mu}\mu^0}{0!} = e^{-\mu} \tag{7.37}$$

Given the probablity to detect an interaction in single side mode (ϵ^{sing}), term II is the combined probability of not detecting the n interactions occurring in a bunch:

$$II = (1 - \epsilon^{sing})^n \tag{7.38}$$

Term II is convoluted with a Poissonian distribution of average μ.

$$\sum_{n=1}^{\infty}(1 - \epsilon^{sing})^n \frac{e^{-\mu}\mu^n}{n!} = \sum_{n=0}^{\infty}(1 - \epsilon^{sing})^n \frac{e^{-\mu}\mu^n}{n!} - e^{-\mu} = e^{-\epsilon^{sing}\mu} - e^{-\mu} \tag{7.39}$$

Note that the sum begins with n=1 to exclude term I. The total probability od observing an empty event is the sun of the two previous equations:

$$\frac{N_0}{N_{BX}} = e^{-\mu} + e^{-\epsilon^{sing}\mu} - e^{-\mu} = e^{-\epsilon^{sing}\mu} \tag{7.40}$$

In order to determine the luminosity, this expression has to be inverted and the following formula is obtained:

$$\mu_{zeroAND} = -\frac{1}{\epsilon^{sing}} \cdot ln\left(\frac{N^0}{N_{BX}}\right) \tag{7.41}$$

in which the number of interactions per bunch crossing is related to the fraction of empty bunches.

Zero OR

In the zero OR algorithm a zero count is detected when at least one of the two LUCID modules has no hit. The total probability is given by the sum of four contributions:

1. probability of having 0 interactions;
2. probability of having n interactions with at least one interaction detected in module A, together with a number of interactions not detected in module C;
3. probability of having n interactions with at least one interaction detected in module C, together with a number of interactions not detected in module A;
4. probability to have n interactions with 0 hits in both modules.

The term I is the Poissonian probability of having 0 interactions:

$$P_\mu(0) = \frac{e^{-\mu}\mu^0}{0!} = e^{-\mu} \tag{7.42}$$

Term II(III) consists of all the permutations of k interaction detected in module A(C) and $n - k$ interactions not detected in any module:

$$II = \sum_{k=1}^{n} \epsilon_1^k \epsilon_0^{n-k} \binom{n}{k} = (\epsilon_1 + \epsilon_o)^n - \epsilon_0^n \tag{7.43}$$

$$III = \sum_{k=1}^{n} \epsilon_2^k \epsilon_0^{n-k} \binom{n}{k} = (\epsilon_2 + \epsilon_o)^n - \epsilon_0^n \tag{7.44}$$

Term IV is the probability of having a bunch crossing with n interactions which are not detected in any of the two modules:

$$IV = \epsilon_0^n \tag{7.45}$$

Term II, III and IV are convoluted with a Poissonian distribution of average μ (notice that the sum starts from n=1 to exclude the term I):

$$\sum_{n=1}^{\infty} \frac{e^{-\mu}\mu^n}{n!}[(\epsilon_1+\epsilon_0)^n - \epsilon_0^n] = e^{-\mu}[e^{-\mu(\epsilon_1+\epsilon_0)} - e^{\mu\epsilon_0}] \tag{7.46}$$

$$\sum_{n=1}^{\infty} \frac{e^{-\mu}\mu^n}{n!}[(\epsilon_2+\epsilon_0)^n - \epsilon_0^n] = e^{-\mu}[e^{-\mu(\epsilon_2+\epsilon_0)} - e^{\mu\epsilon_0}] \tag{7.47}$$

$$\sum_{n=1}^{\infty} \frac{e^{-\mu}\mu^n}{n!}\epsilon_0^n = e^{-\mu}(e^{\mu\epsilon_0} - 1) \tag{7.48}$$

The total probability is the sum of all the four terms:

$$\frac{N_0}{N_{BX}} = e^{-\mu(1-\epsilon_0-\epsilon_1)} + e^{-\mu(1-\epsilon_0-\epsilon_2)} - e^{-\mu(1-\epsilon_0)} \tag{7.49}$$

Given the previous relations with inclusive efficiency definitions this equation can be written as:

$$\frac{N_0}{N_{BX}} = f(\mu) = e^{-\mu\epsilon_A} + e^{-\mu\epsilon_C} - e^{-\mu(\epsilon_A+\epsilon_C-\epsilon_{coinc})} \tag{7.50}$$

The average number of interactions per bunch crossing is obtained by numerical inversion of previous equation.

$$\mu = f^{-1}\left(\frac{N_0}{N_{BX}}\right) \tag{7.51}$$

Appendix C

PMT calibration from signal

This method is based on the principle of functioning of the electronics that characterize a photomultiplier. The photoelectron current I_{pk}, emitted from the photocathod in presence of incident light, strikes the first dynode plane where secondary electrons are produced. Each of the secondary electrons is accelerated up to the second dynode plane where it is multiplied again. Thus a cascade process is produced up to the last dynode. Assuming that one electron impinging on the dynode number i produces in average k_i secondaries with variance $\sigma^2_{k_i}$. The secondary emission ratio k_i is a function of the interdynode voltage. The output of the first dynode striking the second dynode produces an average gain m_2 with variance $\sigma^2_{m_2}$. Using cascade events statistics, the average gain and its variance may be related to the individual dynode statistics as follow: $m_2 = k_1 \cdot k_2$ and $\sigma^2_{m_2} = k_2^2 \sigma^2_{k_1} + k_1 \sigma^2_{k_2}$. Up to the last stage, the gain and its variance can be written as:

$$m_n = \prod_{i=1}^{i=n} k_i \tag{7.52}$$

$$\sigma^2_{m_n} = m_n^2 \cdot \left(\frac{\sigma^2_{k_1}}{k_1^2} + \frac{\sigma^2_{k_2}}{k_1 k_2^2} + ... + \frac{\sigma^2_{k_n}}{k_1 k_2 .... k_{n-1} k_n^2} \right) \tag{7.53}$$

The signal-to-noise ratio is given by:

$$\frac{m_n}{\sigma_{m_n}} = \left(\frac{\sigma^2_{k_1}}{k_1^2} + \frac{\sigma^2_{k_2}}{k_1 k_2^2} + ... + \frac{\sigma^2_{k_n}}{k_1 k_2 .... k_{n-1} k_n^2} \right)^{-1/2} \tag{7.54}$$

These equations state the expected results: the total average gain for a series of n dynodes is the product of the secondary emission yields of the individual dynodes in the series; the relative contribution of any stage to the total fluctuation decreases with the proximity of the dynodes to the output end of the chain (the first stage contributes the most).

Assuming an isovoltage repartition in the phototmultiplier where $k_i = k \forall i$ and a secondary emission that follows a poissonian statistics for which $\sigma^2_{k_i} = k_i$ the signal-to-noise ratio is given by:

$$\begin{aligned}\left(\frac{m_n}{\sigma_{m_n}}\right)^2 &= \frac{k_1}{k_1^2} + \frac{k_2}{k_1 k_2^2} + ... + \frac{k_n}{k_1 k_2 .... k_{n-1} k_n^2} \\ &= \frac{1}{k_1} + \frac{1}{k_1 k_2} + ... + \frac{1}{k_1 k_2 .... k_n} \\ &= \frac{1}{k} + \frac{1}{k^2} + ... + \frac{1}{k^n}\end{aligned} \tag{7.55}$$

that can also be written as:

$$\left(\frac{m_n}{\sigma_{m_n}}\right)^2 = \frac{1}{k-1} \cdot \left(1 - \frac{1}{k^n}\right) \tag{7.56}$$

where

$$F = \frac{1}{k-1} \cdot \left(1 - \frac{1}{k^n}\right) \tag{7.57}$$

is called the noise factor.
The average number of photoelectrons after conversion from the photocathode is given by $N_{p.e.} = \eta N_\gamma$ where η is the quantum efficiency and N_γ is the mean number of photoelectrons impinging the photocathode. The variance is given by $\sigma^2_{N_{p.e.}} = \eta \sigma^2_{N_\gamma}$. Using these relations the average number of electrons collected at the anode and its variance can be stated as follows:

$$\begin{aligned}&N_a = \eta N_\gamma m_n = N_{p.e.} m_n \\ &\sigma^2_{N_a} = m_n^2 \sigma^2_{N_{p.e.}} + N_{p.e.} \sigma^2_{m_n} = m_n^2 \eta \sigma^2_{N_\gamma} + \eta N_\gamma \sigma^2_{m_n}\end{aligned} \tag{7.58}$$

Assuming a poissonian behavoiur of secondary emission $\sigma^2_{N_\gamma} = N_\gamma$, the previous equations can be rearranged as follows:

$$\begin{aligned}&N_a = N_{p.e.} m_n \\ &\sigma^2_{N_a} = m_n^2 \eta \sigma^2_{N_\gamma} + \eta N_\gamma \sigma^2_{m_n} = N_{p.e.}(\sigma^2_{m_n} + m_n^2) = N_{p.e.} m_n^2 (1+F)\end{aligned} \tag{7.59}$$

Finally the signal-to-noise-ratio can be written as:

$$\left(\frac{\sigma_{N_a}}{N_a}\right)^2 = \frac{N_{p.e.} m_n^2 (1+F)}{N_{p.e.}^2 m_n^2} = \frac{1+F}{N_{p.e.}} \tag{7.60}$$

Recall the expression for F without considering the second term which is $\ll 1$, the final relation is:

$$\left(\frac{\sigma_{N_a}}{N_a}\right)^2 = \frac{\left(1 - \frac{1}{k}\right)}{N_{p.e.}} = \frac{f}{N_{p.e.}} \tag{7.61}$$

Rearranging the previous equation the relation becomes:

$$\frac{\sigma_{N_a}^2}{N_a} = \frac{N_a}{N_{p.e.}} \cdot f = K_{cal} \cdot f \qquad (7.62)$$

where $\frac{N_a}{N_{p.e.}}$ is the calibration constant (called K_{cal}) because it is the ratio between the amplitude of the signal and the average number of photoelectrons produced by the photcathode.
The previous description has been done under the assumption that all the dynodes have the same applied voltage.

Bibliography

[1] CERN, LHC Design Report Volume I: The LHC Main Ring, CERN-2004-003-V-1. (2004).

[2] ALEPH, DELPHI, L3 and OPAL Collaboration, Phys. Lett. B565 (2003) 61.

[3] B.W.Lee at al Phys. Rev. Lett 38 (1977) 883; M.Quiros, *Constaints on the Higgs boson properties from the effective potential*, hep-ph/9703412; A. Ghinculov and T. Binothe, Acta Phys. Polon. B30 (1999) 99.

[4] The LEP Collaboration ALEPH, DELPHI, L3 and OPAL, the LEP Electroweak Working Group, the SLD Electroweak and Heavy Flavour Groups, *A combination of preliminary electroweak measurements and contraints on the Standard Model*, hep-ex/0312023; Updates numbers from the LEP Electroweak Working Groups: http://lepewwg.web.cern.ch/LEPEWWG. The LEP Collaborations ALEPH, DELPHI, L3 and OPAL, the LEP Electroweak Working Gropus, *Precision Electroweak Measurements and Constrains on the Standard Model*, arXiv:0712.0929[hep-ex], December 2007.

[5] A. Djouadi et al., Phys. rept. 457 1-216, 2008, LPT-Orsay-05-17 *The Anatomy of Electroweak Symmetry Breaking, Tome II*, aXiv:0503172[hep-ph].

[6] A. Djouadi et al., Phys. rept. 459 1-241, 2008, LPT-Orsay-05-18 *The Anatomy of Electroweak Symmetry Breaking, Tome II*, aXiv:0503173[hep-ph].

[7] See for instance: G.Altarelli, F.Feruglio and I.Masina, JHEP 0011 (2000) 040.

[8] G.R. Farrar and P.Fayet, Phys. Lett. B76 (1978) 575.

[9] J.R.Ellis, J.S.Hagelin, D.V.Nanopoulos, K.A.Olive and M.Srednicki, Nucl. Phys. B238 (1984) 453.

[10] ATLAS Collaboration, and G. Aad et al., *The ATLAS Experiments at the CERN Large Hadron Collider*, JINST 3:S08003 (2008).

[11] ATLAS Collaboration, ATLAS TDR 14, CERN/LHCC/99-14, 5 (25 May 1999).

[12] T.Cornelissen, *Track Fitting in the ATLAS Experiment*, PhD thesis, NIKHEF, 2006.

[13] *ATLAS Forward Detector for Luminosity Measurements and Monitoring Letter of Intent*, CERN-LHCC/04-10, LHCC I-014.

[14] ATLAS Collaboration, *ATLAS, High Level Trigger, Data Acquisition and Controls*, CERN/LHCC/2003-022, Geveva, CERN 2003.

[15] C. Ohm, T. Pauly, *The ATLAS beam pick-up based timing system*, NIM A (2009).

[16] D. Belohrad, J-J. Gras, L.K. Jensen, O.R. Jones, M. Ludwig, P. Odier, J.J. Savioz, S. Thoulet, *Commissioning and First Performances of the LHC Beam Currens Measurement Systems*, http://accelconf.web.cern.ch/AccelConf/IPAC10/papers/mope059.pdf.

[17] *Luminosity determination using the ATLAS detector*, ATL-ATLAS-CONF-2010-060, July 20, 2010.

[18] W.Herr, B.Muratori, *Concept of Luminosity*, CERN 2006-002 (2006).

[19] E.D.Courant, H.Snyder, Ann. Phys, 3,1, (1958).

[20] S.De Capua et al, *Luminosity measurements at LHC*, Nuovo Cim. 123B: 423-434, 2008.

[21] S.van der Meer, CERN-ISR-PO-68-31, 1968.

[22] The TOTEM Collaboration, The TOTEM experiment at the CERN Large Hadron Collider, 2008 JINST 3 S08007.

[23] W.R Leo, *Techniques for Nuclear and Particle Physics Experiments*, Springer-Verlag.

[24] S.Baranov at al., *Estimation od Radiation Background, Impact on Detectors, Activation and Shiedling Optimization in ATLAS* ATL-GEN-2005-001.

[25] R.Arnold et alt., NIM A270 (1988) 289.

[26] A. Sbrizzi et al, *Simulation of ATLAS Luminosity Monitoring with LUCID*, ATLAS not, 26 January, 2010.

[27] Slim5 Collaboration, *Beam test Reasults of 4k pixel CMOS MAPS ans High Resistive Striplets Detectors equipped with digital sparsified readout in the Slim5 Low Mass Silicon Demonstrator*, NIM A.

[28] Slim5 Collaboration, *SLIM5 beam test results for thin striplet detector and fast readout beam telescope*, NIM A.

[29] I.Chirikov-Zorin, I.Fedorko, A.Menzione, I.Sykora, S.Tokar, *Single Photoelectron Spectra Analisys for the Metal Dynode Photomultiplier*, NIM A461 (2001) 587-590

[30] S.Agostinelli et al.; NIM A506 (2003) 250.

[31] Hamamatsu private communication.

[32] R.Engel, *Phojet manual*, http://www-ik.fzk.de/ engel/phojet.html.

[33] http://www.staff.uni.mainz.de/zeitnitz/Gcalor/gcalor.html.

[34] TOSCA, program developed by Vactor Field Limited, http://www.vectorfields.com

[35] M.Bruschi, D.Caforio, A.Floderus, V.Hedberg, W.Kozanecki, C.Sbarra *Effects of stray magnetic fields on the LUCID detector.*, ATLAS note December 17, 2009.

[36] The LUCID group, private communication.

[37] ATLAS Collaboration, *Updated Luminosity Determination in pp Collisions at* $\sqrt{s} = 7TeV$ *using the ATLAS Detector*, March 3, 2011.

[38] H. Burkhardt and P. Grafstrom, *Absolute Luminosity From Machine Parameters*, LHC-PROJECT-report-1019, 2007.

[39] S.M. White, R. Alemany-Fernandez, H.Burkhardt, M.Lamont, *First Luminosity Scans in the LHC*, http://accelconf.web.cern.ch/AccelConf/IPAC10/papers/mopec014.pdf, 2010.

[40] ATLAS Collaboration, *Luminosity Determination in pp Collisions at* $\sqrt{s} = 7TeV$ *using the ATLAS Detector at the LHC*, November 8, 2010.

[41] ATLAS collaboration , *$W \rightarrow \mu\nu$ and $Z \rightarrow \mu\mu$ cross section measurments in proton-proton collisions at $\sqrt{7}\,TeV$ with the ATLAS detector*, ATL-COM-PHYS-2010-685.

[42] LEP Collaboration, *Precision electroweak measurements on the Z resonance*, Phys.Rept., 427:257, 2006.

[43] CTEQ collaboration http://www.phys.psu.edu/ cteq/.

[44] SINTEF Applied Mathematics, *MRST Matlab Reservoir Simulation Toolbar* http://sintef.org/Projectweb/MRST.

[45] Fermilab, *Pythia Physics and Manual*, FERMILAB-PUB-06-052-CD-T (March 2006).

[46] K. Nakamura et al (Particle Data Group (PDG)), JPG 37, 075021 (2010).